UNIVERSITAT DE BARCELONA

X-ray Signatures of Particle Escape from Pulsar Wind Nebulae

Xiying Zhang

PHD THESIS

X-RAY SIGNATURES OF PARTICLE ESCAPE FROM PULSAR WIND NEBULAE

XIYING ZHANG

SUPERVISORS
Dr. Pol Bordas Coma
Dr. Valentí Bosch-Ramon

UNIVERSITAT DE BARCELONA

Xiying Zhang, *X-ray Signatures of Particle Escape from Pulsar Wind Nebulae*, PhD Thesis
Barcelona, 09 de maig de 2024

X-ray Signatures of Particle Escape from Pulsar Wind Nebulae

Memòria presentada per optar al grau de
doctor per la Universitat de Barcelona

Programa de doctorat en Física

Autor
Xiying Zhang

Directors
Dr. Pol Bordas Coma
Dr. Valentí Bosch-Ramon

Tutor
Dr. Alberto Manrique Oliva

DEPARTAMENT DE FÍSICA QUÀNTICA I ASTROFÍSICA

Barcelona, 09 de maig de 2024

UNIVERSITAT DE BARCELONA

DECLARATION

I hereby declare that this thesis represents my own work which has been done after registration for the degree of PhD at University of Barcelona, and has not been previously included in a thesis or dissertation submitted to this or any other institution for a degree, diploma or other qualifications.

Xiying Zhang

Barcelona, 09 de maig de 2024

ACKNOWLEDGMENTS

Throughout the course of this Thesis I have benefited immensely from the support of those around me. I am extremely grateful to my supervisor, Dr. Pol Bordas, who provided me with lots and lots of encouragement, guidance, and patience during the past years, which helped me to grow not only as a researcher but also as an individual. I also want to thank Dr. Valentí Bosch-Ramon who is not only my co-supervisor but also my Catalan tutor (the best one!). Many thanks also go to Professor Marc Ribó and Professo Josep Maria Paredes for their support during the elaboration of this Thesis and for providing the means to expose the obtained results in international conferences. I also want to thank the enjoyable times spent with my office mates. Sincere thanks here go to Núria Torres-Albà, Edgar Molina, Eleni Kefala, Arnau Aguasca, Mar Carretero, Elena Díaz and all my lunch buddies on the 7th floor of the UB Physics Faculty. Special thanks go also to the members of the jury for taking the time to evaluate my work. I'm also indebted to my parents and my grandparents for all their love and support. Finally, this PhD Thesis wouldn't have been possible without the financial support provided by the FI-SDUR Grants of the Generalitat the Catalunya.

RESUM EN CATALÀ

Aquesta tesi doctoral té com objectiu entendre els processos d'escapament de partícules i la seva posterior emissió en nebuloses de vent de púlsar (BSPWNe), intentant connectar a) les troballes observacionals en la banda dels raigs X de grans estructures resoltes en alguns d'aquests sistemes; b) la fenomenologia associada als "TeV Halos" de raigs gamma descoberts recentment, i c) la predicció d'estructures esteses similars en la banda de ràdio. Amb aquesta finalitat, he estudiat en detall tres BSPWN amb característiques d'emissió estesa destacades, detectades en raigs X, que mostren evidències d'aquests processos d'escapament de partícules.

Per a la primera font, PWN J1135-6055, les observacions d'arxiu de *Chandra* han revelat la presència d'una nebulosa compacta així com dues estructures laterals semblants a un jet que mostren una geometria molt asimètrica. L'origen d'aquestes estructures es discuteix en diferents escenaris, ja sigui considerant el desenvolupament de "jets cinètics" a partir de processos d'escapament de partícules, o la presència d'autèntics "jets de púlsars" afectats per la pressió externa. Les propietats de PSR J1135-6055 recorden les de la nebulosa entorn de Geminga, un dels pocs BSPWN amb un TeV Halo confirmat.

Per a la segona font, PWN B1853+01 a W44, s'analitza un extens conjunt de dades de raigs X obtingudes amb les missions *Chandra*, *XMM-Newton* i *NuSTAR*. Els resultats revelen la presència d'una estructura estesa que segueix el púlsar, unes prol.longacions semblants a antenes per davant del púlsar, i amb un espectr molt dur, així com un possible "Halo de raigs X" al voltant del PWN. Aquestes troballes es discuteixen i es comparen amb el PWN de G327.1-1.1, conegut per mostrar també emissions esteses tant d'antenes com d'halos en raigs X. També se sap que PWN a G327.1-1.1 té una contrapartida de en el rang TeV.

Per a la tercera font, IGR J11014-6103 (la "Nebulosa del Far"), s'investiga la possibilitat de detectar emissió ràdio estesa produïda per la mateixa població de partícules que genera les estructures tipus jet detectades en raigs X. Si les partícules relativistes amb factors de Lorentz moderats, $\gamma \gtrsim 10^5$, són capaços d'escapar de la regió de xoc d'arc, aquestes estructures tipus "Halo Radio" es podrien detectar amb els instruments actuals. Aquest estudi proporciona, per tant, una prova observacional que permet limitar el mecanisme d'escapament que es pensa que funciona als BSPWNe.

Els resultats d'aquesta tesi proporcionen nova informació sobre els mecanismes d'escapament de partícules que operen als BSPWNe.

Indiquen, a més a més, que en aquestes fonts hi actua de fet un únic mecanisme responsable de l'emissió estesa al voltant de BSPWNe observada tant a la banda d'energia de raigs X com gamma, i també potencialment detectable a energies corresponents a la banda ràdio.

ABSTRACT

This PhD thesis aims at understanding the particle escape and subsequent emission processes taking place in Bow-shock Pulsar Wind Nebulae (BSPWNe), trying to connect a) the observational findings of large X-ray jet-like structures resolved in some of these systems; b) the phenomenology associated to the recently discovered gamma-ray TeV halos, and c) the prediction of similar extended structures in the radio band. To this end, I have studied in detail three BSPWN with prominent extended emission features detected in X-rays showing evidences of such particle escape mechanism.

For the first source, PWN J1135-6055, archival *Chandra* observations have revealed a compact nebula as well as two lateral jet-like structures displaying a highly asymmetric geometry. The origin of these structures is discussed in different scenarios, either considering the development of "kinetic jets" from particle escape processes, or the presence of "true pulsar jets" bent by the external medium pressure. The properties of PSR J1135-6055 are reminiscent of those of the Geminga PWN, one of the few BSPWN with a confirmed TeV halo structure.

For the second source, PWN B1853+01 located inside SNR W44, a rich X-ray data set composed of archival data from *Chandra*, *XMM-Newton* and *NuSTAR* is analysed. The results reveal the presence of a cometary tail trailing the pulsar, a spectrally hard antennae-like feature ahead of the pulsar, as well as a possible "X-ray Halo" around the PWN. These findings are discussed and compared with the PWN in G327.1-1.1, known to display also both antennae- and halo-like extended emission in X-rays. PWN in G327.1-1.1 is also known to have a TeV counterpart.

For the third source, IGR J11014-6103 (the "Lighthouse Nebula"), the possibility to detect extended radio emission produced by the particle population powering the jet-like structures detected in X-rays is investigated. If relativistic particles with moderate Lorentz factors, $\gamma \gtrsim 10^5$, are able to escape the bow-shock region, such extended "Radio Halo"-like structures could be detected with current instruments. This study provides therefore an observational test allowing to constrain the escape mechanism thought to operate in BSPWNe.

The results of this thesis provide new constraints on the particle escape mechanism(s) operating in BSPWNe, and argue for a common mechanism leading to the extended features around BSPWNe observed in the X-ray and gamma-ray energy band, and potentially detectable also at radio energies.

CONTENTS

1

PREFACE

Pulsar wind nebulae (PWNe) are among the most fascinating objects in the sky. The observation of the Crab Nebula, the most famous and best studied PWN of all times, has a long history going back to the 18th century, when it was discovered and then catalogued as the first entry in the "Messier catalogue". The mysterious nature of this source was not clear until two hundred years later, when W. Baade and F. Zwicky, in 1934, proposed that supernovae (SNe) represent the transition of an ordinary star into a neutron star with a very small radius and an extremely high density (Baade and Zwicky 1934). In the following years, N. Mayall and J. Oort reasoned that the Crab Nebula was the remnant of the supernova explosion SN 1054 (Mayall 1939; Mayall and Oort 1942).

The observational discovery of neutron stars, however, had to await the development of radio telescopes. It was in 1967 that the first pulsed radio signal from CP1919/PSR B1919 + 21 (Hewish et al. 1968) was detected. It was then recognised for the first time that pulsars are actually neutron stars (Gold 1968; Gold 1969). In fact, shortly (just a few months) before the discovery of pulsars, F. Pacini suggested that the rotational energy of the neutron stars could give rise to these Crab-like SNRs (Pacini 1967). The detection of the Crab pulsar in 1968 (Lovelace et al. 1968) definitely demonstrated that pulsars are a manifestation of neutrons stars, which are ultimately the powering engines for the observed Crab-like SNRs.

What was dubbed Crab-like SNRs is called nowadays PWNe, as in these systems pulsar winds are the source of these extended nebulae, which can be observed in almost the entire electromagnetic spectrum, from radio up to X-ray and gamma-ray energies.

The development of X-ray telescopes revolutionized the study of PWNe. Photons at X-ray wavelengths are produced by the most energetic particles accelerated in these nebulae (Gaensler and Slane 2006). Although gamma-ray radiation can also be produced by these highly energetic particles, the angular resolution of gamma-ray telescopes prevents us from pinpointing the precise acceleration location (Aharonian et al. 2006). Focusing X-ray instruments, on the other hand, feature excellent angular resolutions with which fine structures can be resolved with high precision. In this regard, in the early 2000's the *Chandra* satellite unveiled for the first time the torus and jet structure in the Crab Nebula (Weisskopf et al. 2000), an observational finding that was not predicted on theoretical grounds. While the torus feature was soon interpreted in terms of the termination shock produced by an

anisotropic pulsar wind, the formation of the jet structures resolved in the Crab nebula were more puzzling. Further theoretical development explained the formation of these jets as a consequence of the conservation of the magnetic field energy in the shocked pulsar wind, with magnetic hoop stresses redirecting equatorial wind-shocked material towards the pulsar rotation axis.

Jet-like structures have been detected in the past decade from a number of PWNe, becoming a common feature of these systems. The most extreme cases are found in fast-moving pulsars producing BSPWNe (Pavan et al. 2014; Klingler et al. 2016a; Wang 2021; Bordas et al. 2021; de Vries and Romani 2022). Meanwhile, "TeV Halos" around high-energy pulsars have been discovered in the last few years with ground based observatories operating in the TeV energy band, becoming a new class of TeV source (Abeysekara et al. 2017; Riviere et al. 2017; Brisbois et al. 2018; Linden et al. 2017; Aharonian et al. 2021).

Inspired by the possibility that the large-scale X-ray features are actually the result of high-energy particles escaping the PWNe (Bandiera 2008; Olmi and Bucciantini 2019b), and accounting for the phenomenology of these newly detected TeV halos, which may also be the result of gamma-ray emitting particles escaping the parent PWNe (Sudoh et al. 2019; Giacinti et al. 2020), I developed the research exposed in this PhD Thesis, focusing on the study of X-ray jet-like structures in BSPWNe. The goal has been to deep our knowledge on the physics related to novel acceleration processes, emission properties, and escape mechanisms of high-energy particles in BSPWNe, highlighting the possible common and unique origin of jet-like feature in BSPWN in X-rays and TeV halos.

This PhD Thesis is organised as follows: in Chapter 2, I briefly summarize the current theoretical models for pulsars, pulsar winds and PWNe. In Chapter 3, I introduce focusing X-ray telescopes, on particular the *Chandra*, *XMM-Newton* and *NuSTAR* facilities from which I have obtained the observational data used for my studies. In the following Chapters I present my studies on three specific PWNe, namely PWN J1135-6055, PWN B1853+01 and PWN IGRJ11014+6103 (the Lighthouse Nebula). A dedicated observation campaign on the PWN of J1135-6055 combining all available archival *Chandra* data is presented in Chapter 4. Chapter 5 presents a detailed X-ray analysis of PWN B1853+01 located inside the SNR W44, which revealed a complex morphology with peculiar protruding outflows and the possible evidence of an X-ray halo structure. In Chapter 6, predictions on the low-energy emission from the PWN around IGRJ11014+6103 are placed to constrain the escape mechanism that could give rise to the observed X-ray jets, and the possible existence of large-scale extended radio emission from this BSPWN. The nature of the large-scale X-ray jet-like structures in BSPWNe is discussed in Chapter 7, in which I also

address its possible association with the TeV halos phenomenology observed at gamma-ray energies. A summary of my findings and the final conclusions are given in Chapter 8 along with perspectives for future work on these systems.

2

INTRODUCTION

2.1 PULSAR, PULSAR WINDS AND PULSAR WIND NEBULAE

Since the energy source of the PWNe is the central pulsar, the theory of PWN has to necessarily start from our understanding of the physics operating in pulsars, their powerful winds, and the interaction of these winds with the surrounding medium.

2.1.1 *Pulsar basics*

Neutron stars are stellar remnants resulting from a core-collapse supernova explosion of a massive star's core in its last evolutionary stages, when it cannot produce sufficient energy from nuclear fusion to counteract its own gravity and therefore collapses. The extreme pressure present during the explosion causes the electrons and protons to combine to produce neutrons, while emitting large amounts of neutrinos. Neutron stars are found to have a radius on the order of 10 km and masses in a range between 1.4 to 2.9 solar masses, implying an average density even higher than that found in atomic nuclei. Neutron stars are born on the other hand with strong magnetic fields, with values of about 10^{12} G, because of the conservation of magnetic flux, and can rotate rapidly due to angular momentum conservation, with rotation periods in the range between a few ms to tens of seconds (Condon and Ransom 2016).

The magnetospheres of non-accreting rotation-powered pulsars [1] can essentially be considered as a giant rotating magnetic dipoles filled by a force-free plasma (see Fig. 2.1). For a neutron star of radius $R_\star$ with a surface magnetic field $B_\star$ rotating with a period P and an angular velocity Ω ($\Omega = 2\pi P^{-1}$), one can derive its magnetic dipole moment μ at the center of the star, which can be inclined with respect to its rotational axis by an angle α. This rotating magnetic dipole then will radiate energy at a rate given by (Landau and Lifshitz 1975):

$$P_{\rm rad} = \frac{2}{3}\frac{\mu_\perp^2 \Omega^4}{c^3} \ , \tag{2.1}$$

where $\mu_\perp = \mu sin\alpha$ is the projection of the magnetic dipole moment onto the plane perpendicular to the rotation axis, and c is the speed

1 Nebulae associated with magnetars are not discussed in this Thesis, as the physics powering these sources may be different from the ones associated with rotational-powered pulsars.

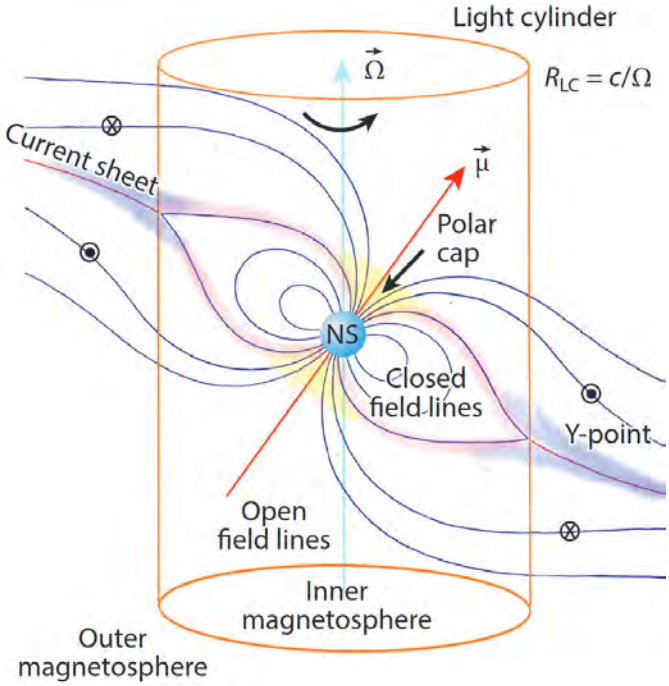

Figure 2.1: Basic structure of a pulsar magnetosphere, with the neutron star located at the center, rotating with an angular velocity $\vec{\Omega}$ around its rotation axis. Magnetic field lines are represented, together with the light-cylinder with a radius $R_{LC} = c/\Omega$ that encompasses the closed co-rotating field lines. Figure from Philippov and Kramer 2022.

of light. If one also assumes that the neutron star is a uniformly magnetized sphere, then $\mu = B_\star R_\star^3$ and

$$P_{\rm rad} = \frac{2}{3}\frac{(B_\star R_\star^3 sin\alpha)^2 \Omega^4}{c^3} = \frac{2}{3}\frac{(B_\star R_\star^3 sin\alpha)^2}{c^3}(\frac{2\pi}{P})^4 \,. \tag{2.2}$$

On the other hand, the pulsar's rotational energy loss is occurring at a rate given by:

$$-\frac{dE}{dt} = -\frac{d(\frac{1}{2}I\Omega^2)}{dt} = -I\Omega\frac{d\Omega}{dt} = 4\pi^2 I\frac{\dot{P}}{P^3} \tag{2.3}$$

where I ($\sim 10^{45}$g cm^2) is the moment of inertia of the pulsar. If the only contribution to the rotational energy loss is the magnetic dipole radiation:

$$-\frac{dE}{dt} = P_{\rm rad} \,, \tag{2.4}$$

then equating Eq. 2.2 and Eq.2.3, one obtains:

$$-4\pi^2 I\frac{\dot{P}}{P^3} = \frac{2}{3}\frac{(B_\star R_\star^3 sin\alpha)^2}{c^3}(\frac{2\pi}{P})^4 \,. \tag{2.5}$$

From this, one can get the minimum magnetic field strength (com-

monly known as characteristic magnetic field) in the case that $\alpha = 90°$:

$$B = (\frac{3c^3 I}{8\pi^2 R_\star^6})^{1/2}(P\dot{P})^{1/2} \,. \tag{2.6}$$

where $B \approx 3.2 \times 10^{19}(P\dot{P})^{1/2}$G, and the period P is given in seconds. Most pulsars with prominent PWNe have indeed inferred magnetic fields in the range $1 \times 10^{12} \leq B \leq 5 \times 10^{13}$G (Gaensler and Slane 2006).

Taking from Eq. 2.5 $\dot{P} = kP^{-1}$, the characteristic age τ_c is defined as follows:

$$\dot{P} = \frac{dP}{dt} = kP^{-1} \rightarrow \int_{P_0}^{P} PdP = \int_0^{\tau_c} kdt \,, \tag{2.7}$$

and if $P_0 \ll P$, then

$$\tau_c \simeq \frac{P}{2\dot{P}} \,. \tag{2.8}$$

Therefore, one can roughly infer the magnetic strength and the age of the pulsar from the specific period and its derivative, e.g. employing the widely used $P - \dot{P}$ diagram (see Fig. 2.2).

It is to be noted that $t_c = \frac{P}{2\dot{P}}$ represents an upper limit to the true pulsar age, as it assumes that the pulsar was born spinning infinitely fast. The so-called braking index n is also defined $\dot{\Omega} = k\Omega^n$. While in the pure magnetic dipole radiation case $n = 3$ (see Eq. 2.5), it is usually assumed that $2 \leq n \leq 3$ - as for instance the relativistic pulsar winds may influence the relationship between P and $\dot{P}$.

2.1.2 *Pulsar winds*

Early studies of pulsars assumed that pulsars live in vacuum. Goldreich and Julian 1969 pointed out, however, that such vacuum assumption was not even valid in a simplified aligned rotator model where the magnetic axis and the rotation axis coincide: particles can be extracted from the neutron star surface resulting in a co-rotating magnetosphere filled with plasma and particles streaming out along the open magnetic field lines (see Fig. 2.3). In the aligned rotator model, a huge voltage difference is established by the giant rotating magnetic dipole, and the neutron star is operating like a unipolar generator. The electric potential obtained by solving Laplace's equation is:

$$\Phi(R,\theta) = -\frac{B_\star \Omega R_\star^2}{3c}\left(\frac{R_\star}{R}\right)^3 P_2(cos\theta) \,, \tag{2.9}$$

where r and θ are polar coordinates with θ measured from the rotation axis and $P_2(X) = \frac{1}{2}(3x^2 - 1)$ is the Legendre polynomial of second degree. The surface charge density on the star, $\sigma_\star$, can then be computed

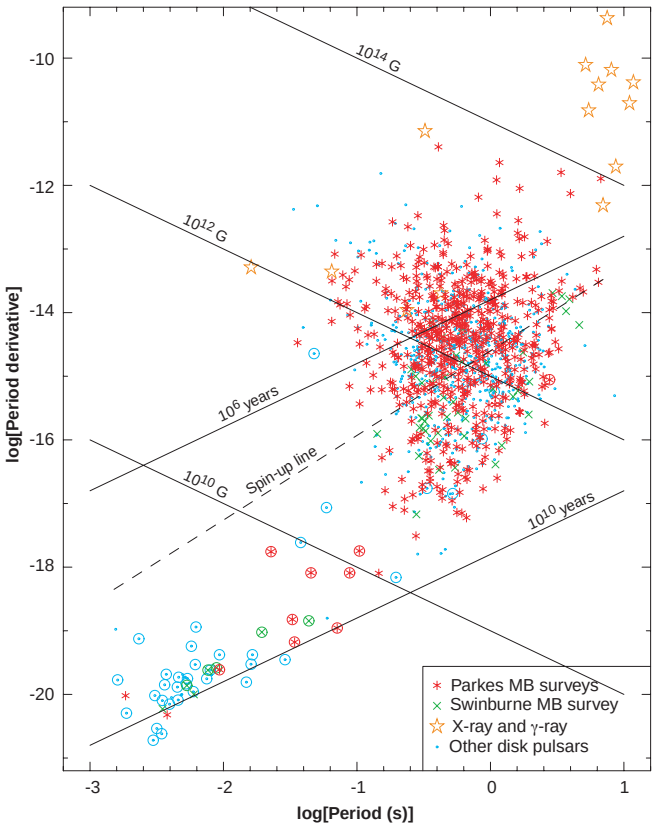

Figure 2.2: Distribution of P *vs* $\dot{P}$ for known pulsars in the Milky Way. Pulsars that have been detected only in the X-ray or gamma-ray energies are indicated by open stars; pulsars found in binary systems are indicated by a circle around the point. Lines of constant characteristic age and surface magnetic field are shown. The group of X-ray/gamma-ray pulsars in the upper right corner of the plot are slowly-spinning, highly magnetized pulsars known as magnetars. Figure adapted from Manchester 2004.

from the discontinuity of the normal component of the electric field at its surface,

$$\sigma_\star = -\frac{B_\star \Omega R_\star}{4\pi c} \cos^2\theta \ . \tag{2.10}$$

These charges can be pulled off the neutron surface easily by electric forces. For electrons, the electric force along the direction of the magnetic field can be 5×10^8 times larger than the gravitational force, and about 8×10^{11} larger for protons. The pulsar magnetosphere is thus considered to be filled with plasma that corotates with the pulsar inside the so called light-cylinder, with a radius $R_{lc} = c/\Omega$, at which the rotation velocity equals that of light. Beyond the light-cylinder, charged particles can stream out only along open field lines.

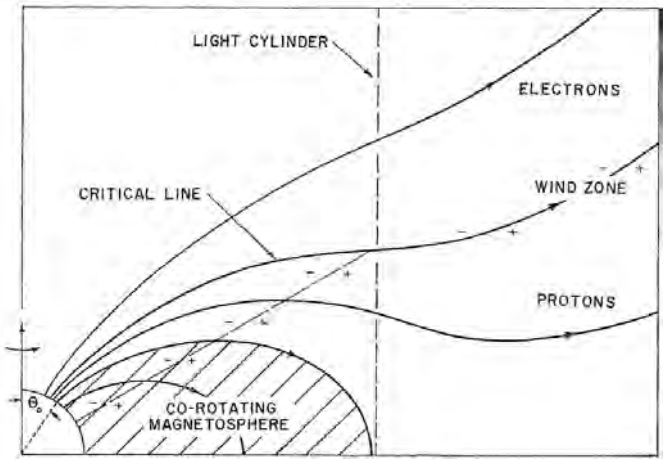

Figure 2.3: Schematic diagram showing the co-rotating magnetosphere and the wind zone from Goldreich and Julian 1969. The neutron star is at the bottom and left corner of the diagram.

The potential difference between the last closed magnetic field line ($\sin^2\theta = R_\star/R_{lc}$) and the neutron star pole is:

$$\Delta\Phi = \frac{B_\star \Omega^2 R_\star^3}{2c^2} \approx 6 \times 10^{12} \frac{{R_6}^3 B_{12}}{P^{-2}}\ V \tag{2.11}$$

which determines the maximum particle energy that can be achieved in the pulsar/PWN system. Additionally, this scenario also predicts a charge density commonly referred to as the Goldreich-Julian density:

$$\rho_{GJ} = \frac{\vec{\nabla}\cdot\vec{E}}{4\pi} = -\frac{\vec{\Omega}\cdot\vec{B}}{2\pi c}\frac{1}{\left[1-(\Omega r/c)^2\sin^2\theta\right]}. \tag{2.12}$$

The total flux of charged particles that can be released to the pulsar surroundings is constrained by the integral of this charge density over the polar cap region, which encompasses the open magnetic field lines, and assuming that particles are leaving the star at the speed of light. The particle extraction rate can then be calculated, yielding:

$$\dot{N}_{GJ} = \frac{B_\star \Omega^2 R_\star^3}{ec}\ . \tag{2.13}$$

Observational and theoretical constraints indicate nevertheless that the plasma in pulsar winds has to be much denser, far exceeding ρ_{GJ} or $\dot{N}_{GJ}$, for the observed PWNe luminosity to be attainable, and for the magnetohydrodynamic (MHD) assumption to be valid theoretically (Kennel et al. 1979). This difficulty can be however solved when considering pair creation processes in the pulsar magnetosphere (Sturrock 1971; Ruderman and Sutherland 1975; Arons and Scharlemann 1979; see also Timokhin and Harding 2019 for a recent discussion on this topic). Three regions are of interest for the pair production process to occur: the polar cap, the slot gap and the outer gap regions, where

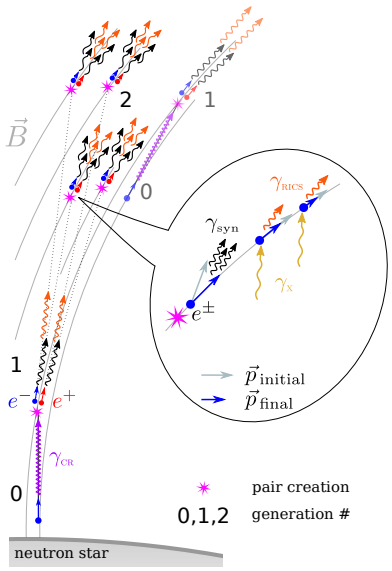

Figure 2.4: Schematic representation of the electron–positron cascades developing in the polar cap region of the neutron star. Several generations of particles are depicted, triggered by previous pair-created particles. Figure adapted from Timokhin and Harding 2019.

electric fields are considered unscreened, and from which coherent radio emission has been detected. Electrons/positrons first get accelerated in curved trajectories, generating curvature radiation. These curvature-generated photons further create electrons and positrons when interacting with the curved magnetic field. Electromagnetic cascades can then develop within a few stellar radii from the neutron star surface (see Fig. 2.4). The so-called pulsar multiplicity, k, defined as the ratio between the total charge flux and $\dot{N}_{GJ}$, is determined by this cascading process.

Whereas the magnetic field is mainly poloidal and particles move along the magnetic field lines near the pulsar, far away from the pulsar, in the pulsar wind zone, charges flow along open magnetic field lines that have a toroidal structure. Pulsar winds are therefore composed by a flux of charged particles, mainly electrons and positrons with maybe also a small amount of protons and ions, embedded in a strong magnetic field. These pulsar winds extend outwards away from the pulsar until the wind ram presure is balanced by the pressure of the surrounding medium, giving rise to the PWNe phenomenology.

2.1.3 *Pulsar wind nebula*

Rees and Gunn 1974 outlined the basic conceptual ideas about PWNe: the highly relativistic wind containing a toroidal magnetic field is terminated by a strong shock at a radial distance r_s from the pulsar.

At r_s, particles are randomized and energy is transferred to relativistic electrons which copiously emit synchrotron radiation. Based on these concepts, a self-consistent steady-state MHD model was later developed by Kennel and Coroniti in 1984 (Kennel and Coroniti 1984a) for the Crab PWN. They also coupled synchrotron emission to this MHD model under an *ad hoc* assumption that at the relativistic shock particles are accelerated to have a simple power-law energy distribution, which then is evolved along the outflow taking only adiabatic expansion and synchrotron energy losses into consideration (Kennel and Coroniti 1984b).

The model developed in (Kennel and Coroniti 1984a,b) is now commonly referred to as the "KC84" model, which originally described a simplified situation where the PWN freely expands into the SN ejecta. As displayed in Fig. 2.5, the flow in this model is divided into several regions:

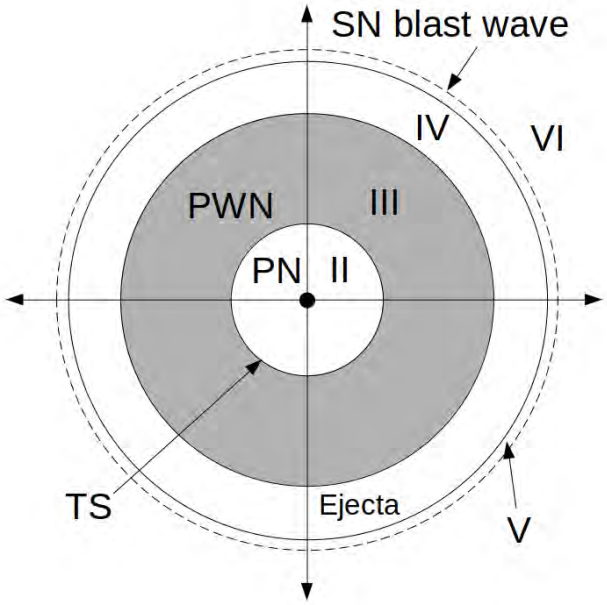

Figure 2.5: A simplified scheme of a spherically symmetric PWN inside of a supernova remnant, with regions labeled from I to VI defined to contain the pulsar, the cold pulsar wind, the shocked pulsar wind, the ejecta from the parent SN explosion and the shocked and unperturbed medium, respectively. Adapted from Kennel and Coroniti 1984a.

- Region I: The pulsar and its magnetosphere are located at the very center of the system.
- Region II: The cold pulsar wind consisting mainly of e^+ and e^- is produced in the pulsar magnetosphere and then streams out along the open magnetic field lines. This highly relativistic wind is terminated by a strong MHD shock, the termination shock (TS), whose radial distance from the pulsar can be estimated

from the observed size of the underluminous zone surrounding the pulsar.

- Region III. The nebula itself, defined as the region where the shocked pulsar winds are confined by the parent supernova remnant (SNR) that gave birth to the pulsar. In this region strong synchrotron emission from radio to X-rays is observed. The cooling time of particles losing energy via mainly through synchrotron radiation is energy-dependent, so the size of the nebula shrinks as energy increases.
- Region IV: This region encompasses the SN explosion ejecta surrounding the system.
- Region V: Shocked interstellar medium (ISM) together with heated ejecta are found in this region. The dashed outermost circle denotes the SN blast wave expanding into the ISM. If there is a reverse shock, some of the SN ejecta can be heated by it.
- Region VI: Unperturbed ISM.

The pulsar spin down luminosity channeling out through the magnetized relativistic pulsar wind until reaching the TS can be computed as:

$$\frac{dE}{dt} = \kappa \dot{N}_{GJ} m_e \Gamma_w c^2 \left(1 + \frac{m_i}{\kappa m_e}\right)(1+\sigma) \tag{2.14}$$

where Γ_w is the Lorentz factor of the flow, m_e is the electron mass, m_i is the ion mass, and the magnetization parameter, σ, stands for the ratio between the Poynting flux and the particle kinetic energy flux in the outflow:

$$\sigma = \frac{B^2}{4\pi n_e m_e \Gamma_w^2 c^2} \tag{2.15}$$

where n_e is the electron/positron density and B.

The TS of the pulsar wind is a perpendicular shock, assuming that the magnetic field is mainly toroidal far away from the pulsar. The following MHD conservation equations can then be derived for the particle number flux, the perpendicular component of the electric field,

the total energy, and the momentum carried by the flow (subscripts 1 and 2 refer to Region II and Region III defined above):

$$n_1 u_1 = n_2 u_2 \,, \tag{2.16}$$

$$E = \frac{u_1 B_1}{\gamma_1} = \frac{u_2 B_2}{\gamma_2} \,, \tag{2.17}$$

$$\mu_1 n_1 u_1 \gamma_1 + \frac{B_1^2}{4\pi}\frac{u_1}{\gamma_1} = \mu_2 n_2 u_2 \gamma_2 + \frac{B_2^2}{4\pi}\frac{u_2}{\gamma_2} \,, \tag{2.18}$$

$$\mu_1 n_1 u_1^2 + p_1 + \frac{B_1^2}{8\pi} = \mu_2 n_2 u_2^2 + p_2 + \frac{B_2^2}{8\pi} \,, \tag{2.19}$$

where n is the proper particle density, E and B are the shock frame electric and magnetic fields, u is the radial four speed of the flow ($u = \gamma\beta$), $\gamma^2 = 1 + u^2$, p is the pressure, and μ is the specific enthalpy, which for a gas with an adiabatic index Γ is defined by

$$\mu = mc^2 + \frac{\Gamma}{\Gamma - 1}\left(\frac{p}{n}\right) \,. \tag{2.20}$$

In the case of a cold highly relativistic wind $p_1 \ll n_1 mc^2$ and $\gamma_1 \approx u_1 \gg 1$. Considering also a strong shock approximation, $p_2/n_2 mc^2 \gg 1$, which means $\Gamma_2 = 4/3$, and assuming that $p_1 \sim 0$ and $u_2/u_1 \sim 0$, the Rankine-Hugoniot relations for a strong perpendicular shock are reduced to:

$$u_2^2 = \frac{8\sigma^2 + 10\sigma + 1}{16(1+\sigma)} + \frac{\sqrt{64\sigma^2(\sigma+1)^2 + 20\sigma(\sigma+1) + 1}}{16(\sigma+1)} \tag{2.21}$$

$$\frac{B_2}{B_1} = \frac{n_2\gamma_2}{n_1\gamma_1} = \frac{N_2}{N_1} = \frac{\gamma_2}{u_2} \tag{2.22}$$

$$\frac{p_2}{n_1 mc^2 \gamma_1^2} = \frac{1}{4u_2\gamma_2}\left[1 + \sigma\left(1 - \frac{\gamma_2}{u_2}\right) - \frac{\gamma_2}{\gamma_1}\right] \,. \tag{2.23}$$

For a non-relativistic unmagnetized (low σ) flow, one has:

$$u_2^2 \approx \frac{1+9\sigma}{8} \,, \gamma_2^2 \approx \frac{9+9\sigma}{8} \tag{2.24}$$

$$\frac{B_2}{B_1} = \frac{n_2\gamma_2}{n_1\gamma_1} = \frac{N_2}{N_1} = \frac{\gamma_2}{u_2} \approx 3(1-4\sigma) \tag{2.25}$$

$$\frac{p_2}{n_1 mc^2 \gamma_1^2} = \frac{2}{3}(1 - 7\sigma)) \,. \tag{2.26}$$

Downstream of the flow, after the TS, the basic equations for a steady flow in a toroidal magnetic field apply:

$$\frac{d}{dt}(cnur^2) = 0\,, \tag{2.27}$$

$$\nabla \times \frac{\mathbf{u}\times\mathbf{B}}{\gamma} = 0 \;\rightarrow \frac{d}{dr}\left(\frac{ruB}{\gamma}\right) = 0\,, \tag{2.28}$$

$$\frac{d}{dr}(nur^2 e) + P\frac{d}{dr}(r^2 u) = 0 \tag{2.29}$$

$$u\frac{d}{dr}(\gamma\epsilon) \equiv \frac{d}{dr}\left[nur^2\left(\gamma\, h + \frac{B^2}{4\pi n\gamma}\right)\right]\,, \tag{2.30}$$

where ϵ is the total electromagnetic plus kinetic energy per particle in the proper frame,

$$\epsilon = \mu + \frac{B^2}{4\pi n\gamma^2}\,. \tag{2.31}$$

One can solve these equations in the small σ limit for the velocity u and the magnetic field strength B of the flow in the nebula. Finally, assuming that the shock-accelerated particles follow a power-law distribution $\propto \epsilon_k^{-P}$, with $\epsilon_k = E/mc^2$ the normalised kinetic particle energy and P the distribution spectral index, one can compute the evolution of the particle energy in a steady flow:

$$u\frac{d\epsilon_k}{dr} = \epsilon_k u\frac{d}{dr} ln\; n^{1/3} - \frac{2}{3}\frac{e^4}{m^3c^5}B^2{\epsilon_k}^2 sin^2\theta \tag{2.32}$$

where θ is the pitch angle of the particle velocity with the magnetic field. One can then constrain the extended emission of the nebula considering e.g. adiabatic expansion energy losses as well as losses produced by synchrotron radiation.

2.2 OBSERVATIONS OF PWNE AT X-RAY WAVELENGTHS

So far $\sim$ 60 PWNe have been resolved in X-rays by *Chandra* and *XMM-Newton* thanks to deep observations carried along the last 20 years. The X-ray emission detected from PWNe is typically described using a power-law spectrum with a photon index Γ, whose value generally is within the range $1.5 \leq \Gamma \leq 2.2$ (Kaspi et al. 2006; Gaensler and Slane 2006).

PWNe display a truly variate morphology, but can be roughly divided into two classes: those featuring a torus-jet morphology, and those displaying cometary-tail structures (see e.g. Kargaltsev and Pavlov 2008), the difference between them being the speed of the pulsar with respect to the local sound speed, lower (higher) in the former (latter). It is to be noted that this morphological classification has been possible only since the launching of the NASA *Chandra* mission, and its unprecedented $\approx 0.5''$ resolution capability, which is required to study the global structure of PWNe in detail.

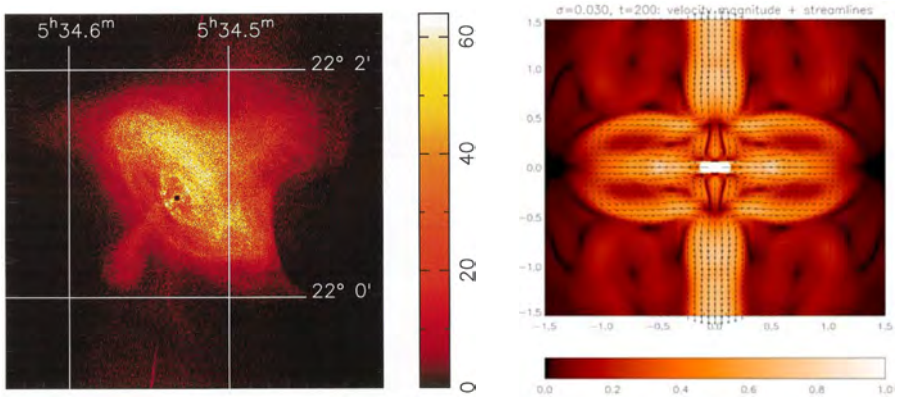

Figure 2.6: Left panel: *Chandra* image of the inner region of the Crab Nebula, in which a torus and two jet structures are clearly seen (figure from Weisskopf et al. 2000). Right panel: Numerical MHD simulation of the formation of torus and jets, performed right after the first resolved images of the source were provided in the early 2000's (figure from Del Zanna et al. 2004).

2.2.1 *Torus and jet-like structures in the Crab Nebula*

One of the most exciting discoveries made by *Chandra* was indeed the discovery of a torus and a jet structure at the center of the Crab Nebula (Weisskopf et al. 2000). These structures were not predicted previously, and deserved further theoretical modelling to explain the observed overall shape as well as the formation of these jet-like structures. In this regard, the torus structure was soon associated with the location of the TS of the pulsar wind. The non uniform morphology of the torus feature differs from the KC84 model since in that model one assumed that pulsar winds were isotropic, a non-valid assumption for an oblique rotator. When the pulsar rotation axis and magnetic axis do not coincide, the magnetic field will have an alternating polarity, stretching out and giving rise to striped winds separated by current sheets (Michel 1971; Coroniti 1990; Bogovalov 1999; Kirk et al. 2009). The wind energy flux is then anisotropic, $\propto sin^2(\theta)$, with its maximum value in the equatorial direction, which results in an oblate TS.

The jet-like features observed in the Crab Nebula, on the other hand, were more puzzling to interpret. Jet structures found e.g. in AGNs or Galactic microquasars are supersonic, well collimated outflows ejected from accretion processes on the central compact object. Magnetic collimation of ultrarelativistic pulsar winds is, on the contrary, extremely hard to achieve, and completely ineffective to explain the origin of pulsar jets. A theoretical framework had to be developed, in which these pulsar jets were interpreted as the result of magnetic hoop stresses channeling the shocked pulsar wind toward the pulsar rotation axis (Lyubarsky 2002). This theoretical interpretation of pulsar jets was later supported by 2D numerical MHD simulations (see e.g.

Komissarov and Lyubarsky 2004 and Del Zanna et al. 2004), which successfully reproduced the torus jet structure of the Crab Nebula.

2.2.2 *Bow Shock Pulsar Wind Nebulae (BSPWNe)*

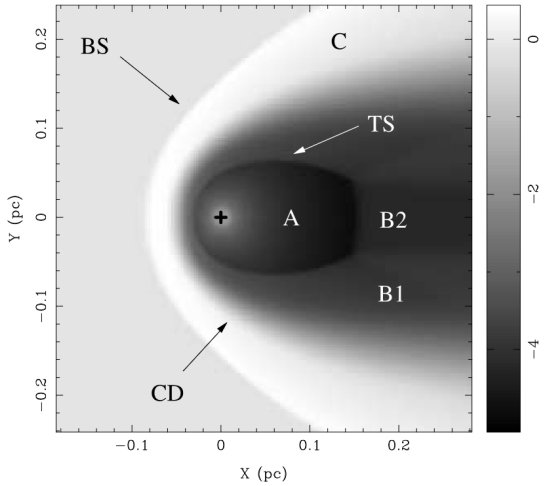

Figure 2.7: A 2D axially symmetric hydrodynamic simulation of a pulsar's bow shock, from Gaensler et al. 2004. The position of the pulsar is indicated by the "+" symbol; region A contains cold relativistic pulsar winds while shoced pulsar winds radiate sychrotron emission in region B. There is a CD seperating the shocked pulsar winds and the shocked ISM.

The distribution of the proper motion of isolated pulsars displays a maximum at velocities $\sim 400 - 500$ km/s (Hobbs et al. 2005). If a pulsar moves supersonically in the surrounding/ambient medium, the spherical geometry of its nebula can be strongly distorted, and the system will acquire a bullet-like morphology characterized by a bow-shaped shock and a cometary tail. This is found to be the case for relatively old runaway pulsars, as they have already escaped their parent SNR and are today moving through the ISM. Middle-aged pulsars, still confined in the SNR, may also develop cometary-tail extended structures in some circumstances (e.g. in the "Snail" nebula and PWN B1853+01 inside SNR W44). BSPWNe show in turn a variety of morphological shapes due to several geometrical factors, including the relative orientations of the pulsar rotation axis, the magnetic dipole axis, the pulsar velocity vector and the line of sight.

At the TS, the external ram pressure resulting from the pulsar's supersonic motion through the medium balances the bulk wind ram pressure. In the direction of the pulsar's motion, the distance to the TS (also referred as the "stand-off distance"), is defined through:

$$\frac{\dot{E}}{4\pi\omega R_0^2 c} = \rho_{ISM} v_{PSR}^2 \rightarrow R_{TS} = \sqrt{\frac{\dot{E}}{4\pi\omega\rho_{ISM} v_{PSR}^2}}\,, \tag{2.33}$$

where $\rho_{ISM} = m_p n_{ISM}$ is density of the ambient medium, $\dot{E}$ is the wind kinetic luminosity, and for an isotropic wind $\omega = 1$. The TS distance from the pulsar is a function of the angle with respect to the pulsar's proper motion direction, since the action of the ram pressure is not isotropic. The resulting bow shock shape can be geometrically described (see e.g.Wilkin 1996):

$$R(\theta) = R_{TS} \csc(\theta) \sqrt{3(1 - \theta \cot(\theta))}\,, \tag{2.34}$$

where θ is here the polar angle with respect to the direction of motion.

Numerical 2D axisymmetric hydrodynamic simulations of BSPWNe (see e.g. Bucciantini 2002; van der Swaluw et al. 2003; Gaensler et al. 2004) show that a contact discontinuity (CD) region exists separating the forward shock (FS) and the TS (see Fig. 2.7). The FS will heat up the ISM, with Hα emission from the shock region being detected in some cases (Bucciantini and Bandiera 2001). The TS on the other side of the CD terminates the pulsar wind. This shock is thought to be the site for very efficient particle acceleration, in which electrons and positrons can attain multi-TeV energies, radiating in X-rays (synchrotron) and gamma rays (through inverse Compton emission) (see Sect.n 2.4). The ultrarelativistic particles accelerated at the termination surface of the pulsar wind may undergo further reacceleration in the converging flow system formed by the plasma outflowing from the wind TS and the plasma inflowing from the bow shock (Bykov et al. 2017).

So far about 30 BSPWNe have been detected in the X-ray band. An updated list of BSPWNe can be found in Table 2.1. Images of some of these BSPWNe obtained with *Chandra* are shown in Fig. 2.8. As can be see from these *Chandra* images, several BSPWNe seem to be associated with jet-like features (see e.g. Kargaltsev et al. 2017). Some of these jet-like features have morphologies resembling an arc structure, and have been interpreted as a limb-brightened shell formed by the shocked PW downstream of the TS, or as pulsar jets bent by the ram pressure of the oncoming ISM. As an alternative explanation, Bandiera 2008 suggested that when the gyro-radii of the most energetic electrons is comparable to or exceed the stand-off distance of the bow shock, these particles cannot be contained within the bow shock, and can hence leak into the ISM, where they diffuse along the ambient ISM magnetic field lines while radiating synchrotron emission. Recent numerical simulations seem to largely support this interpretation (see e.g. Olmi and Bucciantini 2019b; Barkov et al. 2019b and references therein).

2.3 PARTICLE ACCELERATION IN PWNE

The spectrum of the electrons injected into the Crab Nebula inferred from observations displays a broad power-law distribution in energy, typically $\propto E^{-2}$, in a rather wide energy range, $10 \leq \gamma \leq 10^9$, with

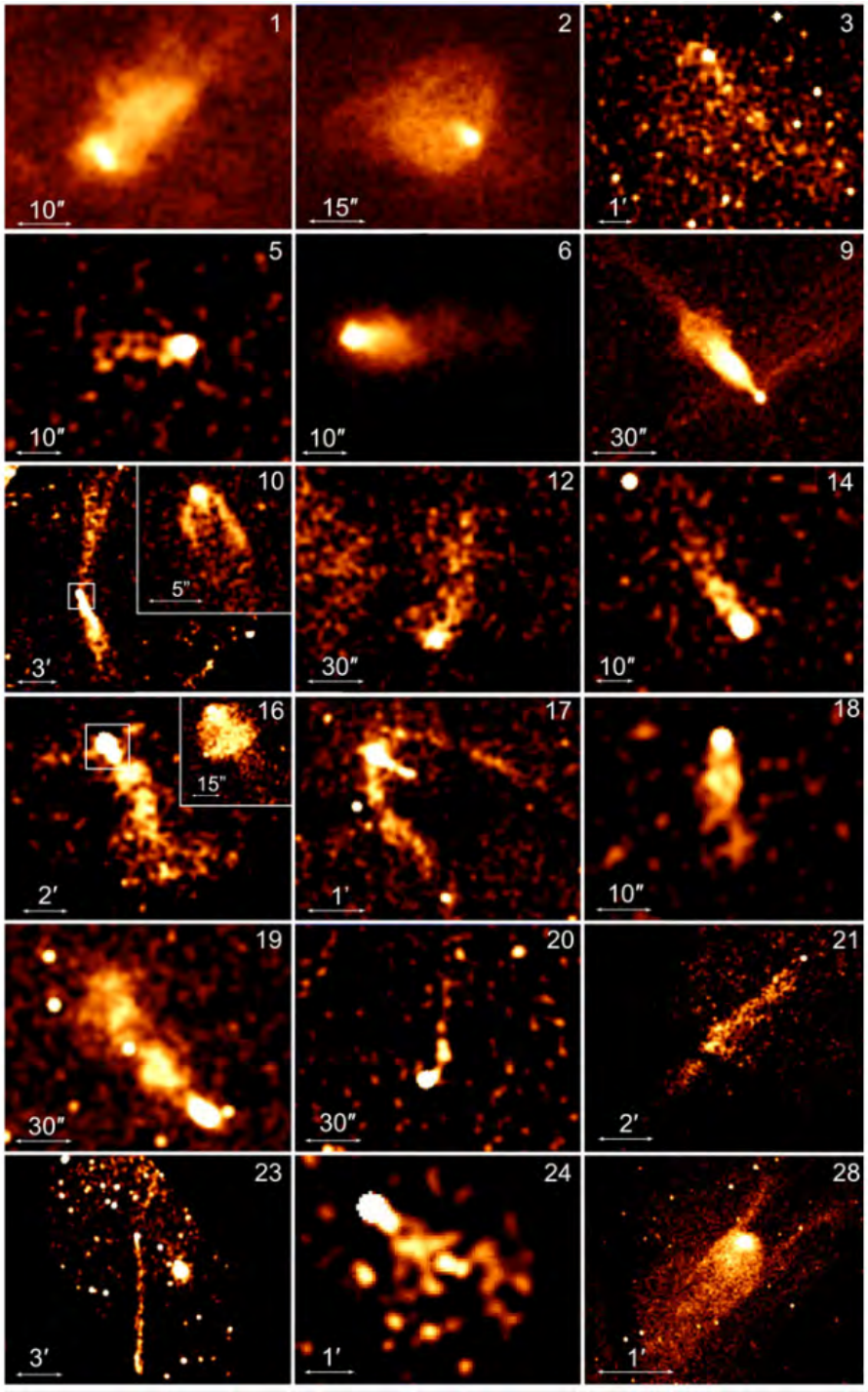

Figure 2.8: Chandra ACIS images of 18 SPWNe (figure from Kargaltsev et al. 2017). The panels are numbered in accordance with Table 2.1.

#	Pulsar	Associated Object(s)	d kpc	$\log \dot{E}$ erg s^{-1}	$\log \tau$ yrs	B_{11} 10^{11} G	$v_\perp$ km s^{-1}
1	J0537–6910[a]	SNR N157B	49.7	38.68	3.69	9.25	...
2	B1951+32	SNR CTB 80	3	36.57	5.03	4.86	460
3	J1826–1256	HESS J1825–137	$\sim 3.9^b$	36.56	4.16	37	...
4	B1706-44	SNR G343.1–2.3	2.6	36.53	4.24	31.2	$\lesssim 100$
5	B1757–24	SNR G5.27–0.9, Duck PWN	3.8	36.41	4.19	40.4	198
6	J1747–2958	Mouse PWN	5	36.40	4.41	24.9	306 ± 43
7	J1135–6055	...	$\sim 2.8^b$	36.32	4.36	30.5	< 330
8	J1437–5959	SNR G315.9–0.0, Frying Pan PWN	8	36.15	5.06	7.37	~ 300
9	J1101–6101	Lighthouse Nebula, SNR G290.1–0.8	$\sim 7^b$	36.13	5.06	7.24	~ 2000
10	J1509–5850	...	4	35.71	5.19	9.14	$200 - 600$
11	B0906–49	...	1	35.69	5.05	12.9	~ 60
12	B1853+01[a]	SNR W44	3.3	35.63	4.31	75.5	400^{+114}_{-73}
13	B0740–28	...	2	35.28	5.2	16.9	275^c
14	B1957+20	the Black Widow pulsar	1.73	35.20	9.18	0.002	~ 220
15	J0538+2817	SNR S147	1.39^p	34.69	5.79	7.33	357^{+59}_{-43}
16	B0355+54	Mushroom PWN	1.04^p	34.66	5.75	8.39	61^{+12}_{-9}
17	J0633+1746	Geminga PWN	0.25^p	34.51	5.53	16.3	~ 200
18	J2030+4415	...	$\sim 1^b$	34.46	5.74	12.3	...
19	J1741–2054	...	0.3	33.97	5.59	26.8	155
20	J2124–3358	...	0.41	33.83	9.58	0.003	75^c
21	J0357+3205	Morla PWN	0.5	33.77	5.73	24.3	~ 2000
22	J0437–4715	...	0.156^p	33.74	9.2	0.006	104.7 ± 0.9
23	J2055+2539[a]	...	$\sim 0.6^b$	33.69	6.09	11.6	$\lesssim 2300$
24	B1929+10	...	0.36^p	33.59	6.49	5.18	177^{+4}_{-5}
25	B2224+65	Guitar Nebula	1.88	33.07	6.05	26	1626
26	...	SNR IC443[a]	1.4	...	...	...	~ 250
27	...	SNR MSH 15–56, G326.3–1.8	4	...	...	...	100–400
28	...	G327.1–1.1, Snail PWN	7	...	...	...	~ 500

Table 2.1: List of BSPWNe detectd in X-rays, adapted from Kargaltsev et al. 2017.

a softening break at $\sim$ 500 GeV. The existence of electrons up to multi-PeV energies in this source (see the recent results reported by the LHAASO Collaboration, LHAASO Collaboration et al. 2021) and the incredibly high efficiency in converting pulsar rotation energy into kinetic energy, at the level of about 30% (Hester 2008), suggest that very efficient particle acceleration processes take place near the PWN TS (see e.g. the recent review in Amato 2024). The most widely considered acceleration mechanisms in PWNe are the First order Fermi process at the TS of the pulsar wind, and magnetic reconnection processes taking place in the wind, at the TS and downstream in the nebular region. Below we provide a brief general description of these acceleration mechanisms, whereas their application to the particular case of BSPWNe will be discussed in the following Chapters.

2.3.1 *Fermi acceleration*

The first-order Fermi acceleration process was developed based on the concept that particles crossing a strong shock front repeatedly will result in an efficient acceleration mechanism - first order in β, the shock velocity in units of the speed of light c (see e.g. Axford et al. 1977; Bell 1978; Blandford and Ostriker 1978). This Fermi acceleration process will yield a distribution in energy for the accelerated particles that follows a power law, with an index close to 2. This acceleration mechanism is also called diffusive shock acceleration (DSA) as it assumes that the accelerated particles diffuse back and forth the shock front. The DSA mechanism is the most commonly invoked particle acceleration mechanism in astrophysics. Its application and efficiency has been widely proven in the case of non-relativistic shocks (see e.g. Caprioli and Spitkovsky 2014).

The first version of the Fermi acceleration process (which was later renamed to second-order Fermi acceleration because its efficiency actually scales as the shock velocity to the power of 2) was proposed by Enrico Fermi in 1949 (Fermi 1949), which demonstrated that acceleration of relativistic particles can take place by repeated collisions with interstellar clouds acting as magnetic mirrors, so that particles are reflected back and forth almost isotropically, gaining energy on average after many collisions. The total kinetic energy of the cloud is largely unaffected, as the cloud is much more massive than the scattering particle, which after the scattering emerges from the cloud with a different (higher) energy and in a random scattered direction.

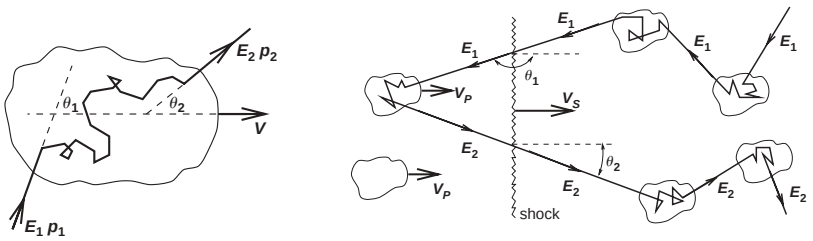

Figure 2.9: Sketch depicting the Fermi acceleration mechanism. The left panel shows the second-order mechanism, as originally envisaged by E. Fermi in 1949, in which a cosmic-ray particle scatters within a moving molecular cloud gaining energy ($E_2 > E_1$) and momentum and exiting the cloud in a randomised scattering angle. The right panel shows first-order Fermi acceleration of a cosmic ray particle scattering back and forth magnetic inhomogeneities across a strong shock, gaining energy and momentum at each crossing step, with an energy gain proportional to the shock velocity v_s. Figure adapted from (Protheroe and Clay 2004)

The exact amount of energy that the particle can gain can be derived by applying the Lorentz transformations between the laboratory frame and the cloud frame (see for instance Protheroe and Clay 2004). The averaged energy gain per collision is:

$$\frac{\Delta E}{E} \approx \frac{4}{3}\left(\frac{v_c}{c}\right), \tag{2.35}$$

where v_c is the cloud velocity. One can then calculate the average time between collisions, such that an energy rate can be derived from Eq. 2.35:

$$\frac{dE}{dt} \approx \frac{4}{3}\left(\frac{v_c^2}{cL}\right) E \equiv \alpha E, \tag{2.36}$$

where L is the mean free path between clouds, along the field lines. In order to find from this expression the final energy spectrum of the accelerated particles $N(E)$, one needs to solve the particle diffusion-loss equation in the steady state while considering this energy rate, assuming that the particles remain in the acceleration region for a given characteristic time t_{esc}:

$$N(E)\,dE = \text{cte} \times E^{1+\frac{1}{\alpha t_{esc}}}\,dE \tag{2.37}$$

This second-order Fermi acceleration mechanism is relatively inefficient, as it allows particles to gain energy at a rate that depends on the square of v_c/c, while the exponent of the resulting power-law distribution is rather uncertain as it depends on unconstrained values of αt_{esc}. For the observed low cloud densities in most astrophysical environments, the energy gain is therefore rather slow.

The original Fermi theory was later modified in the 1970s (see e.g. Bell 1978; Blandford and Ostriker 1978) to describe a more efficient acceleration mechanism, which is first-order in v_c/c. This new theory was initially invoked to explain particle acceleration in supernova shocks but is generally applicable to any strong shock in other astrophysical contexts, e.g. in the TS of PWNe. In these scenarios, a strong shock wave propagates radially out at a given speed v_s while the surrounding medium (for instance the supernova ejecta) and its associated magnetic field pile up in front of the shock, which moves at a velocity v_p. In the frame of the shock the gas flows from upstream into the shock with a given speed u_1 and a density ρ_1, and flows out of the shock in the downstream region with a given speed $u_2 = (v_s - v_p)$ and a density ρ_2. The relation between the velocities v_s and v_p depends on the ratio of specific heats Γ. The compression ratio R for a strong shock is defined as:

$$R = \frac{\rho_2}{\rho_1} = \frac{u_1}{u_2} = \frac{\Gamma+1}{\Gamma-1}, \tag{2.38}$$

and for a monoatomic ionized gas, $\Gamma = 5/3$; it turns out that the compression ratio for a strong shock is $R = 4$.

In order to obtain the energy gain per shock crossing in this scenario, one can consider the existence of magnetic irregularities tied to the outflowing plasma on either side of the shock as if they were clouds of magnetised plasma in the Fermi's original theory. Assuming that the relativistic accelerated particles are isotropically distributed at both sides of the shock, one can compute the rate at which particles cross the shock from downstream to upstream, and upstream to downstream (see e.g. Protheroe and Clay 2004):

$$\frac{\Delta E}{E} \approx \frac{4}{3}\left(\frac{v_p}{c}\right) \approx \frac{4}{3}\frac{(R-1)}{R}\frac{v_s}{c}\,, \tag{2.39}$$

which is therefore first-order in $\beta = v_p/c$, so the fractional energy change per collision can be much higher than in Fermi's original theory. The reason behind this is that in this strong shock scenario the converging flow as seen from both sides of the shock is approaching at a speed v_p.

Using the kinetic theory of particle transport, one can consider the probability for a particle to repeatedly escape the shock and enter the shock again (see e.g. Protheroe and Clay 2004). From this, one obtains the spectrum of accelerated particles:

$$N(E)\,dE = \text{cte} \times E^{-\Gamma} dE\,, \tag{2.40}$$

where $\Gamma \approx \frac{R+2}{R-1}$, which for a strong shock ($R = 4$) will give the well-known differential spectrum $\propto E^{-2}$.

This general framework of first-order particle acceleration through the Fermi mechanism seems nevertheless rather inefficient when applied to the case of PWNe. Numerical simulations show indeed that strong shocks triggered in a relativistic magnetized plasma as the one assumed to be in pulsar winds, particles cannot cross the shock back and forth unless a high level of magnetic turbulence is found in the downstream region (Sironi et al. 2013). This condition can be satisfied, however, if the magnetization parameter σ in the wind is low, $\sigma \lesssim 10^{-3}$. If that is the case, the spectrum of accelerated electrons is also a power law with an almost universal slope value of $\sim 2.2 - 2.3$, similar to what is inferred from X-ray observations of PWNe (Achterberg et al. 2001). Furthermore, in the case of relativistic shocks in a weakly magnetized plasma, electromagnetic plasma instabilities can develop. In particular, the so-called Weibel instability (Weibel 1959), triggered by a stream of shock-reflected particles propagating ahead of the shock, can build up a magnetic barrier that is sufficient to deflect the incoming particles and thus mediate the shock formation. This magnetic

structure adopts a filamentary geometry in the upstream region of the shock, and can in turn scatter the particles back and forth across the shock, accelerating particles up to highly relativistic energies via the aforementioned Fermi process (Spitkovsky 2008; Sironi and Cerutti 2017). In the case of PWNe, these instabilities can be produced by the turbulent medium in which the TS develops by large-scale shear flows in the nebula (see e.g. Komissarov and Lyubarsky 2004). If these large-scale motions drive a turbulent cascade to shorter wavelengths, they could indeed sustain Fermi acceleration to higher energies.

Fermi acceleration at the TS of PWNe is therefore a likely candidate for producing the accelerated particle distribution which would then be responsible for the observed X-ray emission via the synchrotron process. The steady state hard X-ray and gamma-ray spectra of PWNe do lead to inferred particle distributions following a power law $\propto E^{-p}$ with $p \sim 2.2 - 2.4$, which is a natural prediction of the Fermi process in relativistic shocks (see e.g. Kirk et al. 2000; Achterberg et al. 2001).

2.3.2 *Magnetic Reconnection*

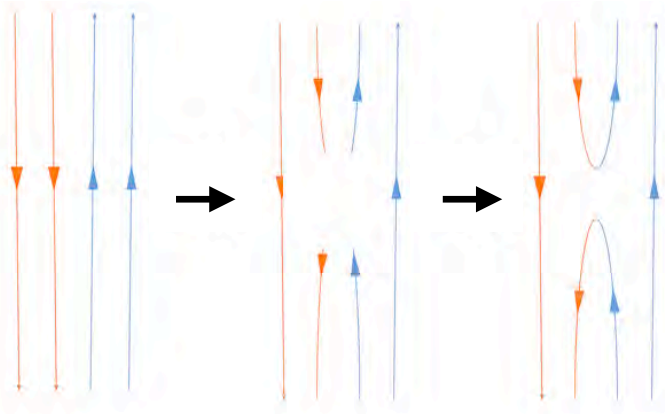

Figure 2.10: Sketch of the geometry of the field lines in magnetic reconnection. Oppositely directed magnetic field lines come into close contact and then reconnect giving rise to a different line structure. Figure adapted from The Sky's the limit's lectures "Magnetic reconnection: a prominent mystery"

Magnetic reconnection is an energy transfer process, in which magnetic Poyinting flux of a flow is converted to particle kinetic energy (Coroniti 1990; Michel 1994). In this energy transfer process, the flow heats up, and a non-thermal distribution tail can appear with a very hard spectral index, $\Gamma \leq 2$ (Sironi and Spitkovsky 2014). For pulsar winds, when the rotational and magnetic axes of the central pulsar are misaligned, the wind around the equatorial plane adopts a geometry in which toroidal stripes appear and feature an alternating magnetic polarity, with the stripes separated by current sheets of hot plasma

(the so-called "striped wind" pulsar wind structure, see e.g. Pétri and Lyubarsky 2007). It is today a matter of intense debate whether these alternating stripes can or cannot dissipate before reaching the TS (see e.g. Kirk and Lyubarsky 2001; Lyubarsky and Kirk 2001; Sironi and Spitkovsky 2011).

Once at the TS, the compression of the flow will force the annihilation of nearby field lines, a process known as driven magnetic reconnection (see e.g. Lyubarsky 2003). At this point magnetic reconnection erases the striped structure of the flow and transfers most of the energy stored in the magnetic fields to the particles. As a result of the magnetic field dissipation, the average particle energy increases across the shock. The incoming particles are accelerated by the reconnection electric field and, in the post-shock spectrum, they feature a broad distribution extending to much higher energies than expected in thermal equilibrium, resulting in a power-law with a slope as hard as $\lesssim 1.5$, much harder than what the Fermi process normally gives in relativistic shocks (Sironi and Spitkovsky 2014). Particle acceleration by magnetic reconnection has been invoked, in particular, to explain the gamma-ray flares detected from the Crab Nebula in recent years (see e.g. Cerutti et al. 2013).

2.4 NON-THERMAL EMISSION FROM PWN

Radiation from BSPWN is mainly produced through synchrotron and inverse Compton emission, which are responsible respectively for the radio to X-ray and gamma-ray fluxes observed in these sources. Below, a description of these two emission channels is provided.

2.4.1 *Synchrotron emission*

Particles with non relativistic velocities v gyrating in a magnetic field B with a pitch-angle θ with respect to the magnetic field orientation will have a gyration radius given by $r_g = \frac{mvsin\theta}{qB}$ and will radiate cyclotron radiation at a frequency $\nu_g = \frac{qB}{2\pi m_0}$ (or its angular analogue, $\omega_g = \frac{qB}{m}$). For relativistic particles the frequency spectrum is more complex, with gyration frequencies that can be much larger than the cyclotron frequency. The radiation from relativistic particles gyrating in the magnetic field is known as synchrotron radiation.

A relativistic particle with a Lorentz factor γ moving in a magnetic field will experience the Lorentz force:

$$\frac{d}{dt}(\gamma m_0 \vec{v}) = q(\vec{v} \times \vec{B}) \,, \tag{2.41}$$

where

$$\gamma = \sqrt{1 - \frac{\vec{v} \cdot \vec{v}}{c^2}} \tag{2.42}$$

is the Lorentz factor, m_0 is the rest mass of the charged particle and q is its charge. One can expand the left-hand side of the equation:

$$m_0 \frac{d}{dt}(\gamma \vec{v}) = m_0 \gamma \frac{d\vec{v}}{dt} + m_0 \vec{v} \frac{d\gamma}{dt}\,, \tag{2.43}$$

and since the three-acceleration $\vec{a} = d\vec{v}/dt$ is always perpendicular to $\vec{v}$,

$$m_0 \vec{v} \frac{d\gamma}{dt} = m_0 \gamma^3 \vec{v} \frac{(\vec{v} \cdot \vec{a})}{c^2} = 0\,. \tag{2.44}$$

One is left then with

$$\gamma m_0 \frac{d\vec{v}}{dt} = q(\vec{v} \times \vec{B})\,. \tag{2.45}$$

Splitting now the velocity into its parallel and perpendicular components with respect to the magnetic field, $v_{\parallel}$ and one perpendicular $v_{\perp}$, and using the pitch angle to θ as the angle between $\vec{v}$ and $\vec{B}$, one obtains:

$$\frac{d\vec{v}_{\parallel}}{dt} = 0\,, \qquad \frac{d\vec{v}_{\perp}}{dt} = \frac{q}{m_0 \gamma} \vec{v}_{\perp} \times \vec{B} = \frac{q|\vec{v}|Bsin\theta}{m_0 \gamma} \tag{2.46}$$

which implies that both $\vec{v}_{\parallel}$ and $|\vec{v}_{\perp}|$ are constant.

The solution to the equation of motion is a uniform circular motion of the projected motion on the normal plane, since the acceleration in this plane is normal to the velocity and of constant magnitude. The combination of this circular motion and the uniform motion along the field is a helical motion of the particle.

Equating this acceleration to the centripetal acceleration one obtains

$$\frac{|v_{\perp}^2|}{r_B} = \frac{q|\vec{v}|Bsin\theta}{m_0 \gamma}\,, \tag{2.47}$$

from which the Larmor radius can be defined:

$$r_L = \frac{m_0 \gamma |\vec{v}| sin\theta}{qB}\,, \tag{2.48}$$

and the frequency of the gyration is

$$\omega_B = \frac{qB}{\gamma m_0} = \frac{\omega_g}{\gamma},\ \nu_B = \frac{qB}{2\pi \gamma m_0} = \frac{\nu_g}{\gamma}\,. \tag{2.49}$$

A full description of the derivation of synchrotron radiation can be found in Pacholczyk 1970, Rybicki and Lightman 1986 and Longair 2011. The Larmor's formula for the radiation rate from a single accelerated particle with charge q and proper acceleration $\vec{a}_0$ ($\vec{a}_0^2 = \gamma^4[\vec{a}^2 + \gamma^2(\vec{v} \cdot \vec{a})/c^2]$), as measured in the instantaneous rest frame of the particle is:

$$P = \frac{2}{3}\frac{q^2|\vec{a}_0|^2}{4\pi\epsilon_0 c^3} = \frac{q^2\gamma^4}{6\pi\epsilon_0 c^3}\left[\vec{a}^2 + \gamma^2\left(\frac{\vec{v}\cdot\vec{a}}{c}\right)^2\right]. \tag{2.50}$$

The acceleration of the particle can be separated into components parallel $a_{\parallel}$ and perpendicular $a_{\perp}$ to the velocity vector $\vec{v}$, $|\vec{a}|^2 = |a_{\perp}|^2 + |a_{\parallel}|^2$, so that

$$P = \frac{q^2\gamma^4}{6\pi\epsilon_0 c^3}(|a_{\perp}|^2 + \gamma^2|a_{\parallel}|^2)\,. \tag{2.51}$$

For a relativistic particle that gyrates in a magnetic field in which $a_{\perp} = qvBsin\theta/\gamma m_0$ and $a_{\parallel} = 0$, one obtains:

$$P_{\rm syn} = \frac{q^2\gamma^4}{6\pi\epsilon_0 c^3}|a_{\perp}|^2 = \frac{q^4B^2}{6\pi\epsilon_0 c m_0^2}\frac{v^2}{c^2}\gamma^2 sin^2\theta\,, \tag{2.52}$$

which can be rewritten as:

$$P_{\rm syn} = 2c\left(\frac{e^4}{6\pi\epsilon_0^2 m_0^2 c^4}\right)\left(\frac{v}{c}\right)^2\frac{B^2}{2\mu_0}\gamma^2 sin^2\theta = 2c\sigma_T U_B\left(\frac{v}{c}\right)^2\gamma^2 sin^2\theta\,. \tag{2.53}$$

where σ_T is the Thomson cross section and U_B is the magnetic energy density. Averaging over an isotropic distribution of pitch angles, the average radiation power is:

$$< P_{\rm syn} >= \frac{4}{3}c\sigma_T U_B\left(\frac{v}{c}\right)^2\gamma^2. \tag{2.54}$$

The power per unit frequency emitted by the particle in the ultra-relativistic limit is:

$$P(\nu) = \frac{\sqrt{3}q^3B}{4\pi\epsilon_0 m_0 c}sin\theta F\left(\frac{\nu}{\nu_c}\right) \tag{2.55}$$

where $\nu_c \equiv \frac{3}{2}\gamma^3\nu_B sin\theta$ is the so-called critical frequency, and

$$F(x) \equiv x\int_x^{\infty} K_{5/3}(z)dz, \tag{2.56}$$

with $K_{5/3}$ being the Bessel function of the second kind. Asymptotic expressions of $F(x)$ at two extreme ends ($x \ll 1$ and $x \gg 1$) are:

$$F(x) \sim \frac{4\pi}{\sqrt{3}\Gamma\left(\frac{1}{3}\right)\sqrt[3]{2}}x^{\frac{1}{3}},\ x \ll 1\,, \tag{2.57}$$

$$F(x) \sim \left(\frac{\pi}{2}\right)^{\frac{1}{2}}e^{-x}x^{\frac{1}{2}},\ x \gg 1\,. \tag{2.58}$$

The spectrum (the spectral flux) of the synchrotron radiation from an individual electron peaks at the frequency given by $\nu \simeq 0.29\nu_c$.

Electrons radiating synchrotron emission will cool down. The synchrotron cooling time scale is given by:

$$t_{\rm syn} \equiv \frac{E}{< P >} = \frac{\gamma m_0 c^2}{\frac{4}{3} c \sigma_T U_B \left(\frac{v}{c}\right)^2 \gamma^2} = \frac{9\pi\epsilon_0 m_0^3 c^5}{q^4 v^2 B^2 \gamma}\,. \tag{2.59}$$

In the case of a power-law distribution of electrons, $N(E) = KE^{-P}$ in the range $E_1 < E < E_2$, and assuming that electrons with energy E and Lorentz factor γ radiate mostly at the critical frequency ν_c, the total energy radiated in the frequency range $[\nu, \nu + d\nu]$ is given by:

$$J(\nu)d\nu = < P_{\rm syn}(E) > N(E)dE\,, \tag{2.60}$$

so the synchrotron specific emissivity is:

$$J(\nu) \propto K B^{\frac{P+1}{2}} \nu^{-\frac{P-1}{2}}, \tag{2.61}$$

with the synchrotron emission spectral index α that will depend on the index of the particle distribution P and is defined as $J(\nu) \propto \nu^{-\alpha}$, so $\alpha = \frac{P-1}{2}$. At X-ray wavelengths, however, photons are treated like particles and one usually "counts" them. The spectrum is typically defined as $N_{\rm ph}(E) \propto E^{-\Gamma_{\rm ph}}$ where the photon index is $\Gamma_{\rm ph} = \alpha + 1$.

2.4.2 *Inverse Compton emission*

In the case of PWNe the energetic electron population that produces synchrotron radiation in the keV X-ray energy range also could interact with the ambient photon field and produce gamma-rays via the inverse-Compton (IC) scattering of those photons (Atoyan and Aharonian 1996). The cosmic microwave background, or diffuse infrared and optical radiation of Galactic origin, can be the ambient photons acting as IC targets.

For target photon energies $h\nu \ll m_e c^2$ in the rest frame of the electron, the interaction is basically elastic; this is known as the Thomson regime. Otherwise, when $h\nu \gtrsim m_e c^2$ in that frame, the recoil of the electron under Compton scattering cannot be neglected and the interaction is no longer elastic (among other effects of quantum nature); this is known as the Klein-Nishina regime. The Klein-Nishina QED cross section in the electron frame, which accounts for both the Thomson and the Klein-Nishina regimes, for an isotropic target photon field as expected in PWNe, is (Longair 2011):

$$\sigma_{\rm KN} = \pi r_e^2 \frac{1}{x}\left\{\left[1 - \frac{2(x+1)}{x^2}\right] ln(2x+1) + \frac{1}{2} + \frac{4}{x} - \frac{1}{2(2x+1)^2}\right\} \tag{2.62}$$

where $x = h\nu/m_e c^2$ and $r_e = e^2/4\pi\epsilon_c m_e c^2$ is the classical electron radius. In the ultra-relativistic limit, the cross section can be written as:

$$\sigma_{\rm KN} \approx \pi r_e^2 \frac{1}{x}\left(ln2x + \frac{1}{2}\right) . \tag{2.63}$$

In the ultra-relativistic case, the cross section is largely reduced with respect to the Thomson cross section, which as mentioned is relevant for low photon energies (i.e. $h\nu \ll m_e c^2$). In the latter case, however, $\sigma_{\rm KN}$ becomes equal to the classical case of Thomson scattering where the electron radiates oscillating and producing emission in response to the incoming electromagnetic waves. In that regime, the total cross-section $\sigma_{\rm T}$ for scattering of electromagnetic waves by electrons is:

$$\sigma_{\rm T} = \frac{e^4}{6\pi\epsilon_0^2 m_e^2 c^4} \approx 6.65 \times 10^{-25} cm^2. \tag{2.64}$$

In the Thomson regime, the frequency of the radiation is left unchanged in the electron rest frame, which means that the electron energy in the lab frame is also not significantly changed due to one interaction in the Thomson regime, unlike interactions occurring in the Klein-Nishina regime, where even one interaction can already significantly decrease γ. In the context of relativistic electrons scattering ambient photons in PWNe, albeit small, a transfer of energy from the electron to the photo still takes place, and thus the radiation process is called inverse Compton scattering. In most of the following discussion, we nevertheless assume that the interaction takes place in the Thomson regime, as it applies for a broad energy range of the relativistic electrons in PWNe. For the highest energy electrons the Klein-Nishina regime can however become relevant.

In what follows, the laboratory frame of reference is denoted by S, and the rest frame of the electron by S'. To calculate the power per electron channeled into the IC scattered radiation, $P_{\rm IC}$, in the Thomson regime, we consider that the energy of the target photon in S is much less than $m_e c^2/\gamma$ (equivalent to $h\nu' \ll m_e c^2$ in S', where $\nu = \nu'/\gamma$), with γ being the electron Lorentz factor. After transforming the energy of the scattered photon to S' and then back to S, the photon energy gets boosted by γ^2. This means that

$$P_{\rm IC} = \frac{4}{3}\sigma_T c U_{\rm rad}\left(\frac{v}{c}\right)^2 \gamma^2, \tag{2.65}$$

where $U_{\rm rad}$ is the the energy density of the target photons. The spectral index of the scattered radiation is $\alpha = (P-1)/2$, where P is the index of the electron energy distribution, which typically follows a power-law (i.e. $N(\gamma) \propto \gamma^{-P}$).

If the electron-photon interaction is head-on in S, the maximum energy of the scattered photon in an IC collision is:

$$(h\nu_{sc})_{\rm max} \approx 4\gamma^2 h\nu_0 . \tag{2.66}$$

The average energy of the scattered photons when dealing with an isotropic electron distribution is

$$< h\nu_{sc} > \approx \frac{4}{3}\gamma^2 h\nu_0 \,. \tag{2.67}$$

The $4/3$ in this expression corresponds to the $4/3$ present in Eq. (2.65). For simplicity, more in general one can adopt

$$\nu_{sc} \approx \gamma^2 \nu_0 \,, \tag{2.68}$$

which applies as long as the scattering angle in S is not $\ll \pi$. We note that deep in the Klein-Nishina regime, $h_{sc}\nu \approx \gamma m_e c^2$.

A discussion on the particle and photon energy distributions associated to the synchrotron and IC processes can be found in Bosch-Ramon 2008. Depending on the cooling and IC regime, the gamma-ray spectrum can appear softer or harder, which can determine the detectability of the source.

2.5 PARTICLE ESCAPE FROM PWNE

The possibility for particles accelerated in PWNe to escape the surrounding medium strongly depends on the evolution of the PWN inside its parent SNR. This evolution can be rather complex, as it involves not only the evolution of the SNR, but also the interaction between the SNR and the PWN. Below we provide a brief summary of the different evolutionary stages for both SNR and PWNe. Thereafter, our current understanding of particle escape mechanisms occurring in BSPWNe is presented.

2.5.1 *Evolution of SNRs*

The evolution of the SNR in the ISM is typically divided into 4 different phases (Reynolds 2008; Vink 2020; Bamba and Williams 2022), and needs to consider also the circumstellar medium (CSM) which, different from the ISM, will be strongly affected by the stellar winds of the progenitor star.

- Free expansion phase. The supernova ejecta expands with a velocity $v_s = (2E_{\rm SN}/M_{\rm ej})^{1/2} \sim 5000$ km s^{-1}, with $E_{\rm SN}$ being the total energy output in the explosion and $M_{\rm ej}$ the total ejected mass. This velocity is much larger than the sound speed c_s in the ISM, of order of 1-10 km s^{-1}. The ejecta drives in this way a strongshock wave into the ISM with a very high Mach number ($M \gtrsim 10^3$). The radius of the shock increases linearly with time, $R_s = v_s t$.

- Adiabatic phase (or Sedov-Taylor phase). This phase begins when the amount of accumulated material from the surrounding medium (characterised by a particle density n_0) swept up

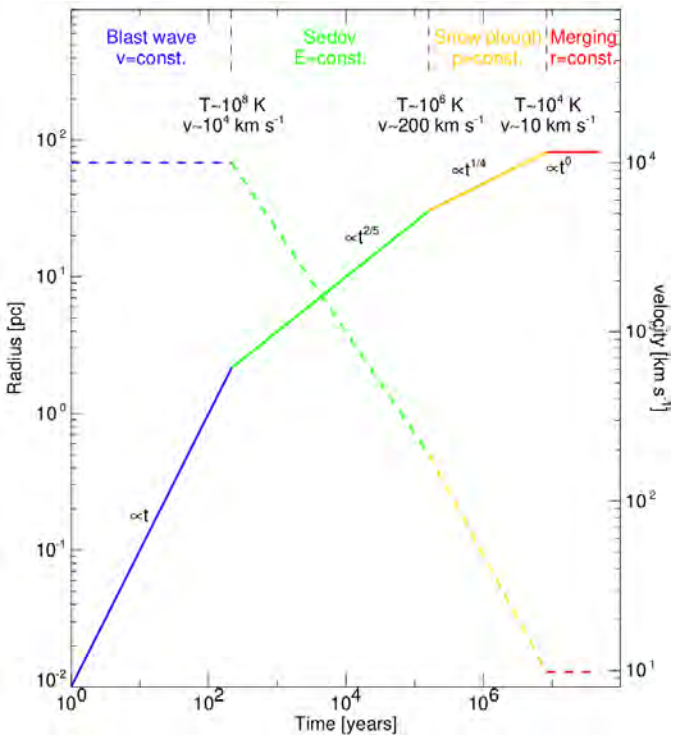

Figure 2.11: The evolution of SNR shock velocity (dashed line) and radius (solid line). Figure from Padmanabhan 2000.

by the shock front approaches the total mass contained in the outflowing ejecta, $\frac{4\pi}{3} n_0 R_s^3 \approx M_{ej}$. At this stage, the shock front evolves into a more complex structure, with a forward shock propagating outwards into the CSM and a reverse shock moving inwards towards the unshocked ejecta. When the reverse shock reaches the center of the SNR, its interior will be filled with shock-heated ejecta, and the SNR is in a fully self-similar stage. The evolution of the shock wave then can be characterised by a self-similarity solution: $R_s \propto t^{2/5}$ and $v_s \propto t^{-3/5}$ (Sedov 1959; Cox 1972). An estimation of the time it takes for the reverse shock to reach the center of the SNR is given by (Reynolds and Chevalier 1984):

$$t_{\rm cross} = 1 \times 10^4 \left(\frac{M_{\rm ej}}{15 M_\odot}\right)^{\frac{5}{6}} \left(\frac{E_{\rm SN}}{10^{51}{\rm ergs}}\right)^{-\frac{1}{2}} \left(\frac{n_0}{1{\rm cm}^{-3}}\right)^{-\frac{1}{3}} {\rm yr}\,. \tag{2.69}$$

- Radiative phase. The shock front continues expanding while the energy losses caused by thermal radiation become significant, so that the energy conservation assumed in the Sedov phase is not valid anymore. In this phase, $R_s(T) \propto t^{1/4}$ and $v_s \propto t^{-3/4}$.

- Dissipative phase: the velocity of the SNR forward shock decreases down to a value close to c_s, the SNR starts to dissolve and blend into the ISM.

A sketch displaying the evolution of the SNR shock radius as well as the shock velocity with time for the four different phases is displayed in Fig. 2.11.

2.5.2 *Evolution of PWNe*

A PWN can be considered as a bubble of relativistic winds and fields inflated by the central pulsar born in the parent supernova explosion. PWNe are therefore initially contained within the expanding supernova ejecta. Its evolution will depend on the interaction between the SNR reverse shock and the PWN. The averaged "kick" velocity in recently born pulsars is ~ 400 km/s (Hobbs et al. 2005), whereas the SNR shell decelerates as described in last section (see Fig. 2.11). The evolution of a PWN inside of a SNR can be divided into four different stages (Gaensler and Slane 2006; Olmi and Bucciantini 2023):

- Supersonic expansion stage: the PWN is located at the center of the SNR and expands into the freely expanding ejecta. In a spherically symmetric case, the radius of the PWN's forward shock is $R_{\rm PWN} \propto t^{6/5}$ (Chevalier 1977). A textbook example of a PWN in this stage is the PWN powered by PSR J1833-1034 at the center of the SNR G21.5–0.9 (Matheson and Safi-Harb 2010).

- Reverse shock interaction stage: the SNR reverse shock moves inwards to the center of the SNR and it arrives to its center at time t_{cross} (see Eq. 2.69), typically of a few thousand years. The PWN is compressed by the hot SNR ejecta by a large factor, and suddenly reverted into a new expansion. the PWN undergoes a reverberation phase until the system reaches a new equilibrium.

- Subsonic expansion stage: the PWN expands subsonically into the remnant as the interior of the SNR has been re-heated by the reverse shock and the sound velocity has increased by a large factor.

- Bow shock stage: the sound speed in the shocked ejecta drops as the pulsar moves from the center to the edge of the SNR. Eventually the pulsar motion becomes supersonic, and it now drives a bow shock through the SNR interior (Chevalier 1998; Van Der Swaluw et al. 1998). For a SNR in the Sedov phase, the PWN transition to the bow shock phase takes place when the pulsar has moved about two thirds of the distance between the center and the forward shock of the SNR (van der Swaluw et al. 2003). An example of such a system is PSR B1853+01 in the SNR

W44, as discussed in Chapter 5. A pulsar moving with velocity $V_{\rm PSR}$ will escape while the parent SNR is still in the Sedov phase at a time (van der Swaluw et al. 2003):

$$t_{\rm esc} \approx 45 \left(\frac{E_{\rm SN}}{10^{51}\ {\rm ergs}}\right)^{\frac{1}{3}} \left(\frac{n_0}{1\ {\rm cm}^{-3}}\right)^{-\frac{1}{3}} \left(\frac{V_{\rm PSR}}{400\ {\rm kms}^{-1}}\right)^{-\frac{5}{3}} {\rm kyr}\,, \tag{2.70}$$

and because typical sound speed values are approximately 1, 10, and 100 km s^{-1} for the cold, warm, and hot components of the ISM, respectively, the pulsar will move supersonically and drive a bow shock through the ISM. For typical pulsar and ISM parameters, most pulsars are expected to leave their parent SNRs during the Sedov-Taylor phase of remnant expansion.

2.5.3 *Particle escape*

It is worth noting that the last BSPWN phase in the evolution of a PWN described above corresponds to stages 2 and 3 in Giacinti et al. 2020 (see Fig. 2.12), where energetic electrons would be able to escape the PWN/SNR system, diffuse into the ISM and then, upon up-scattering ambient photons, give rise to the observed extended TeV emission via IC process. The extended TeV emission observed at VHE gamma-rays around a number of PWNe are called "TeV halos".

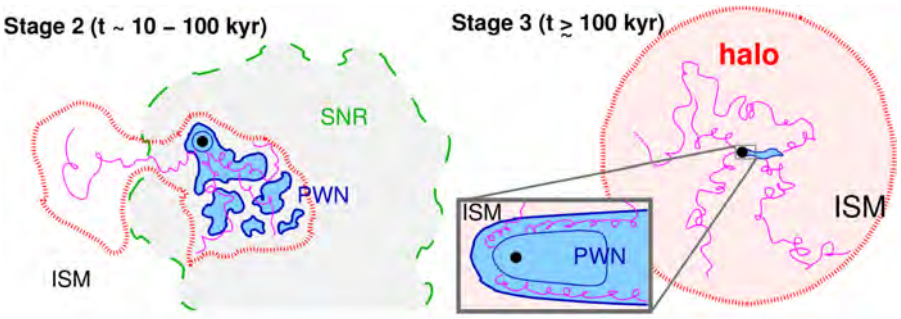

Figure 2.12: Sketch of the two evolutionary stages of a PWN where energetic particles escape the PWN forming the so called "TeV halo", from Giacinti et al. 2020. **Left**: The PWN is crashed by the reverse shock while the pulsar is still in its SNR. **Right**: The pulsar has escaped from its parent SNR and/or the parent SNR has dissolved in the ISM.

The jet-like structures observed in X-rays in recent years in BSPWNe systems mentioned earlier (see Sec. 2.2.2), also suggest energetic particles escaping the PWNe. On theoretical grounds recent numerical simulations (Bucciantini 2018; Olmi and Bucciantini 2019a,b; Barkov et al. 2019a,b) suggest that particles can escape the bow shock through at locations in the CD where enhanced magnetic reconnection is taking place. In particular Olmi and Bucciantini 2019b suggests that the

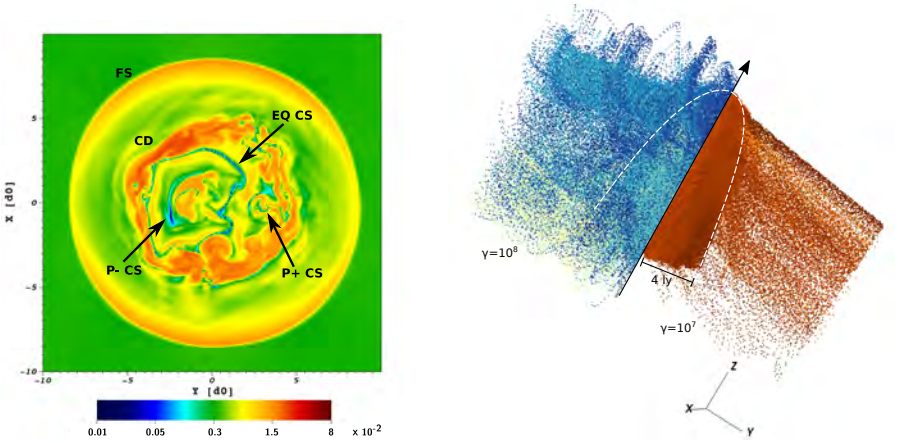

Figure 2.13: **Left**:Transverse section of the BSPWN tail showing the intensity of the magnetic field. Polar current pointing along the direction of the pulsar velocity (P+CS) is largely affected by the turbulent CD. **Right**: Particles escaping from the BSPWN. High energy particles with gyroradius larger than the size of the bowshock diffusively escape. For lower energies, particles tend to escape from the head of the bow shock where magnetic reconnection with ISM magnetic field lines occurs. Figures extracted from Olmi and Bucciantini 2019b and Olmi and Bucciantini 2023.

magnetic field lines associated to the polar current pointing along the direction of the pulsar motion tend to reconnect with the ISM magnetic field (see Fig. 2.13). These polar currents can have different orientations with respect to the velocity of the pulsar so that the jet-like features observed in X-rays will show a asymmetric profile. In this regard, the simulations in (Barkov et al. 2019b) consider different orientations for the pulsar rotation axis, the pulsar magnetic axis, and the external magnetic fields. They also conclude that for certain orientations, the formation of the so-called "magnetic bottles" in reconnection processes can lead to the observed jet versus counter-jet asymmetry.

The transport of the escaped electrons in the ISM can then be characterized using a diffusion model. The evolution of a relativistic particle population is determined by the diffusion-loss equation (Ginzburg and Syrovatskii 1964; Longair 2011):

$$\frac{\partial n}{\partial t} - D\nabla^2 n + \frac{\partial (bn)}{\partial E} + \frac{n}{T} = 0 \tag{2.71}$$

Where E is the particle energy, n the particle density, $b = \frac{dE}{dt}$ are the particle losses, and T is the particle escape time scale. The diffusion coefficient D may be different in the surroundings of some PWNe, as found within the TeV Halos interiors, which seem to have a rather small value compared to the one that characterizes the diffusion of Galactic cosmic rays (Abeysekara et al. 2017).

2.6 SOURCES OF INTEREST

At the early stages of this PhD Thesis, a selection of four potentially interesting BSPWN was performed, largely based on the increasing number of cases detected by *Chandra* (see e.g. Table 2.1 adapted from Kargaltsev et al. 2017): PWN B1757-24, PWN J1135-6055, PSR B1853+01 and the PWN in IGR J11014-6103, the Lighthouse nebula.

PSR B1757-24 is a young and energetic pulsar, with a period $P = 125$ ms, a high spin-down energy-loss rate of $\dot{E} = 10^{36.4}$ erg s^{-1}, and a characteristic age $\tau_c = P/2\dot{P} = 15.5$ kyr (Manchester et al. 1991). The PWN powered by PSR B1757-24 is located just outside the westernmost parts of the SNR G5.4-1.2, and displays a marked cometary-like morphology. The association with G5.4-1.2 implies a proper motion of PSR B1757-24 of $\sim$ 1500–2000 km s^{-1} (Frail et al. 1994). Observations of PSR B1757-24 and its nebula with *Chandra* for a total exposure time of $\sim$20 ks, revealed a fainter extended emission (likely the PWN tail) on the eastern side of the source (Kaspi et al. 2001) similar to the extended nebular observed in the radio band (Frail et al. 1994). Also there seems to be a hint of a jet-like feature towards the north of the pulsar. The relatively low statistics obtained from the tail yielded a rather poor spectral fit. The best-fit photon index assuming a power-law distribution was found to be very hard, but with large uncertainties $\Gamma = 1.0 \pm 0.6$ and $\chi^2_{\rm red}(d.o.f.) = 2.0$ (4). To better characterize the tail structure, both morphologically and spectrally, and to search for jet-like structures in this BSPWN, we proposed twice for a deep *Chandra* observation in cycle 22 and cycle 23. The proposals and their science potential were acknowledged, but they did not receive the required prioritization in the *Chandra* scheduling.

Since it was not possible to acquire new data on PWN B1757-24, this source is not further discussed in this Thesis. For the studies related to the other three sources, the reader is referred to Chapters 4, 5 and 6 for PWN J1135-6055, PSR B1853+01 and IGR J11014-6103, respectively.

3

OBSERVING X-RAY EMISSION FROM PWNE

Particles emitting X-ray radiation through synchrotron emission have typically very short lifetimes (e.g. the characteristic synchrotron cooling time for electrons emitting at 1 keV in a magnetic field of $\sim 50\ \mu$G is only ~ 100 yrs). Observations in the X-ray band are therefore capable to trace in almost "real time" the dynamics of pulsar outflows, which can become essential to understand the acceleration and transportation mechanisms taking place in PWNe.

Different from radio and ground-based observatories, X-ray telescopes have to be carried by balloons or installed in satellites since the molecules composing the atmosphere gas absorb most of the X-rays arriving at Earth (see Fig. 3.1).

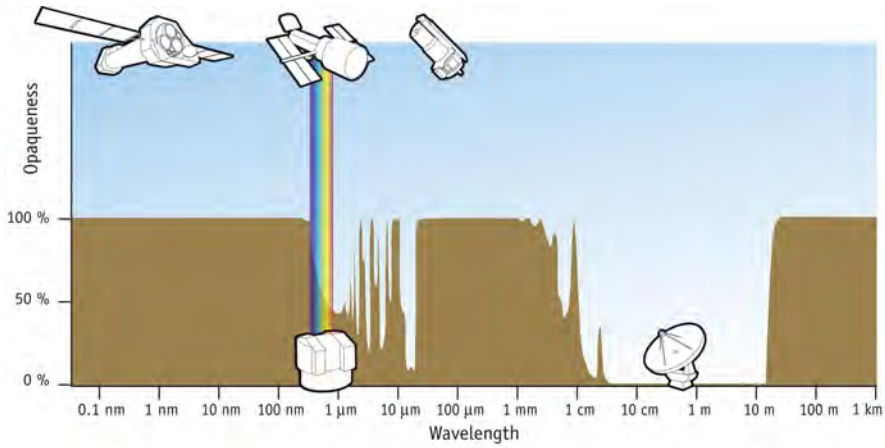

Figure 3.1: Absorption of electromagnetic radiation by Earth's Atmosphere. Credit: NASA

The first detection of X-ray emission with a cosmic origin came in 1949, when radiation detectors installed on rockets were able to record photons from the most intense X-ray source in the sky, the Sun. The improvement of detectors in the following decade brought the detection of new sources beyond our Solar system, e.g. with the NASA's Uhuru mission, launched in 1970. Further technological advancement, particularly regarding improved detector capabilities, led to the operation of X-ray observatories like Einstein, ROSAT or ASCA, among others.

In the past two decades, instruments like *Chandra*, *XMM-Newton* or *NuSTAR* have revolutionized our understanding of PWNe. *Chandra* proved great success in resolving PWNe with its unprecedented subarcsec angular resolution. *XMM-Newton* with excellent sensitivity make detection of faint emission possible. *NuSTAR* as the first focusing

telescope in hard X-ray energy range now allows us to observe PWNe and other sources up to 79 keV with far improved resolution. Thanks to these developments, the discovery rate in X-ray astronomy in the last 50 years can be compared to that of optical astronomy in the last 400 years.

3.1 X-RAY TELESCOPES

The design of X-ray telescopes is quite different from that of optical telescopes. X-rays have a much shorter wavelength, so when they strike the mirror surfaces nearly perpendicularly they are either transmitted or absorbed. In fact, the more energetic X-ray photons are, the harder it is to get them focused. At the high-energy end of the X-ray band, at energies above $\sim$ 10 or 80 keV, non-imaging instruments such as scintillators have been often used, e.g. in the HXD detector onboard Suzaku (Takahashi et al. 2007)). For imaging purposes, collimator or pseudo-imaging techniques such as coded-aperture masks have also been developed and successfully exploited (e.g. the detectors of the INTEGRAL mission, JEM-X, IBIS and SPI, the latter one reaching up the soft gamma-ray band, up to 8 MeV; Winkler et al. 2003). Coded-mask instruments, however, feature a wide point spread (response) functions (PSFs), and therefore a a low angular resolution and a relatively high background contamination, affecting their sensitivity.

Soft to medium-energy X-rays (energies in the range $\sim$ 5 - 10 keV) can be reflected if they strike on the mirror at small angles ("grazing incidence"). Such reflections are particularly efficient for mirrors composed of metals with a high density, such as gold, platinum or iridium. Since astrophysical X-ray sources are weak, maximizing the light-gathering power of a mirror system is critical. Focusing mirrors based on grazing incidence optics, combined with high resolution detectors, are behind the great success of missions like *Chandra*, *XMM-Newton* or NuSTAR. For these three missions, a Wolter optics designe is employed, which improves the instrument angular resolution (in contrast to lobster-eye optics, which provide a wide field of view, see e.g. the recently launched Einstein Probe mission (Yuan et al. 2015)).

Wolter optics make use of a paraboloid followed by a hyperboloid surface mirror to focus X-rays (Wolter 1952). In X-ray astronomy, the Type I design (see Fig. 3.2) is the most commonly implemented, as it implies a relatively simple mechanical configuration and the possibility of nesting telescopes inside one another, which increases greatly the effective reflecting area. Both *Chandra*, *XMM-Newton* and *NuSTAR*, from which X-ray data has been retrieved and analysed in this PhD Thesis, adopted the Wolter Type I optics design. These missions still present some performance differences, however, mainly due to their detector capabilities. In the soft X-ray energy range, *Chandra* features

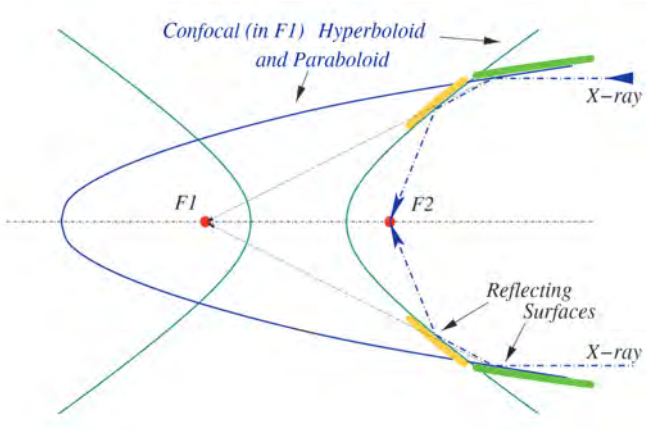

Figure 3.2: Scheme of the Wolter I type optics. Figure form Burrows 2021

an unequaled angular resolution, key to resolve small scale structures with great detail. *XMM-Newton*, with three different cameras onboard, provides a great sensitivity to study faint sources. *NuSTAR*, on the other hand, provides the exciting opportunity to explore the hard X-ray energy range, up to 80 keV, with a much improved angular resolution and sensitivity compared to previous missions operating at these energies. Fig. 3.7 shows the comparison of the effective area dependency on energy for the three instruments.

3.2 THE *chandra* X-RAY OBSERVATORY

The Chandra X-Ray Observatory (CXO) was launched by the NASA's Space Shuttle *Columbia* on 23rd of July, 1999, and its was placed later in a highly elliptical orbit. A High Resolution Mirror Assembly (HRMA), consisting of four nested Wolter Type-I mirrors coated in iridium, is the principle element of the *Chandra* X-ray telescope system. HRMA can yield a point spread function (PSF) as small as 0.5 arcsec. Two instruments are placed on the focal plane of *Chandra*: the Advanced CCD Imaging Spectrometer (ACIS) and the High Resolution Camera (HRC). These two instruments can also be used with grating arrays to get an extremely high resolution X-ray spectrum for bright sources. In this Thesis, all *Chandra* data was obtained using ACIS without grating arrays.

ACIS features two different arrays of CCDs: ACIS-I and ACIS-S (see Fig. 3.3). ACIS-I consists of 2×2 front illuminated chips and is optimized to provide a relatively wide field of view ($16' \times 16'$). ACIS-S, on the other hand, is composed of a 6-strips CCD array among which 4 (S0, S2, S4, S5) are front illuminated and two (S1 and S3) are back illuminated. ACIS-S is usually chosen for on-axis imaging over small fields ($8' \times 8'$). The spatial resolution for on-axis imaging with HRMA/ACIS is limited by the physical size of the CCD pixels ($\sim$

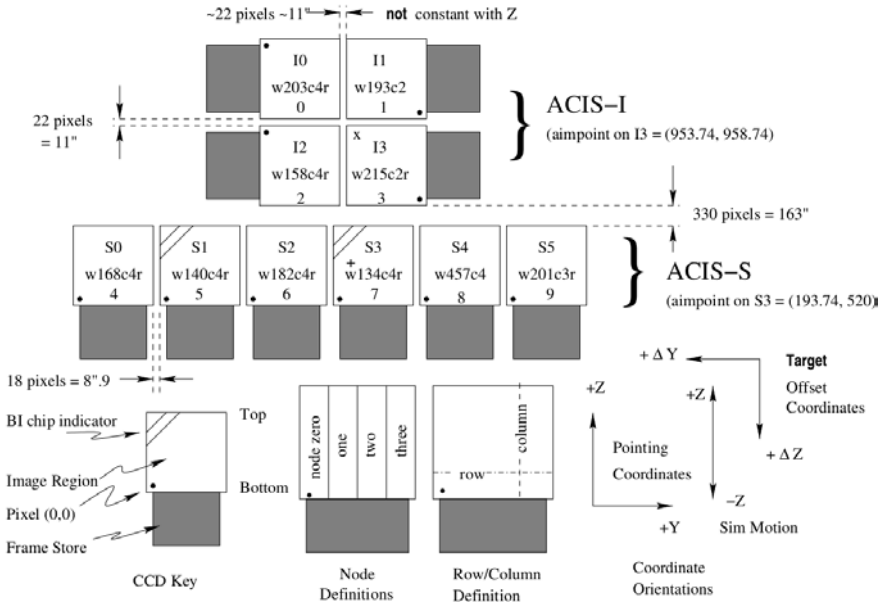

Figure 3.3: Sketch of the *Chandra* ACIS-I and ACIS-S chips layout. Figure adapted from The Chandra Proposer Observatory Guide.

0.492 arcsec) and not by the HRMA. The on-axis PSF of the HRMA is shown on the left panel of Fig 3.4, whilst that of HRMA/ACIS-I is shown on the right panel.

All *Chandra* data used in this Thesis are from observations taken in the so-called timed exposure (TE) mode. In this ACIS operating mode, a CCD collects data for a preselected amount of time (the Frame Time) then the charge from the active region is quickly transferred to the frame store region and subsequently read out. Two telemetry options: FAINT and VFAINT format were used in the data used in this work. The FAINT format provides the event position in detector coordinates, the arrival times, the event amplitude, and the amplitude of the signal in each pixel in the 3×3 event island that determines the event grade. The VFAINT format provides the event position in detector coordinates, the event amplitude, arrival time, and the amplitude of the signal in each pixel in a 5×5 island (although events are still graded by the contents of the central 3×3 island). This format offers the advantage of reducing the background after ground-processing for sources with low counting rates, avoiding both telemetry saturation and pulse pile-up.

3.3 THE X-RAY MULTI-MIRROR MISSION (*xmm-newton*)

XMM-Newton was launched on December 10^{th}, 1999. It carries three co-aligned X-ray telescopes, each consisting of 58 nested Wolter Type-I mirrors coated in gold. *XMM-Newton* thus has the largest effective area of a focusing X-ray telescope ever (the total mirror geometric effective

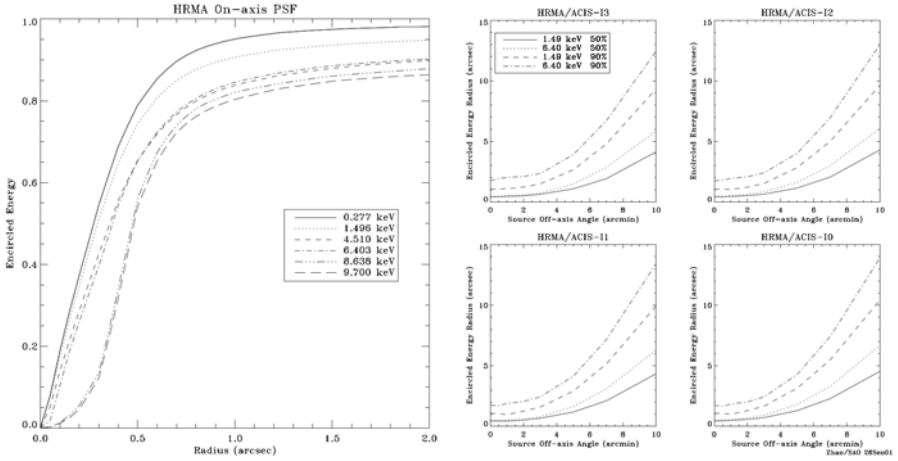

Figure 3.4: **Left**: fractional encircled energy as a function of angular radius, calculated for an on-axis point source, at selected X-ray energies. The curves are the combined response and are centered at the common focus of the full HRMA. **Right**: The HRMA/ACIS-I encircled energy radii for circles enclosing 50% and 90% of the power at 1.49 and 6.40 keV as a function of off-axis angle. Figure adapted from The Chandra Proposer Observatory Guide.)

area is 3×1550 cm^2 at 1.5 keV). On the focal plane, the European Photon Imaging Camera (EPIC) is composed by two MOS (Metal Oxide Semiconductor) CCD arrays (MOS1, MOS2) and one ccd camera (pn) (Turner et al. 2001; Strüder et al. 2001). Highly sensitive imaging observations over the telescope's field of view, of $\sim$30 arcmin, in the energy range from 0.2 to 12 keV provide a good spectral ($E/\Delta E \sim 20-50$) and angular resolution [1]. The relative astrometry between the three EPIC cameras is better than 1–2" across the full field of view.

A sketch of the detector layout and the baffled X-ray telescope field of view for the EPIC MOS and pn cameras is shown in Fig. 3.5. There are 7 CCDs in the focal plane of each MOS camera with the central one located at the focal point surrounded by the outer ones. The 12 pn-CCDs, fabricated on a single wafer so that the detector quality over the entire field of view is approximately uniform, are divided into four individual quadrants with each having three pn-CCD sub-units. MOS and pn cameras have pixels with sizes of 40 and 150 μm corresponding to 1.1" and 4.1" on the sky. MOS1 and MOS2 are rotated by 90^o with respect to one each other. MOS1 encountered however two major hit accidents (probably due to micrometeorite impacts), one on March 9th 2005 and the other on December 11th 2012. CCD6 was significantly damaged during the first event and CCD3 in the second. Data from these two CCDs were thereafter no suitable for its scientific use. The second event has also increased the noise level in CCD4.

1 http://xmm-tools.cosmos.esa.int/external/xmm_user_support/documentation/uhb/

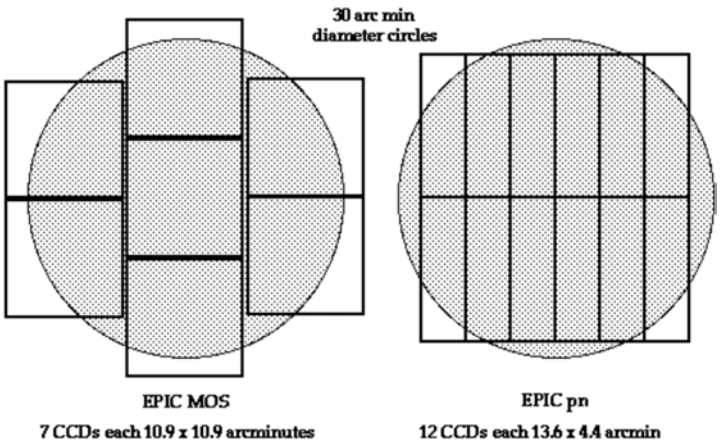

Figure 3.5: A sketch of the field of view of MOS (left) and pn (right) cameras. Each of the two MOS cameras has 7 CCDs with the central one located at the focal point surrounded by the rest outer ones. The outer ones follow approximately the focal plane curvature to improve the imaging for off-axis sources. 12 pn CCDs are divided into four individual quadrants with each having three pn-CCD subunits. Figure from XMM-Newton Users Handbook.

Different from *Chandra*, EPIC's angular resolution is basically determined by the PSF of the mirror modules. The on-axis PSF varies little over a wide energy range (0.1–6 keV) whereas it becomes slightly more energy-dependent above 6 keV. As shown in Fig. 3.6, the shape of the PSF is different for the three cameras. The achieved PSF has a FWHM of about 6" and a HEW, at which 50% of the total energy is encircled, of 15". The fractional encircled energy as a function of angular radius for the three cameras is shown on the right side of Fig. 3.6. All EPIC CCDs operate in photon counting mode with a fixed frame readout frequency, producing event lists. This allows for simultaneous imaging and non-dispersive spectroscopy due to the intrinsic energy resolution of the pixels.

3.4 THE NUCLEAR SPECTROSCOPIC TELESCOPE ARRAY (*nustar*)

The Nuclear Spectroscopic Telescope Array (*NuSTAR*), launched on June 13^{th} 2012, is the first X-ray focusing telescope in orbit operating at energies significantly higher than 10 keV (Harrison et al. 2013). Fig. 3.7 shows *NuSTAR*'s effective area as a function of X-ray energy compared to selected focusing X-ray telescopes. It can be seen that *NuSTAR* can extend the sensitivity into the high-energy end, $\sim$ 10 keV to 79 keV. Compared to collimated or coded mask instruments that operate in a similar energy band, *NuSTAR*'s focusing feature enables a more than 100-fold improvement in sensitivity.

NuSTAR has two almost identical co-aligned telescope modules. These two modules and the equipped detectors are designed to be as

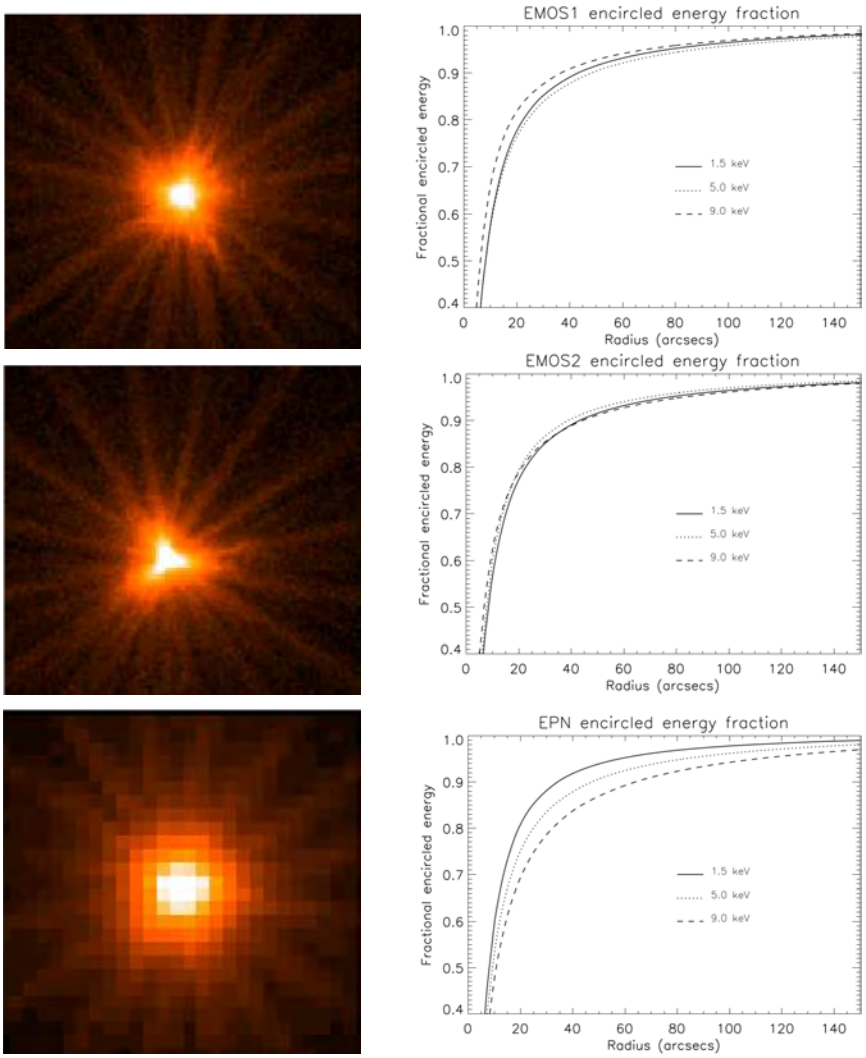

Figure 3.6: **Lefton** panel: from top to bottom is the in orbit on-axis PSF of the MOS1, MOS2 and pn X-ray telescopes, registered on a common source. The pixel size is 1.1 arcsec^2 for the MOS, and 4.1 arcsec^2 for the pn. The images are 110 arcsec wide. **Right** panel: from top to bottom, the fractional encircled energy as a function of angular radius (on-axis) at selected energies of MOS1, MOS2 and pn. Figure adapted from XMM-Newton Users Handbook.

identical as possible so that the focal plane images can be co-added to gain sensitivity. Each consists of 133 concentric mirror shells in a conical approximation to a Wolter Type-I design (Petre and Serlemitsos 1985). In order optimize the broadband energy response and field of view, the inner 89 shells are coated with depth-graded Pt/C multilayers that reflect efficiently below the Pt K-absorption edge at 78.4 keV, while the outer 44 shells are coated with depth-grade W/Si multilayers that reflect efficiently below the W K-absorption edge at 69.5 keV.

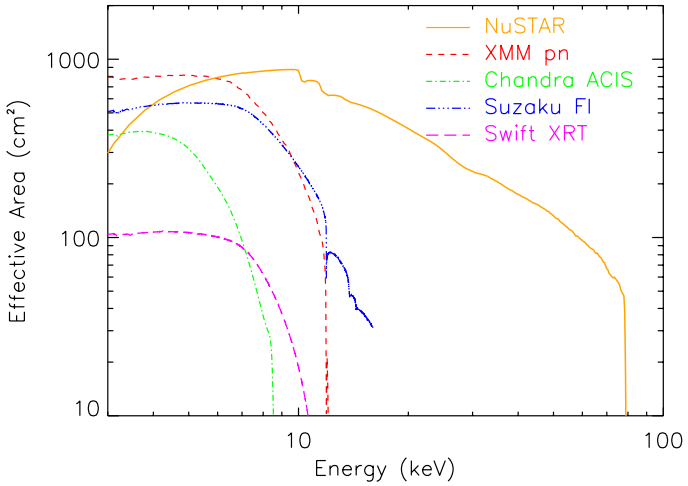

Figure 3.7: Effective collecting area of *NuSTAR* compared to other selected operating focusing telescopes (*Chandra*, *XMM*, *Suzaku*, and *Swift*-XRT). *NuSTAR* provides a good overlap with these soft X-ray observatories and extends the focusing capability up to ∼79 keVs. Figure from Harrison et al. 2013.

The focal plane bench supports two CdZnTe detectors, one for each of the two optics. The optic/detector pairs are known as 'modules'. The detectors consist of four chips, each with 32×32 mm pixels. On-board processors, one for each detector, read out pulse height information from the pixel, as well as from the surrounding 8 pixels for increased positional accuracy. Each event has its location, energy, depth of interaction, and timing recorded with an accuracy of 2 μs. *NuSTAR* detectors do not adopt a CCD-style readout but rather record each event individually. This allows for a readout rate of 300-400 evt/s/module, with a 1% accuracy in the flux measurement. Each detector is surrounded by a CsI anti-coincidence shield and aperture stops that reduce the background generated by stray photons. NuSTAR's focal plane modules are designed to achieve a good energy resolution in the hard X-ray range, with a FWHM response of 400 eV at 10 keV and 0.9 keV at 60 keV.

Two benches that support the optics and focal plane systems, respectively, are separated by a deployable composite mast. The mast is not however perfectly stable. The *NuSTAR*instrument therefore incorporates an aspect/metrology system consisting of a star camera mounted to the optics bench as well as two laser metrology units. When combined, the tracker and lasers measure the translation, tip, tilt and clocking between the benches. This information is used to reconstruct the instantaneous instrument alignment and pointing direction. The resulting corrections are applied on the ground to correctly back-project individual X-rays onto the sky. The absolute astrometric positions of bright X-ray sources with known positions were observed to be within

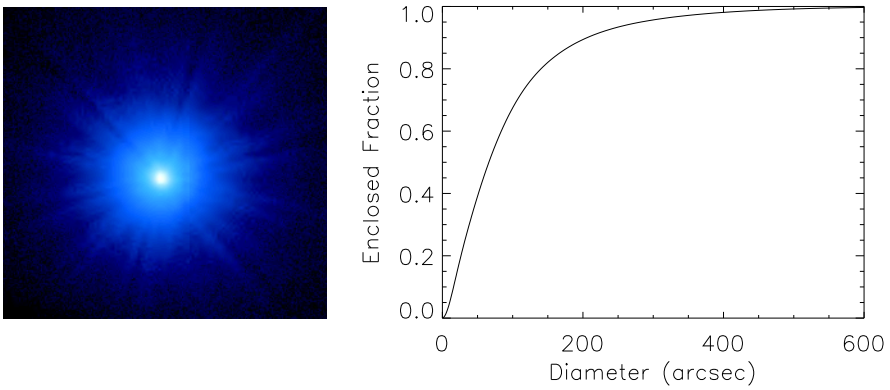

Figure 3.8: *NuSTAR* module A on-axis PSF. Data from observations of the bright point source GRS 1915+105. The left panel shows that the instrument response is azimuthally symmetric. The right panel shows the encircled energy as a function of the diameter of a circular extraction region. The bottom panel. Figure adapted from Harrison et al. 2013.

$\pm$8" (90%) using the updated in-orbit alignment data. The angular resolution of the *NuSTAR*is limited by the optics, displaying a 18" FWHM, with a HPD of 58", over its 3-79 keV energy range. On the other hand, the *NuSTAR* PSF is not a strong function of off-axis angle. While the detailed shape changes, to first order the area of the encircled energy contours remains approximately constant with off-axis angle.

3.5 X-RAY DATA ANALYSIS SOFTWARE

CIAO (Chandra Interactive Analysis of Observations) (Fruscione et al. 2006) is the software package developed at the Chandra X-Ray Center (CXC) for analysing data from the CXO. Apart from a few Chandra-specific instrument tools, CIAO is mission independent by design and has proven itself useful for the analysis of data from other X-ray and non-X-ray missions. CIAO was used in this Thesis to reduce and analyze the data from *Chandra*.

To reduce and analyze data I retrieved from the archive of *XMM-Newton*, the Science Analysis System (SAS) is used as SAS is a collection of tasks, scripts and libraries, specifically designed for *XMM-Newton*.

Finally, for *NuSTAR*data analysis, were employed. The current version of HEASoft contains the *NuSTAR*subpackage of tasks - NuSTARDAS, a subpackge included in HEASoft, maintained at the HEASARC, has been used in this Thesis. HEASoft also contains the FTOOLS and XANADU software packages. Using NuSTARDAS together with the existing FTOOLS and XANADU tasks, we are able to perform a complete analysis of *NuSTAR*datasets.

4

JET-LIKE STRUCTURES FROM PSR J1135-6055

4.1 INTRODUCTION TO PSR J1135-6055

PSR J1135-6055 was discovered with the *Fermi*-LAT in a blind search as an energetic gamma-ray only pulsar (de Luca et al. 2011). It is a young ($\tau \sim 10^4$ yr) and energetic pulsar ($\dot{E} \gtrsim 10^{36}$ erg s^{-1}) located at $d \sim 2.8$ kpc and displaying a high proper motion velocity $v_\perp \lesssim$ 330 km s^{-1} (Kargaltsev et al. 2017). The analysis of archival *Chandra* data amounting to $\sim$ 37 ks obtained from the observation of the SNR G293.8+0.6, covering also PSR J1135-6055, revealed for the first time the presence of both the pulsar and its nebula in the X-ray band (Marelli 2012) whereas SNR G293.8+0.6, likely associated with PSR J1135-6055, was not detected. The morphological properties of the extended emission around PSR J1135-6055 obtained with this *Chandra* observation unveiled two prominent large-scale jet-like structures at both sides of the pulsar.

Here, an updated analysis of archival *Chandra* observations of PSR J1135-6055, amounting to a total of about $\sim$ 130 ks, is presented. We focus on the morphological and spectral properties of this BSPWN to constrain the nature of its jet-like outflows. We compare our results with those reported from other BSPWNe, finding strong similarities with the PWNe around PSR J1509–5850 and Geminga. Our results are interpreted in the general framework of pulsar jet formation theory and in alternative scenarios accounting for the production of jet-like features from BSPWN.

4.2 OBSERVATIONS AND DATA REDUCTION

Chandra observed the field-of-view covering PSR J1135-6055 in three occasions. The first observation (DS-1) was aimed at the study of the nearby SNR G293.8+0.6, yet revealed the presence of PSR J1135-6055 and its PWN in X-rays for the first time. Further two observations with *Chandra* (DS-2 and DS-3) were focused on the PWN itself, for a total of $\sim$ 90 ks. A summary of the *Chandra* observations of PSR J1135-6055 is given in Table 4.1

The three observations were all performed in *Chandra*'s `VERY FAINT`, TE mode using the instrument's ACIS-S detector (see Section 3.2). Data processing was performed using CIAO (Fruscione et al. 2006), version 4.11, together with the *Chandra*'s Calibration Database (CALDB), version 4.8.2. All observations were reprocessed using `chandra_repro` in `VFAINT` background cleaning mode. Unless otherwise noted, we

Data set	Obs. ID	Date	Exposure (ks)
1	3924	2003-08-24	36.11
2	15966	2014-12-30	55.54
3	17572	2015-01-03	35.73

Table 4.1: *Chandra* observations covering PSR J1135-6055 used for the analysis reported in this Thesis. Data set 1 (DS-1) aimed for the study of SNR G293.8+0.6. DS-2 and DS-3 correspond to the two subsequent dedicated *Chandra* observations of PSR J1135-6055. Columns indicate archival Observation ID, data taking dates, and total observation exposure time.

consider only events on the S3 (ccd_id=7) chip and restrict the energy range to 0.5 – 7.0 keV.

We used the `fluximage` CIAO tool to generate broadband exposure-corrected flux maps for each of the three data sets. We then employed the Voronoi Tessellation and Percolation source detection tool `vtpdetect` on the reprocessed level=2 event file using the previously generated exposure maps, as this method is optimized for the detection of low surface-brightness extended sources (Ebeling and Wiedenmann 1993). The generated source lists were used to remove sources in the FoV. We also checked for the presence of X-ray flares by extracting and filtering the background light-curve (in temporal bins of 200 s width) for deviations larger than 3 sigma. The effective final exposures obtained for each observation are 32.36 ks, 55.14 ks, and 35.73ks for DS-1, DS-2 and DS-3, respectively, and summing up for a total of 127.38 ks (see Table 4.1).

We merged the three data sets to perform a morphological analysis of PSR J1135-6055 and its surroundings. We employed the WCS reference system of DS-2 since it is the longest of the two dedicated pointings on the source assuming that between these two pointings there is no significant difference in the astrometry. To merge the DS-1 data set, we applied the `wavdetect` tool to detect point sources in both DS-1 and DS-2. The two output source lists were then cross-matched to re-project the aspect solution file of DS-1 using `reproject_aspect`. Finally, by running the CIAO tools `wcs_match` and `wcs_update` we ensured a common WCS reference system for the three data-sets.

Merging was performed using the CIAO routine `merge_obs`, with bin size set to 1, in the broad-band energy range 0.5–7.0 keV. A map of the retrieved raw counts was then divided by the corresponding exposure map and then normalised with the exposure time to produce the final flux map (see Fig. 4.1).

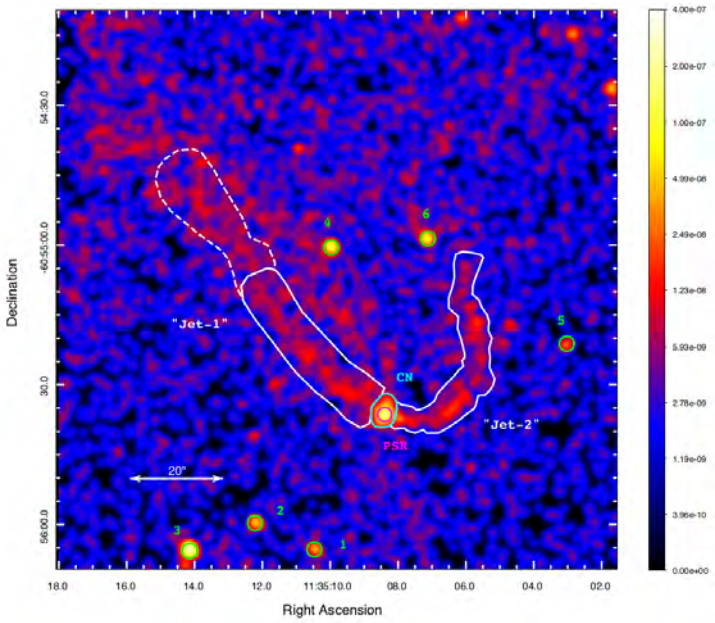

Figure 4.1: Exposure-corrected flux map of the extended emission around PSR J1135-6055 for energies in the range 0.5 – 7.0 keV, smoothed with a 1.5" Gaussian kernel. The following regions are shown: Jet-1 inner (white eastern polygon) and outer regions (dashed white eastern polygon), Jet-2 (white western polygon), CN (cyan polygon), and PSR J1135-6055 (magenta circle with a radius of 1.5"). Additionally, six point sources in the FoV are marked with green circles.

4.3 CHANDRA ANALYSIS RESULTS

4.3.1 *Imaging results*

From the final flux map produced as explained in Sect. 4.2, in addition to the PWN itself, two asymmetric jet-like structures can be clearly distinguished. The eastern jet-like feature, Jet-1, appears more diffuse and displays a much more rectilinear structure compared to the western jet (Jet-2), which displays instead an "arc" shape, likely related to the pressure exerted on the outflow by the surrounding medium.

In the FoV within 1 arcmin around the pulsar, there are also six point-like X-ray detected background sources, marked with a green circle in Fig. 4.1. Five of these are present in the *Chandra* Source Catalogue (S1: 2CXO J113510.4 − 605605, S2: 2CXO J113512.2-605559, S3: 2CXO J113514.1-605605, S4: 2CXO J113509.9-605500, and S5: 2CXO J113503.0-605521). The sixth point-like source (S6) is unassociated, and shows significant flux variability between DS-1, DS-2 and DS-3. Further studies are needed to constrain its nature and/or any possible association at other wavelengths.

Surface brightness profiles were extracted for both Jet-1 and Jet-2. Whereas the eastern jet displays a rather smooth flux profile, the west-

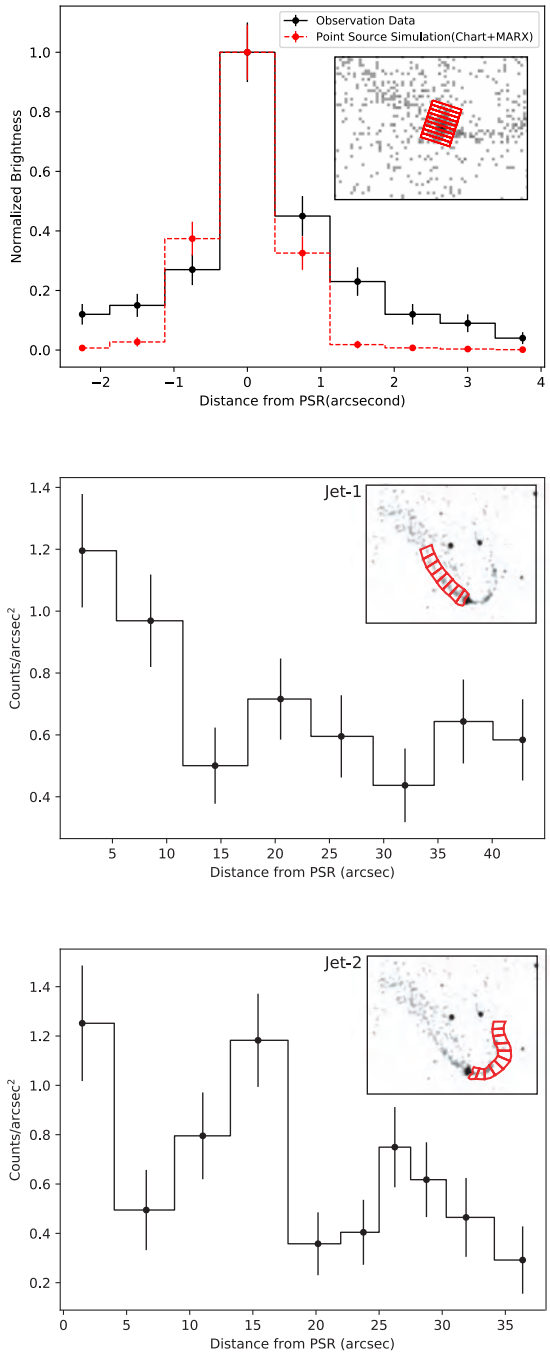

Figure 4.2: Surface brightness profiles along the compact nebula around PSR J1135–6055 (top panel) and the eastern (Jet-1, middle panel) and western (Jet-2, bottom panel) jet-like structures. The profile of the simulated Chandra PSF for a point-like source with spectral properties as the ones derived for PSR 1135–6055 and normalized to its peak intensity at the location of the pulsar is also displayed in the top panel.

ern feature displays a moderately significant enhancement about 18″ away from PSR J1135-6055, followed by a flux decrease and recovering afterwards to a relatively smooth profile (see Fig. 4.2). These profiles further highlight the asymmetry of the two jet-like structures. A flux profile was also extracted for PSR J1135-6055 and its close nebula using 8 rectangular slices along the south-east to north-west direction (see top panel in Fig. 4.2). The PWN displays extended emission along this axis, with a moderately broad flux profile which significantly extends beyond the *Chandra*'s point spread function (PSF). This extended emission is interpreted as the nebula powered by the central pulsar (and labeled in the following as the "compact nebula", CN).

PSR J1135-6055 lacks an accurate estimate of its proper motion velocity. An upper limit $v_{\mathrm{J1135},\perp} \leq 330$ km s^{-1} is provided in Kargaltsev et al. (2017). We take advantage of the time span of the *Chandra* observations studied here to constrain PSR J1135-6055's velocity. Following the procedures outlined in Sect. 4.2, we used `wavdetect` and `wcs_match` to retrieve and then match the position of PSR J1135-6055 amongst data sets, taking DS-2 as a reference since it accounts for the longest available exposure. PSR J1135-6055 is found at (RA, Dec) = ($11^{\mathrm{h}}35^{\mathrm{m}}08.38^{\mathrm{s}} \pm 0.02^{\mathrm{s}}$, $-60°55'36''.49 \pm 0.14''$) in DS-1 and at (RA, Dec) = ($11^{\mathrm{h}}35^{\mathrm{m}}08.41^{\mathrm{s}} \pm 0.01^{\mathrm{s}}$, $-60°55'36''.29 \pm 0.12''$) in DS-3. In this procedure, we are able to constrain the shift in RA and DEC between DS-1 and DS3, $(\Delta\mathrm{RA}, \Delta\mathrm{Dec})^{\mathrm{J1135}}_{DS1,DS3} = (0.035^{\mathrm{s}} \pm 0.021^{\mathrm{s}}, 0.20'' \pm 0.19'')$ Considering the time span of $\sim$ 11.4 yrs between DS-1 and DS-3 and applying astrometric corrections, this translates into a shift of $\mu_{\mathrm{J1135}} \approx 0.043 \pm 0.028$ arcsec yr^{-1}. In order to account for systematic effects, we apply the same procedure with the catalogued sources S3 and S5, which we take as reference sources since these are detected at a statistical significance above 5σ in our analysis. A weighted mean angular shift for these two sources is computed between DS-1 and DS-3, weighted with the square of their positional uncertainties, which is found to be $(\Delta\mathrm{RA}, \Delta\mathrm{Dec})^{S3,S5}_{DS1,DS3} = (0.009^{\mathrm{s}} \pm 0.023^{\mathrm{s}}, 0.463 \pm 0.186'')$. This translates into a shift, after applying astrometric corrections, of $\mu_{S3,S5} \approx 0.042 \pm 0.031$ arcsec yr^{-1}. Since μ_{J1135} is within errors at the level of $\mu_{S3,S5}$, which we take as a systematic uncertainty in our measurement, we use this latter value to derive an upper limit to PSR J1135-6055's velocity. Taking a distance $d_{\mathrm{J1135}} = 2.9$ kpc (Marelli 2012), this translates into $v_{\mathrm{J1135},\perp} \leq 282$ km s^{-1}.

4.3.2 *Spectral results*

Spectral fits were extracted for both the PSR and Jet-1 and Jet-2 regions. Jet-1 was further subdivided into an inner and an outer regions in order to look for spectral variations, e.g. due to radiation losses. The low-counts retrieved for the CN prevents from a meaningful spectral fit to this component. We note that some counts from the CN region

may have been ascribed to the PSR region given their overlapping spatial distribution. However, given the relative low-counts from the CN region as compared to the PSR one, the effects on the final spectral results on the latter are negligible.

Simple power-law spectral models were employed in all cases. For the pulsar, adding a black-body component worsened the fits results significantly. The best fit parameters for the PSR component are a spectral index $\Gamma_{\rm PSR} = 1.31 \pm 0.29$, a flux normalisation $N_{0,PSR} = (3.15 \pm 1.12) \times 10^{-6}$ ph s^{-1} cm^{-2} and a column density of $N_{\rm H} = 0.51 \pm 0.19 \times 10^{22}$ cm^{-2}. For the spectral analysis of all Jet-1 and Jet-2 regions, column densities were fixed to the value obtained in the spectral fit of the pulsar. Spectral indices for Jet-1 are found to be $\Gamma_{Jet1} = 1.71 \pm 0.08$ (with $\Gamma_{Jet1}^{inner} = 1.70 \pm 0.11$ and $\Gamma_{Jet1}^{outer} = 1.71 \pm 0.12$), and $\Gamma_{Jet2} = 1.88 \pm 0.12$ for Jet-2. A summary of the spectral fits is reported in Table 4.2. These values are in agreement, within uncertainties, with the values reported in Marelli (2012) for a similar analysis of PSR J1135-6055 but accounting only for *Chandra* observations in 2003 (DS-1 in Table 4.1) .

Table 4.2: Spectral analysis results of jet-1, jet-2 and PSR regions. `cstat` statistics are used. $N_{\rm H}$ values are fixed to the value found in the spectral fit of the PSR. Errors indicate the 1σ statistical level uncertainty.

	Γ	N_0 ($\times 10^{-6}$ ph s^{-1} cm^{-2})	$N_{\rm H}$ ($\times 10^{22}$ cm^{-2})	χ^2/d.o.f
PSR	1.31 $\pm$ 0.29	3.15 $\pm$ 1.12	0.51 $\pm$ 0.19	349/443 = 0.79
Jet-1	1.71 $\pm$0.08	15.06 $\pm$1.03	0.51 $\pm$0.19	496/444 = 1.12
Jet-1 inner	1.70 $\pm$0.11	8.10 $\pm$0.77	0.51 $\pm$0.19	411/444 = 0.93
Jet-1 outer	1.71 $\pm$0.12	6.93 $\pm$0.71	0.51 $\pm$0.19	399/444 = 0.90
Jet-2	1.88 $\pm$0.12	8.02 $\pm$0.78	0.51 $\pm$0.19	440/444 = 0.99

4.4 DISCUSSION ON PWN J1135-6055

The analysis of *Chandra* observations on PSR J1135-6055 reported in Sect. 4.2 reveals, in addition to the bright emission from PSR J1135-6055, the presence of several extended features likely connected to it, e.g. by the shocked wind of the pulsar moving at supersonic speeds through the surrounding medium (Gaensler and Slane 2006; Bykov et al. 2017). A compact nebula is found extending beyond the *Chandra*'s PSF both ahead and behind the PSR location, whereas two lateral jet-like structures displaying a highly asymmetric geometry are also clearly distinguished. Similar large X-ray extended features have been observed in a few other PWNe (Kargaltsev et al. 2017). The morphology of PSR J1135-6055 is, in particular, reminiscent of that observed in runaway pulsars PSR J1509-5850 (Klingler et al. 2016a) and Geminga

(Posselt et al. 2017), both of which display an axial tail and two lateral outflows. The extensions of the tail and jet-like features are, respectively: 0.04 pc and $\sim$ 0.5-0.7 pc in PSR J1135-6055 (or 2.8″ and 0.5-1′ at a distance of $d_{\rm J1135} = 2.9$ kpc); 0.05 pc and 0.13–0.18 pc in PSR J1509–5850 (or 2.7″ and 7–10″ at a distance $d_{\rm J1509} = 2.9$ kpc); 0.07 pc and $\sim$ 0.3 pc in Geminga (or 1.2′ and 5′ assuming $d_{\rm Geminga} = 0.25$ kpc)

The origin of the extended emission in front of PSR J1135-6055, and the two lateral outflows is uncertain. We tentatively interpret the extended emission ahead of PSR J1135-6055 as the region encompassed by the bow shock in a BSPWN. Its extension, of about 2 arcsec or $\sim 8.7 \times 10^{16}$ cm at a distance $d_{\rm J1135} = 2.9$ kpc, should be of the order of the stand-off radius $R_{\rm S}$ and can be used to infer the proper motion velocity of the system: $v_{\rm psr} \approx (\dot{E}_{PW}\,(1/4\,\pi\,c\,\rho_{\rm ISM} R_{\rm S}^2)^{1/2} \sim 210$ km s^{-1}, taking $\dot{E}_{PW} = 2.1 \times 10^{36}$ erg s^{-1} and an ISM particle density of $n_{\rm ISM} = 1$ cm^{-3}. This estimate is in accordance with the value obtained in Sect. 4.3, $v_{\rm psr} \leq 282$ km s^{-1}. We have assumed here that the entire spin-down power of PSR J1135-6055 is carried away by the pulsar wind, which is in turn taken to be isotropic for simplicity . The value of $v_{\rm psr}$ depends on these parameters weakly, and its value can change within factors of $\sim$ a few.

The physical origin of the CN emission around the PSR would correspond in this scenario to the pulsar equatorial outflow shocked by the ISM ram pressure either ahead or trailing he pulsar proper motion. As for the lateral outflows, they would correspond to bipolar jets, again bent by the external pressure of the medium. The asymmetry observed between the eastern/western outflows could be due to their different direction of propagation with respect to the pulsar proper motion, to a different relative kinetic power injected into each outflow, or to different properties of the ISM through which they propagate. Similar scenarios have been proposed for the Geminga PWN (Pavlov et al. 2006). This interpretation is also in accordance with recent numerical simulations of extended outflows originated in fast-moving PWNe (Barkov et al. 2019b).

The behaviour obtained for PSR J1135-6055's outflows resembles instead the ones found in PSR J1509-5850, displaying an index $\sim$ 1.8 and 1.9. Both Geminga and PSR J1509-5850 display also an axial tail trailing the pulsar, with spectral indices $\Gamma \gtrsim 2.0$ and 1.4, respectively. Unfortunately, the low statistics obtained in this report for the CN region around PSR J1135-6055 prevents any further comparison of the tail spectral properties.

In this scenario, the observed X-ray emission would be produced by high-energy electrons embedded in the jets' magnetic field $B_{\rm jet}$. The absence of any significant spectral break due to synchrotron cooling along the jets (particularly for the inner and outer regions of Jet-1) implies that $\tau_{sync} \approx 100\,(E_{\rm ph}/1\,keV)^{1/2}\,(B_{\rm jet}/50\,\mu{\rm G})^{3/2} \geq \tau_{dyn} \sim l_{\rm jet}/v_{\rm jet}$, where $l_{\rm jet}$ and $v_{\rm jet}$ are the jet length and flow velocity, respectively. A

lower limit on the bulk velocity of the jet outflows can thus be placed, $v_{\rm jet} \gtrsim 8000\,{\rm km\ s^{-1}}$. The fact that electrons are confined within the jet, on the other hand, implies that their gyroradius $r_{\rm gyro} = \gamma_{\rm e}\, m_{\rm e} c^2 / e B_{\rm jet}$ cannot exceed the jet radius, $R_{\rm jet}$. For a given magnetic field $B_{\rm jet}$, this condition can be used to derive a maximum Lorentz factor of the emitting electrons along the jet, $\gamma_{\rm e}^{max}$. A minimum value, $\gamma_{e,min}^{\rm X}$, is on the contrary needed for synchrotron emission to reach the keV band for the same value of $B_{\rm jet}$. Putting these limits together, one obtains $6.3 \times 10^7 (B/50\,\mu{\rm G})^{-1/2} \leq \gamma_{\rm e}^{\rm X} \leq 3.7 \times 10^9 (B/50\,\mu{\rm G})$.

An alternative interpretation for the CN in PSR J1135-6055 and the two lateral outflows may also be envisaged. The latter could represent the projection of a limb-brightened shell formed in the region of the contact discontinuity separating the pulsar shocked wind with the shocked ISM material. The CN around the PSR could correspond in this scenario to a pulsar jet launched along the pulsar's spin axis. Given the moderately high speed of PSR J1135-6055, such a forward jet would propagate ahead rather shortly, braked and eventually deflected by the strong pressure exerted by the ISM, whereas it should instead be able to propagate up to longer distances behind the PSR. In this regard, it is worth noting that the extended emission observed from the long, eastern outflow Jet-1 is relatively wider than the western jet-like outflow, and quite non-homogeneous (see Fig. 4.1). In particular, a few arcsec away from the position of the pulsar, the Jet-1 seems to be divided in two broad quasi-rectilinear structures, separated by a region displaying a comparatively lower surface brightness.

At larger distances, these structures smoothly converge again into a diffuse, wider structure. While the Jet-1 inner and outer regions may still not represent a proper jet but the limb-brightened shell of the PWN, the inner outflow could be attributed to emission produced by a backwards-propagating jet, slightly deflected/bent by the external medium pressure, which at large distances approaches the PWN shell eastern limb. Note however that a similar structure may also be produced by a ram-pressure confined PWN tail. In that case, however, a bending may not be expected, as the tail should propagate along the direction of motion, confined by an almost symmetrical lateral pressure. Deeper observations of the PWN around PSR J1135-6055 are in any case needed to conclusively assess whether this eastern outflow is indeed composed by several extended sub-structures (see, e.g. the multiple outflows scenario discussed in Pavan et al. 2016 for the Lighthouse Nebula).

The spectral and morphological properties of the extended structures discussed above cannot exclude alternative scenarios for the production of the jet-like structures observed in PSR J1135-6055. Assuming that the lateral outflows correspond to true pulsar jets, a significant bending may be expected and is indeed clearly observed in our morphological analysis, particularly for the western outflow. This

is contrary to more extreme jet-like features seen in other BSPWN (e.g. in the Guitar Nebula (Hui et al. 2012) and the Lighthouse Nebula (Pavan et al. 2014), in which the length and orientation of these features favours a scenario based on the diffusion of high-energy escaping electrons (or "kinetic jets" Barkov et al. 2019b) from the BSPWN. On spectral grounds, our analysis could not retrieve any softening along the jet-like features which could constrain the energy distribution of the underlying emitting particle population (see e.g. Bandiera 2008). Further observations of PSR J1135-6055, both in X-rays or at lower wavelengths (e.g. in the radio band) may be able to resolve such a spectral fingerprint.

5

PARTICLE ESCAPE FROM PWN B1853+01

5.1 INTRODUCTION TO PWN B1853+01 AND THE W44 SNR

W44 (G34.7-0.4) is a mixed-morphology SNR that is interacting with nearby molecular clouds (Wootten 1977; Seta et al. 2004). The age of W44 is about $\sim 10^4$ yrs Smith et al., whereas its distance is found to be $\sim$3.0 kpc, obtained through dedicated OH and HI absorption measurements of the SNR (Caswell et al. 1975; Claussen et al. 1997; Ranasinghe and Leahy 2018). At radio wavelengths, W44 presents a distorted elliptical shell-like shape of about $25' \times 35'$ with the bulk of the radio emission concentrated in knots and filamentary structures (Clark et al. 1975; Jones et al. 1993). Inside the radio shell, the remnant is filled with thermal X-ray emission produced by overi-onized recombining plasma (Shelton et al. 2004; Uchida et al. 2012; Okon et al. 2020). This X-ray thermal emission also displays an elongated shape in the NW-SE direction (Watson et al. 1983; Jones et al. 1993; Rho et al. 1994). Fig. 5.1 displays this X-ray thermal component from W44 obtained with the *XMM-Newton* data set analysed in this Thesis, together with the radio contours obtained from the SNRcat (Ferrand and Safi-Harb 2012). In the high-energy gamma-ray band, two extended gamma-ray sources were found at the two opposite edges of its major axis(Uchiyama et al. 2012; Peron et al. 2020). At very-high-energies (VHEs), the MAGIC Cherenkov telescopes have reported only upper limits from the SNR, also focused on the northern part of the remnant (di Tria et al. 2022).

The central pulsar, PSR 1853+01/PSR J1856+0113, was discovered in 1991 (Wolszczan et al. 1991), and is located south of the SNR, well within its radio shell and at the southern edge of the thermal X-ray emission region. The pulsar slows down at a rate $\dot{P} \sim 208 \times 10^{-15}$ s s^{-1}, which leads to a characteristic age of about 20 kyr. Based on the dispersion measure towards the pulsar, a distance to the source has been estimated to be 3.2 kpc (Wolszczan et al. 1991). Further pulsar-related parameters are listed in Table 5.1. The similarities in both age and distance for PSR B1853+01 and SNR W44 strongly suggest an association between them.

An extended nebula around PSR 1853+01 was first revealed by Jones et al. 1993 in the radio band. Soon after, Frail et al. 1996 confirmed the PWN nature of the extended emission in radio, and located the pulsar at the apex of a cometary-shaped radio structure with an extension of about 2.5′ (or about 2 pc at an assumed distance to W44 of 3 kopc). The spectral analysis of these radio data revealed a relatively flat spectral index $\alpha = -0.12 \pm 0.04$ (where $S_\nu = \nu^\alpha$) when compared to

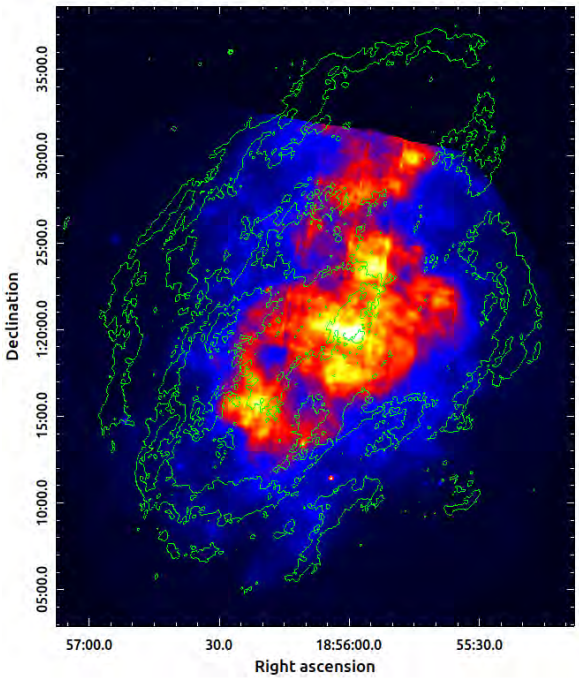

Figure 5.1: *XMM-Newton* exposure corrected mosaic images of W44 in the energy range 0.5–4.0 keV overlaid with the SNR radio contours in green obtained from SNRcat (Ferrand and Safi-Harb 2012)

that obtained for the SNR ($\alpha = -0.33$). The pulsar was also detected at hard X-rays Harrus et al. 1996 using ASCA observations of the region, whereas the cometary-tail extension was also detected in the X-rays with a 50 ks observatin of the source with *Chandra* Petre et al. 2002.

In this Chapter we present a detailed study of PSR B1853+01 and its surrounding nebula in the X-ray band, based on spatially resolved spectra obtained using archival data from *Chandra*, *XMM-Newton* and *NuSTAR*. Below we describe the data set used in this work and data analysis and reduction processes for each mission. We report on the imaging results including images from the three instruments, which highlight a number of features at different scales. Our spectral analysis improved the constraints on the column density towards the source, $N_{\rm H}$, which allow us to further describe the spectral properties of the different extended structures. We finally discuss the obtained results, focusing on the nature of the extended emission structures and comparing our findings to other similar BSPWNe.

5.2 OBSERVATIONS AND DATA REDUCTION

5.2.1 *XMM-Newton Data Analysis*

We retrieved a total of seven archival *XMM-Newton* observations in which PSR 1853+01 and its nebula were found in the instrument's

Table 5.1: Parameters of PSR 1853+01

Parameters	
R.A. (J2000)	$18^h56^m10.89^s \pm 0.01^s$
Decl. (J2000)	$01°13'20.5'' \pm 0.3$ ''
P(s)	$0.26739884073 \pm 0.00000000003$
$\dot{P}(ss^{-1})$	$(208.408 \pm 0.003) \times 10^{-15}$
Derived Parameters	
Magnetic field	7×10^{12} G
Characteristic age	2×10^4 yr
Spin-down luminosity	4.3×10^{35} ergs s^{-1}
Distance	$\sim$ 3.2 kpc

FoV. Our study is based on the analysis of four of these archival observations (namely Obs. ID=0551060101, 0721630101, 0721630201, and 0721630301), as the three remaining pointings accounted for very short exposures which could lead to inaccurate results due to flaring background. Details of the data set used in this Thesis are given in Table 5.2. We note that Obs. 0551060101 accounts for the only on-axis observation available, as for Obs. 0721630101, 0721630201, and 0721630301 neither MOS1 CCD6 nor MOS1 CCD3 were available. The analysis reported in this work has been performed using the *XMM-Newton* Science Analysis System[1] (SAS) version 20.0.0, running on an Ubuntu 20.04 platform. Furthermore, since we're interested in the study of the extended emission encompassing the PWN around PSR B1853+01, we also employed the *XMM-Newton*'s Extended Source Analysis Software (XMM-ESAS) and related analysis procedures [2].

Data was retrieved from the *XMM-Newton* Science Archive, and their reduction made use of the `emchain` and `epchain` tools applied to both MOS and pn observations to filter events based on good time intervals, malfunctioning pixels, and out-of-time events. The task `espfilt` was then applied to filter out cosmic soft-proton events (for pn we used `rangescale=15.0`). For the imaging analysis, we generated the spectra for the entire region, the redistribution matrix files and the ancillary response files using `mos-spectra` and `pn-spectra`, for the MOS and pn detectors, respectively. We estimated the particle-induced non-X-ray background (NXB) with `mos-back` and `pn-back`. The `merge_comp_xmm` tool was then used to merge the individual components (counts, exposure and particle background) from the four observation data sets. We then obtained background subtracted, expo-

1 https://xmm-tools.cosmos.esa.int/external/xmm_user_support/documentation/sas_usg/USG/

2 https://heasarc.gsfc.nasa.gov/docs/xmm/xmmhp_xmmesas.html

sure corrected, and adaptively smoothed images using `adapt_merge`. For the spectral analysis, we first used `especget` to extract spectra for individual pointngs, and then `epicspeccombine` and `grppha` were used to combine and group the spectra.

Table 5.2: *XMM-Newton* Observations.

Obs. ID.	MOS1	MOS2	pn
0551060101	Full Frame 74.7 ks	Full Frame 74.7 ks	Full Frame 70.4 ks
0721630101	Full Frame 112.2 ks	Full Frame 112.1 ks	Extended Full Frame 108.2 ks
0721630201	Full Frame 110.7 ks	Full Frame 110.6 ks	Extended Full Frame 106.7 ks
0721630301	Full Frame 107.2 ks	Full Frame 106.7 ks	Extended Full Frame 102.6 ks

5.2.2 *Chandra Data Analysis*

Three observations (labelled ObsID. 1958, 5548, 6312) containing the PSR B1853+01 and its nebula were found in the *Chandra*'s archive (see Table 5.3 for details). ObsID.1958 was aimed at the center of the SNR W44 with a telescope roll angle of $\sim 285^\circ$ in which the pulsar falls on the S2 chip with an off-axis angle of about 7 arcmin. ObsID. 5548 and 6312 include on-axis observations of the PWN (aimpoint on S3). We reduced the data with the *Chandra* Interactive Analysis of Observations (CIAO) version 4.14.0[3], and the calibration database CALDB (version 4.9.6)[4]. All three observations were reprocessed using `chandra_repro`. For ObsID. 5548 and 6312, "`check_vf_pha = yes`" was set to reduce the ACIS particle background in very faint mode observations.

Broad band (0.5-7.0 keV) flux images accounting for the three observations were produced using `fluximage` (with the parameter psfecf=0.9 to detect faint sources). These flux images were used later by `vtpdetect` to detect and exclude sources and then checked for flares by filtering the background light curve (0.5-7 keV, time bin width of 259.28 s) for deviations larger than 3σ using CIAO's `deflare` tool. We then used these good time intervals to filter the events file, resulting in 44.79 ks left for ObsID. 1958. No significant flares were detected in the other two observations, which account for a total observation time of 52.31 ks and 39.58 ks for Obs. 5548 and Obs. 6312, respectively. The

3 https://cxc.cfa.harvard.edu/ciao/
4 https://cxc.cfa.harvard.edu/caldb/

total exposure for the three observations is therefore $\sim$ 136.86 ks (see Table 5.3).

We applied astrometric corrections to the data sets using the longest observation, ObsID. 5548, as a reference. We used `fluximage` (with parameter psfecf=0.393 to have bright point-like sources detected) to generate broad-band flux images that were later used by `wavdetect` to obtain source lists of each observation. After cross-matching the resulting lists obtained for ObsID. 1958 and ObsID. 5548 and then between ObsID. 5548 and ObsID. 6312 with `wcs_match`, we corrected for the aspect solution of ObsID. 1958 and ObsID. 6312 with `wcs_update`. Considering this absolute astrometry correction, then `merg_obs` was used to merge observations to the same tangent point. To study the pulsar, we also simulated the point spread function (PSF) using *Chandra* Ray Trace (ChaRT) v2 and MARX version 5.5.2. For spectral analysis, `specextract` was used to extract spectra from individual observations, and `grppha` was subsequently used for grouping them.

Obs. ID	Chip	Data Mode	Exposure(ks)	Observation Date
1958	S2	FAINT	45.56 ks	2000-10-31
5548	S3	VFAINT	52.31 ks	2005-06-25
6312	S3	VFAINT	39.58 ks	2005-06-23
Total Exposure			137.45 ks	

Table 5.3: *Chandra* observations containing PSR B1853+01

5.2.3 *NuSTAR Data Analysis*

PSR 1853+01 and its PWN region were observed by *NuSTAR* on Sepetember 2nd 2018 (ObsID. 40401005002) for a total of about 105 ks. The *NuSTAR* data was reduced using the package NuSTARDAS (version 2.1.1) together with the *NuSTAR* FPM CALDB (version 20220105). The `nupipeline` tool was used to reprocess the data to produce cleaned and calibrated event list files. For imaging analysis, we first selected photon events in different energy bands using the CIAO tool `dmcopy` and used `nuexpomap` to produce exposure maps for each energy band and then summed up *NuSTAR* raw images in each energy band to create the final mosaic images using XIMAGE (HEAsoft 6.29). We noticed that the PWN emission is dominant up to $\sim$ 20 keV; therefore, below we only present the imaging analysis below 20 keV. Photon events were selected in three energy bands: 3-10 keV, 10.0-20.0 keV and 20.0-79.0 keV. These energy ranges were selected to ensure a sufficient photon statistics in each image, as well as to minimize the effects of averaging the energy-dependent vignetting function over the entire energy range. Prior to spectral fitting, we used `nuproducts` to generate

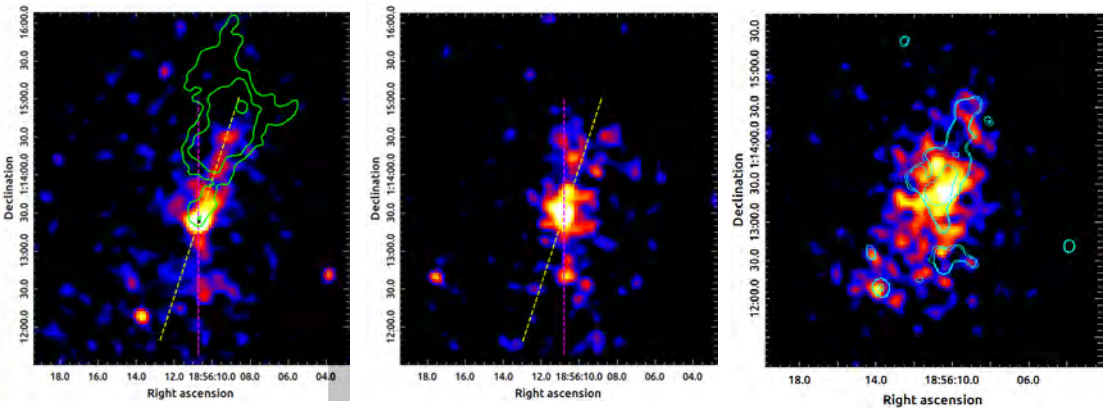

Figure 5.2: Images of PSR B1853+01 and its surrounding emission. **Left**: The exposure-corrected merged *Chandra* ACIS image in 4-8 keV energy band overlaid with the PWN radio contours in green taken from SNRcat Ferrand and Safi-Harb 2012. The image is binned by a factor of 5 (pixel size 2.46") and smoothed with a Gaussian function with radius r=3 pixel and sigma σ=1.5 pixels. **Center**: Merged (MOS1+MOS2) mosaic on-axis *XMM-Newton* count image in 4-8 keV energy band. The image is smoothed with a Gaussian function with radius r=3 pixel and sigma σ=1.5 pixels while the pixel size is set to be 2.5"arcsec. **Right**: Merged (FPMA+FPMB) mosaic *NuSTAR* image in 4.0-10.0 keV, overlaid on which an contour map extracted from *Chandra* image on the left panel. The dashed yellow line shows the approximate symmetry axis of the PWN tail, which can be crudely identified with the direction of the pulsar's proper motion. The dashed magenta line is in N-S direction which roughly coincide with the direction of the southern outflow just leaving the PWN bow shock.

NuSTAR's response matrix (RMF) and effective area ARF) files for an extended source.

5.3 X-RAY DATA ANALYSIS RESULTS

While the PWN is too faint in the soft X-ray band, it can be discerned from the SNR thermal emission above ∼2.0 keV and becomes dominant at energies above ∼4 keV. We therefore limited the analysis of the PWN to relatively high energies in order to remove the contamination from the SNR thermal emission (a similar strategy was adopted in Harrus et al. 1996 and Petre et al. 2002). For the analysis of the *Chandra* data, the excellent angular resolution of the instrument allowed us to clearly separate the pulsar emission from that coming from the PWN, and to resolve out a number of structures at the smallest scales (with angular sizes ranging from a few to a few $\times$10 of arcsec). In the case of *XMM-Newton*, although it is difficult to obtain spatially resolved spectral results as good as those attainable with *Chandra*, the instrument features a very good sensitivity and relatively large

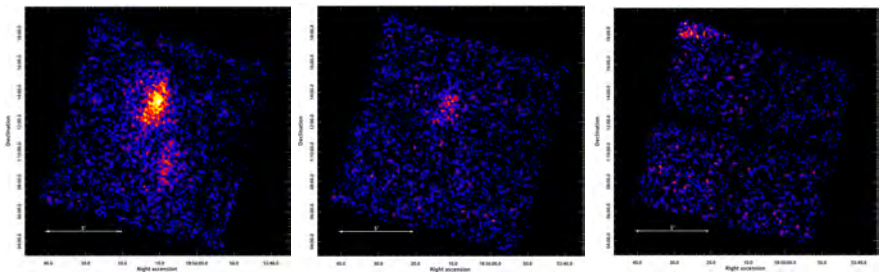

Figure 5.3: Merged (FPMA+FPMB) mosaic*NuSTAR* images in different energy band. **Left**: 4.0-10.0 keV. **Middle**: 10.0-20.0 keV **Right**: 20.0-79.0 keV. The PSR/PWN emission is clearly seen up to $\sim$ 20 keV.

FoV, and was therefore mainly used to study large scale structures displaying a relatively low surface brightness. The analysis of the *NuSTAR* data set, instead, allowed for the first time to constrain the X-ray properties of the PWN and surrounding emission up to $\sim$ 20 keV energies. All together the three instruments offer a unique opportunity to characterize this PWN in X-rays with unprecedented detail.

5.3.1 *Imaging Results*

We generated exposure-corrected *Chandra* image of the system in the 4.0-8.0 keV energy band while merging all the three archived observations to compare with images obetained from other two instruments in the similar energy range. We also produced an exposure-corrected image in the energy range 2.0–7.0 keV after combing the two on-axis observations for the study the the pulsar. For *XMM-Newton* data we generated merged images in two energy bands: soft (0.5-4.0 keV), hard (4.0-8.0 keV). We noticed that the PWN emission in *NuSTAR* data is dominant up to $\sim$ 20 keV; therefore, we only present imaging analysis below 20 keV hereafter. Photon events were selected in three energy bands: 4.0-10.0 keV, 10.0-20.0 keV and 20.0-79.0 keV. Such energy bands were selected to ensure a sufficient photon statistics in each image, as well as to minimize the effects of averaging the energy-dependent vignetting function over the energy range. *NuSTAR* mosaic images of two FPMs were generated in the aforementioned three band.

Fig. 5.2 displays the exposure-corrected skymaps of the PWN obtained with *Chandra*, *XMM-Newton* and *NuSTAR* in the 4-8 keV energy range (4.0-10.0 keV range for *NuSTAR*), together with the radio contours obtained from the SNRcat catalogue Ferrand and Safi-Harb 2012. All three instruments detected an extended emission around the position of the pulsar (see Figure 5.2). The *Chandra* analysis results, in particular, show that PSR B1853+01 is embedded in a bright cometary-tail like extended emission. In addition, unexpected extended emission feature ahead of the pulsar which resembles a pair of "antennae" is observed. Both the PWN tail and the antennae feature are detected in

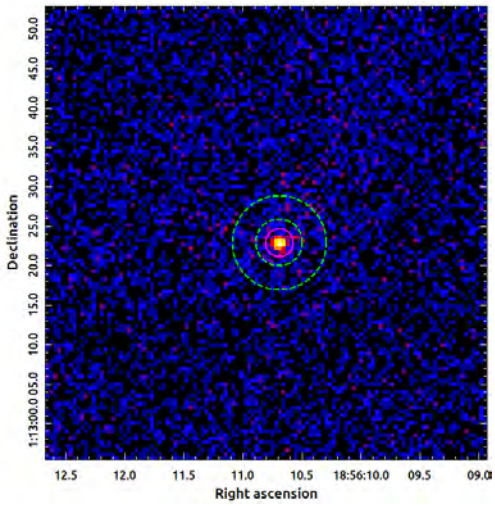

Figure 5.4: *Chandra* on-axis count image. The image is unbinned and unsmoothed. Both the circle and the anulus are centered at the pulsar position detected by *Chandra*. The magenta circle is of raidus 1.8″and is used for pulsar spectra extraction. The green dashed annulus has raii of 3″and 6″and is used as background region for the pulsar.

the *XMM-Newton* on-axis observations. In addition, large-scale, fainter emission encompassing both the PWN and the "antennae" structures is obtained in dedicated binned and smoothed *XMM-Newton* merged images. This will be refereed as to the "halo" structure.

In the case of *NuSTAR*, we could not resolve the "antennae" structures out from the PWN emission. Our results only show an spindle-shaped emission tapering the PWN region toward each end that can be seen up to energies as high as 20 keV and also a hint of a large scale structure at the same position as the large scale structure revealed in the *XMM-Newton* images. We note that this is the first direct detection of this PWN above 10 keV. Also also there seems to be some contamination from the nearby source 2CXO J185613.6+011207 as one can see from the right panel of the Fig. 5.2 where the the contour map extracted from *Chandra* image is overlaid.

5.3.1.1 *The Pulsar B1853+01*

Two on-axis *Chandra* observations (Obs.ID. 5548 and 6613) were used to study the compact emission from the pulsar. An unbinned and unsmoothed count image (see Fig. 5.4) using the two observations and using a wide energy energy (2.0-7.0 keV) was used to constrain the emission from the pulsar, as the bright pulsar emission can easily dominate over that from the PWN and also from the thermal emission from the SNR even in a wide energy range. We performed a source detection using the `wavdetect` tool to this combined count fits file with dedicated PSF and exposure maps to pinpoint the pulsar position,

Table 5.4: Position of PSR 1853+01.

	R.A. (J2000.0)	Decl. (J2000.0)
Radio[a]	18 56 10.79± 0.04	1 13 28 ± 2
ASCA (GIS)	18 56 10.0±1.5	1 13 17 ±40
ASCA (SIS)	18 56 12.6 ±1	1 12 34±30
Chandra[b]	18 56 10.69 ± 0.01	01 13 22.9±0.1

which is found to be at R.A.(J2000)= 18^h 56^m 10.68^s, DEC.(J2000)=+01^o 13 ′22.9″. In Table 5.4, we summarize the positions of PSR B1853+01 as retrieved in radio, in previous X-ray measurements, and the resulting position from our work.

In the *XMM-Newton* MOS images obtained from the analysis of the on-axis Obs. 0551060101 data, the centroid of the brightest pixels is found to lie about 4" north to the position obtained as mentioned above from the *Chandra* on-axis observation data sets. Instead, the centroid of the brightest pixels in the images obtained from Obs. 721630101, 721630201 and 721630301 conincide well with the *Chandra* pulsar position. We thus conclude that that a possible position offset exists in Obs. 0551060101. As for *NuSTAR*, the centroid of the brightest pixels in the 4.0-20.0 keV mosaic image is located ∼6" southwest from the derived *Chandra* pulsar position, yet this is well within the instrument systematic uncertainties (which is about ∼8" for the brightest targets Harrison et al. 2013 as mentioned before in Chapter 3).

5.3.1.2 *The PWN Tail*

The exposure-corrected and merged *Chandra* image (Fig. 5.2) reveals a tail feature trailing the pulsar. This tail stretches toward approximately the southeast-northwest direction, as far as ∼1.5 arcmin (or ∼1.3 pc at an assumed distance about 3 kpc), about half the extent in radio (Frail et al. 1996). A gap half way along the tail is clearly seen in *Chandra* (and also in *XMM-Newton* and *NuSTAR*) images dividing the tail morphologically into two parts: a compact nebula (CN) in the pulsar's very vicinity, and a relatively fainter "dropped tail" feature which is half the brightness of the CN. A hint of a small extended feature with an angle to the pulsar moving direction (protruding to the northeast), of similar brightness as the dropped tail, is also apparent in the binned and smoothed *Chandra* images.

5.3.1.3 *The "Antennae"*

Two strikingly large X-ray structures extending ahead of the PWN are detected in the binned and smoothed *Chandra* (see Fig. 5.2). This emission region extends to the south of the pulsar up to ∼1 arcmin (or ∼0.8 pc) and covers approximately 1000 $arcsec^2$ in the sky. *Chandra*

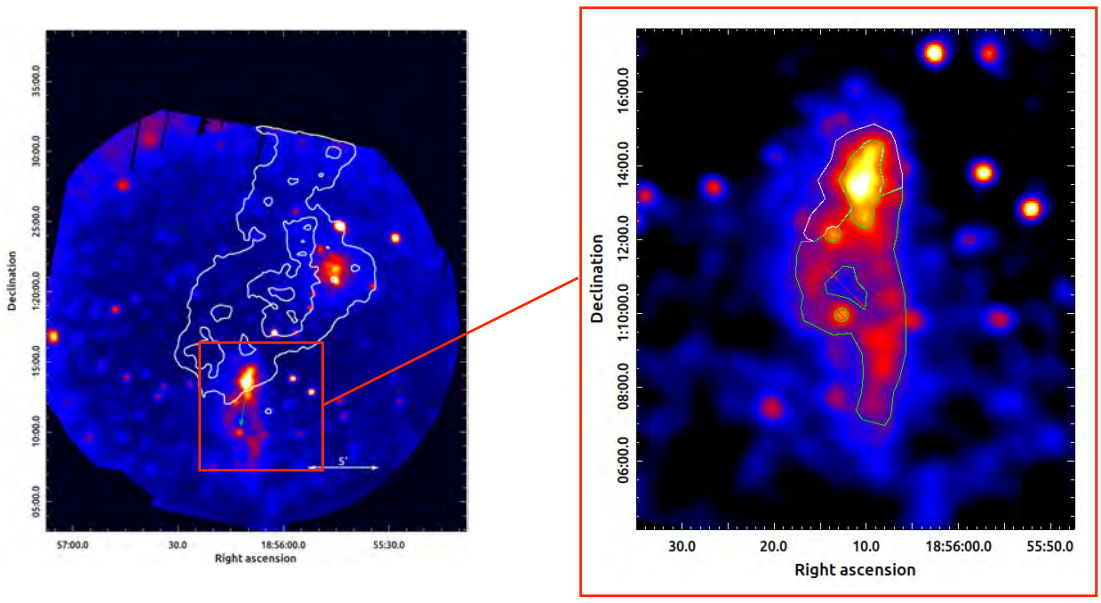

Figure 5.5: **Left**: *XMM-Newton* exposure corrected mosaic images of W44 region in the hard energy range 4.0-8.0 keV. White contours are taken from the soft 0.5–4.0 keV *XMM-Newton* image in Fig. 5.1. The green arrow shows the approximate direction of the pulsar's proper motion inferred from the pulsar's position relative to the SNR center. **Right**: Extended emission structures detected around PWN B1853+01 in the hard 4.0–8.0 keV energy range. The central bright region (consisting of the PWN tail and the antennae) clearly seen in the close vicinity of the pulsar is of similar size to that observed with *Chandra*. The image also shows faint emission surrounding the PWN, which we tentatively identify with an X-ray halo. The halo region is divided into two subregions (green solid line): northern halo (part of the halo inside of the SNR thermal X-ray emission) and southern halo (one outside of the SNR thermal X-ray emission region). It is worth noticing that the southern halo takes the morphology of the antenna feature observed just ahead of the pulsar.

is able to resolve this region in great detail: the 4.0-8.0 keV skymap in Figure 5.2 shows extended emission protruding from the south of the pulsar location and then breaking into two antennae-like features. A clear gap exists halfway down the stream before the branching. *XMM-Newton* could barely resolve the extended feature from the CN/PSR emission, yet it does detect the gap between this extended emission and the southern branched antennae structures. These findings are in good agreement with the observed features detected with *Chandra* in the hard X-ray bandPetre et al. 2002. *NuSTAR*, on the other hand, cannot resolve the emission from the antenna region. However, the edge of the bulk emission towards the south seems to coincide with the tips of the antenna region in *Chandra*.

5.3.1.4 *The X-ray Halo*

The pulsar, the PWN tail and the antennae structures are surrounded by a relatively faint extended X-ray emission, which we were able to trace thanks to the large data set available and the high sensitivity of *XMM-Newton*. This surrounding extended X-ray emission, which we identify as an X-ray alo, displays an averaged surface brightness which is dimmer than that of the PWN and CN by a factor of $\sim$3.

In Fig. 5.5, we show *XMM-Newton* merged background subtracted and exposure corrected images in the 4.0-8.0 keV band where large-scale extended emission close to the position of the PWN is found. Other serendipituous sources are found as well in the FoV, one of them possibly associated to a galaxy cluster(Uchida et al. 2012; Nobukawa et al. 2018). A closer look into this extended emission through highly smoothed maps (see right panel of Fig. 5.5) reveals that the core nebula is surrounded by a rather faint extended emission with the southern encompassing the two antenna features. This is in fact consistent with the results obtained with ASCA at energies 4.0-9.5 keV (Harrus et al. 1996). The PWN looks elongated towards the south in ASCA, although (Harrus et al. 1996) only noted that the position of the new hard X-ray source is consistent with that of the pulsar, while it is marginally inconsistent with the peak position of the diffuse radio nebula to the north. In Okon et al. 2020, the 4-8 keV W44 MOS+pn skymap also shows a hint for this large-scale structures. Our larger data set allow us to better constrain the spatial extent of these antennae-like structures, which reach distances of about 6 arcmin/3′(or 5/2.5 pc at an assumed distance to the source $d_{\rm PWN} = 3$kpc). At closer distances to the pulsar, two brighter and slightly elongated structures are apparent in the *Chandra* maps, which seem to protrude from the PWN itself in the same direction as the large antennae, prompting for their association. The northern part of the extended X-ray halo-like emission follows instead the overall shape of the PWN tail, extending only about half arcmin outwards from the core nebula. Our results from *NuSTAR* confirm the existence of this large antenna structure revealed by *XMM-Newton*, extending the detection up to $\sim$ 10 keV (see Fig. 5.2).

We also searched for this halo feature and in particular the larger antennae structure in the southern part of the halo in *Chandra* images. However, due to the orientation of the ACIS array, the two on-axis observations failed to cover this area. Only in Obs.ID 1958, this area was observed. However, most of this feature falls on the edge of the S2 chip and the front illuminated S0 Chip, which accounts for a background noise rates. We could not therefore confidently confirm the excesses from these extended regions with our *Chandra* data set.

Table 5.5: Spectral-fitting Results for PSR B1853+01

Dataset	Best-fitting Values			$\chi^2_{\rm red}$ (d.o.f)
	$N_{\rm H}$ ($\times 10^{22}$cm^{-2})	Γ	*Norm*[a]	
tbabs × PL:				
Chandra	$0.65^{+0.46}_{-0.42}$	$1.87^{+0.48}_{-0.43}$	$1.22^{+0.86}_{-0.49} \times 10^{-5}$	1.01(16)
XMM-Newton	$0.75^{+0.17}_{-0.14}$	$1.70^{+0.17}_{-0.16}$	$1.45^{+0.35}_{-0.28} \times 10^{-5}$	0.97 (248)
NuSTAR[b]	0.65 (fixed)	$1.91^{+0.42}_{-0.43}$	$8.24^{+10.37}_{-5.39} \times 10^{-5}$	1.20 (19)

Note: [a] photons/keV/cm^2/s @ 1 keV. [b]value for FPMA; for FPMB Norm is $9.83^{+8.76}_{-4.52} \times 10^{-5}$

5.3.2 *Spectral Results*

To conduct spatially resolved spectral analysis, we defined the following regions: (1) the pulsar region, (2) the PWN tail region (excluding the pulsar itself), the cometary tail, (3) the antenna-like structures ahead of the pulsar, and (4) a faint halo region encompassing the three aforementioned regions. We also defined several background regions to compute the spectral fits. The XSPEC (Arnaud 1996) software (version 12.9.0) was used for the spectral analysis while the Tuebingen-Boulder ISM absorption model `tbabs` with the abundances from Wilms et al. 2000 was used to calculate the X-ray absorption in the ISM. Below, uncertainties are given at 90% confidence level unless specified otherwise.

5.3.2.1 *The Pulsar B1853+01*

The contamination from the surrounding SNR in the soft X-ray (below ∼4 keV) band heavily affected the spectral analysis of the PWN. For the pulsar, however, the analysis is less affected as the extraction region is relatively smaller. Hence, pulsar spectra were fitted to determine the $N_{\rm H}$ value towards the system.

For *Chandra* data, a circular region with 1.8" radius centered at $\alpha(2000) = 18^{\rm h}56^{\rm m}10.69^{\rm s}$, $\delta(2000) = 01^\circ13'22.9''$ was defined as the extraction region for PSR B1853+01. To remove contamination from the PWN, the background region was chosen to be a $3'' - 6''$ annulus centered on PSR B1853+01 (see Fig. 5.4). The spectra were combined and then grouped to have a minimum of 20 counts/bin. We fitted the pulsar spectrum from 0.5 to 8 keV. The best fit using an absorbed power-law emission model, "tbabs × PL", yields a column density of $N_{\rm H} = 0.65^{+0.46}_{-0.42} \times 10^{22}$cm^{-2}, a photon index of Γ=$1.87^{+0.48}_{-0.43}$, a normlization of $1.22^{+0.86}_{-0.49} \times 10^{-5}$ photons/keV/cm^2/s and an observed flux in the 0.5-8.0 keV band of 4.12×10^{-14} ergs cm^{-2} s^{-1} (reduced χ^2 = 1.01 with 16 degrees of freedom). Fitting the pulsar spectra with an absorbed blackbody model alone ("tbabs × BB") gives an unrealistically low column density with a large error. Parameters could not be well

constrained neither when fitting the pulsar spectra with an absorbed blackbody plus a power law emission model. We also tried to extract the pulsar spectrum with different background regions and we found they all give consistent results.

Our best-fit pulsar photon index value, however, is different from what was obtained in Petre et al. 2002, $\Gamma = 1.28 \pm 0.48$, which is remarkably harder. We note that this result was obtained after considering a column density of W44 on the order of $5 \times 10^{22} cm^{-2}$ taken from Rho et al. 1994, which also differs from our findings. Our column density value is instead consistent with what was obtained by Harrus et al. 2006, where the pulsar spectrum was extracted from a radius of 20" centered at $18^{\circ}56'11''$ $1^{\circ}13'24''$ using *XMM-Newton* observations, and was best described by an absorbed power law model with $\Gamma = 2.2^{+0.49}_{-0.42}$ and $N_{\rm H}$ =$0.6 \pm 0.2 \times 10^{22}$ cm^{-2}. Harrus et al. 1996 presented on the other hand the analysis of ASCA observations of the X-ray synchrotron nebula associated with PSR B1853+01, in which data were extracted from a circular region of radius of $\sim 5'$ centered on the radio pulsar position and they obtained a photon index of about $2.3^{+1.1}_{-0.9}$, and a column density of $(1.82 \pm 0.05) \times 10^{22} cm^{-2}$.

For *XMM-Newton*, given the different PSFs of the detectors, we defined extraction regions of different sizes. For the on-axis observation Obs.551060101 the pulsar region is centered at the centroid of the brightest pixels with radii of 7" for MOS and 9" for pn. The background region is a concentric annulus with radii 8"-11" for MOS and 10"-13" for pn. For the other off-axis observations, the pulsar extraction region are circles with radii of 9" for MOS and 11" for pn, respectively, again centered at the centroid of the brightest pixels, while the background region is a concentric annulus with radii 10"-13" for MOS and 12"-15" for pn. We then fitted the combined pulsar spectrum, grouped with minimum 30 counts/bin and adopting a wider 0.5 to 10.0 keV range. We found that the emission is best described with an absorbed power-law model with $N_{\rm H}$ = $0.75^{+0.17}_{-0.14} \times 10^{22} cm^{-2}$ and $\Gamma = 1.70^{+0.17}_{-0.16}$ (see Table 5.5) which is, within errors, consistent with what we obtained with *Chandra* data. The column density value obtained from fitting the *Chandra* pulsar spectrum $N_{\rm H}$ =0.65×10^{22}cm^{-2} will thus be used in the remainder of the spectral analysis.

For *NuSTAR*, pulsar spectra were extracted from a circular region of 18" fixed at the centroid of the brightest pixels and grouped to have at least 200 counts per bin. Having $N_{\rm H}$ fixed at 0.65×10^{22}cm^{-2}, we get a $\Gamma = 1.91^{+0.42}_{-0.43}$ with $\chi^2_{\rm red}$ (d.o.f) of 1.20 (15), when fitting in the energy range 3 to 10 keV, and $\Gamma = 2.09^{+0.29}_{-0.29}$, $\chi^2_{\rm red}$ (d.o.f) of 1.04 (19) when extending the fit to the range 3 to 20 keV. We also tried a bit larger extraction radius (r=29") for the pulsar, obtaining $\Gamma = 2.20^{+0.27}_{-0.27}$, with $\chi^2_{\rm red}$ (d.o.f) of 0.75 (36) in the 3-10 keV energy range, and $\Gamma = 2.09^{+0.20}_{-0.19}$, with $\chi^2_{\rm red}$ (d.o.f) of 0.78 (47) when fitting from 3 to 20 keVs.

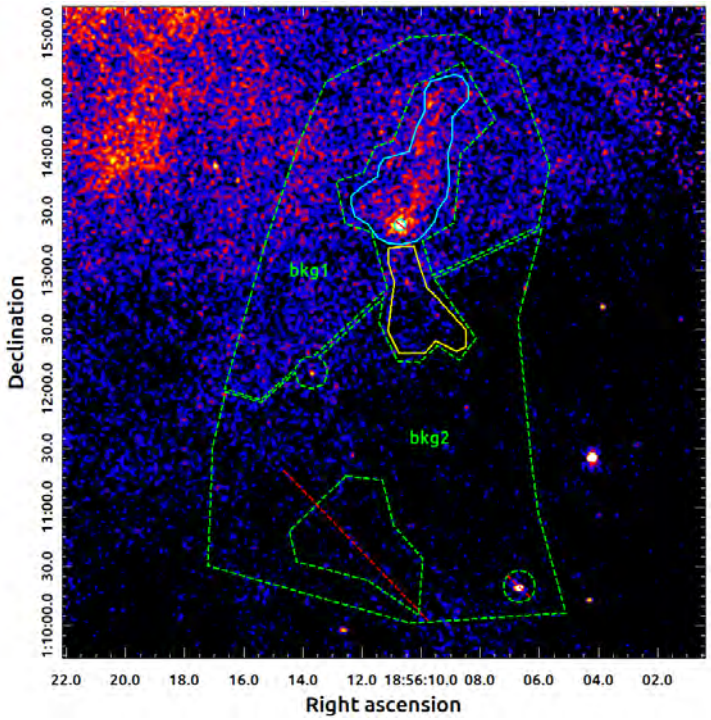

Figure 5.6: Merged *Chandra* broad band (0.5-7.0 keV) flux image with extraction regions used for spectral extraction overlaid. The image is unbinned yet smoothed with a Gaussian function with radius r=3 pixel and sigma σ=1.5 image pixels. Weighted spectra have been extracted from tail (solid cyan) region with pulsar (r=3") excluded, using bkg1 region (dashed green) as background region, and from antenna region (solid yellow) using bkg2 region (dashed green) as background region.

5.3.2.2 *Spatially Resolved Spectra*

Spatially-resolved spectra around the PSR were extracted for both the *Chandra*, *XMM-Newton*, and *NuSTAR* data sets. For *Chandra* observations, weighted spectra were extracted from the tail and antenna regions as shown in Fig. 5.6, combined and grouped to have at least 20 counts per bin, and then fitted with an absorbed power-law model. Knowing from the imaging analysis in XMM that the PWN is inside a halo structure, we chose a background region similar to the part of XMM halo structure inside the thermal SNR around the tail and a background region for the antenna region taking a part of the XMM halo structure outside the thermal SNR but still enclosing the antenna region.

The combined tail spectrum was fit with a power law from 3.0 to 8.0 keV (to minimize the effect of the residual thermal emission) with the column density fixed at the best-fit value obtained with *Chandra*. We found a photon index of $\Gamma = 2.01^{+0.39}_{-0.38}$, $\chi^2_{\rm red}$= 0.98 (with 53 d.o.f.) for the tail region. We tried to divide the tail region into two parts (CN and dropped tail). However, the low statistics prevented

Table 5.6: *Chandra* spatially resolved Spectra

Region	Γ	Norm[a]	$\chi^2_{\rm red}$(dof)
Tail[b]	$2.01^{+0.39}_{-0.38}$	$9.03^{+6.58}_{-3.79} \times 10^{-5}$	0.98 (53)
Small antennae	$1.24^{+0.23}_{-0.24}$	$0.80^{+0.23}_{-0.21} \times 10^{-5}$	1.01 (82)

Note: [a] photons/keV/cm^2/s @ 1 keV.

us from obtaining meaningful results when cutting out the thermal radiation at the low energy band. Spectra were also extracted from the antennae region. The best power-law fit it in the energy range $0.5 - 8.0$ keV probiides a rather hard photon index, $\Gamma = 1.24^{+0.23}_{-0.24}$, for this region. The inspection of dedicated skymaps produced at different energy bands confirms that the emission is only visible above 2.0 keV, confirming its non-thermal and hard spectral nature.

The southern part of this halo feature could not be seen using MOS1 in Obs ID.0700001, 0700002, 0700003, since these observations were taken after the loss of MOS1 CCD3 (these structures happened to fall on CCD3 of MOS1 during these three observations). For *XMM-Newton* observations we only use pn data from Obs. 721630101, 0721630201 and 072163030 as the whole PWN and Halo system only falls completely on one of the pn chip in these observations. We extracted spectra from the tail and the antenna regions and grouped the combined spectra to have at least 30 counts/bin. The high sensitivity of XMM-Newton allowed us to split the tail region into two parts: the CN and the dropped tail. We fit from 3.0 to 10. keV using an absorbed powerlaw model with $N_{\rm H}$ fixed to 0.65×10^{22}cm^{-2} as the low energy part is heavily affected by background subtraction. For the antenna region because it is outside of the thermal X-ray emission from SNR, its spectrum is less affected in the low energy part hence we fit from 0.5 to 10.0 keV. Spectral results are shown in Table 5.2. We also tried to extract spectra from the halo region. The low surface brightness of this feature made us to combine and group the spectra from the two subregions to have at least 200 cts per bin. Since spectra seemed to be rather noisy below 3 keVs and accounting for some copper line emission due to the detector itself also presentin the low/energy end of the fit range, we proceeded to limit the fit from 3.0 keV to 10.0 keVs.

For *NuSTAR* data, spectra have been extracted from region A, C and D as shown in Fig.5.9. Region A is similar to the antenna region, region C is similar to the dropped tail region and region D is similar to the part of the southern halo where one of the large antenna feature lies. We fitted the *NuSTAR* spectra with photon indices and the column density linked for the two detector modules, while normalization parameters were allowed to vary to take into account the small relative calibration uncertainties between the two modules. For the spectral

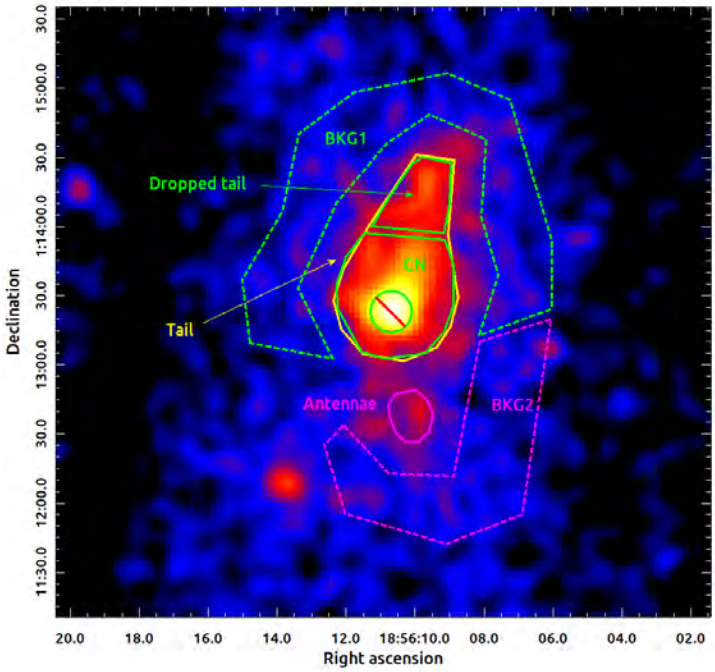

Figure 5.7: 4.0-8.0 keV merged *XMM-Newton* pn image from obs. 0721630101, 0721630201, and 0721630301.The extraction regions for the tail region (solid yellow) and the anteannae region are shown. The tail region can be further split into two subregions: CN and dropped tail (both are solid green lines). A background region inside the thermal X-ray emission area BKG1 (dashed green) was chosen for the tail regions while one outside BKG2 (dashed magenta) for the antenae.

Table 5.7: *XMM-Newton* spatially resolved spectra

Region	Γ	Norm[a]	$\chi^2_{\rm red}$(dof)
Tail	$1.84^{+0.19}_{-0.18}$	$4.36^{+1.47}_{-1.11} \times 10^{-5}$	1.29(118)
CN	$1.75.^{+0.22}_{-0.21}$	$2.67^{+1.06}_{-0.77} \times 10^{-5}$	1.13(80)
Dropped tail	$1.86^{+0.40}_{-0.38}$	$1.00^{+0.83}_{-0.46} \times 10^{-5}$	1.33(29)
Antenna	$1.37^{+0.31}_{-0.33}$	$0.13^{+0.06}_{-0.05} \times 10^{-5}$	0.75(46)
Northern halo	$1.68^{+0.24}_{-0.24}$	$4.16^{+1.92}_{-1.33} \times 10^{-5}$	1.91(21)
Southern halo	$1.44^{+0.32}_{-0.32}$	$8.20^{+5.15}_{-3.23} \times 10^{-5}$	1.34(52)

Note: [a] photons/keV/cm^2/s @ 1 keV.

fitting presented here we freeze the $N_{\rm H} = 0.65 \times 10^{22} {\rm cm}^{-2}$. We fit the *NuSTAR* spectra in the 3 to 20 keV band, above which the detector background dominates.

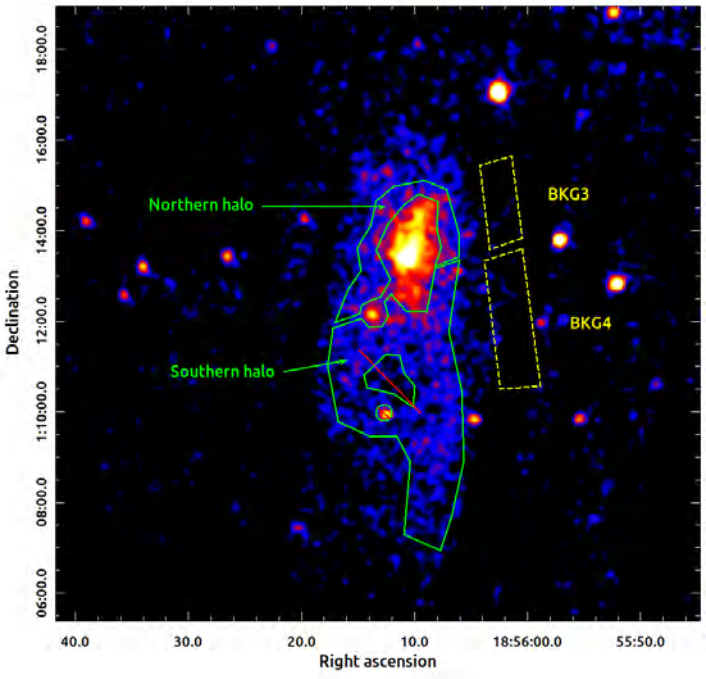

Figure 5.8: 4.0-8.0 keV merged *XMM-Newton* pn image from obs. 0721630101, 0721630201, and 0721630301.The extraction regions for the halo region are shown. The halo region is divided into two subregions (solid green lines): the northern halo and the southern halo. Background regions (dashed yellow lines) for these two regions of interest are BKG3 and BKG4 respectively.

Table 5.8: NuSTAR Spatially Resolved Spectra of PWN Regions

Region	Γ	Norm^a FPMA	Norm^a FPMB	$\chi^2_{\rm red}$(dof)
Region A	$2.04^{+0.37}_{-0.36}$	$2.49^{+2.47}_{-1.30} \times 10^{-5}$	$2.39^{+2.34}_{-1.23} \times 10^{-5}$	0.40(21)
Region C	$2.48^{+0.31}_{-0.30}$	$7.90^{+5.58}_{-3.34} \times 10^{-5}$	$9.16^{+7.05}_{-4.13} \times 10^{-5}$	1.28(36)
Region D	$1.90^{+0.26}_{-0.26}$	$10.96^{+6.98}_{-4.42} \times 10^{-5}$	$3.03^{+2.79}_{-1.62} \times 10^{-5}$	1.11(125)

Note: ^{a} photons/keV/cm^2/s @ 1 keV.

5.4 DISCUSSION ON PWN B1853+01

The following discussion is based on the assumption that PSR B1853+01 is located within the SNR W44. However, we cannot rule out the possibility that pulsar might be actually in front of W44 (which would otherwise agree with the slightly lower best-fit value for $N_{\rm H}$ compared to that of the SNR reported in Okon et al. 2020, $\sim 1.8 \times 10^{22}$ cm^{-2}, although this is highly speculative as the fit results are consistent within uncertainties). In our model, the wind momentum flux from the pulsar balances the ram pressure from the surrounding medium, likely the

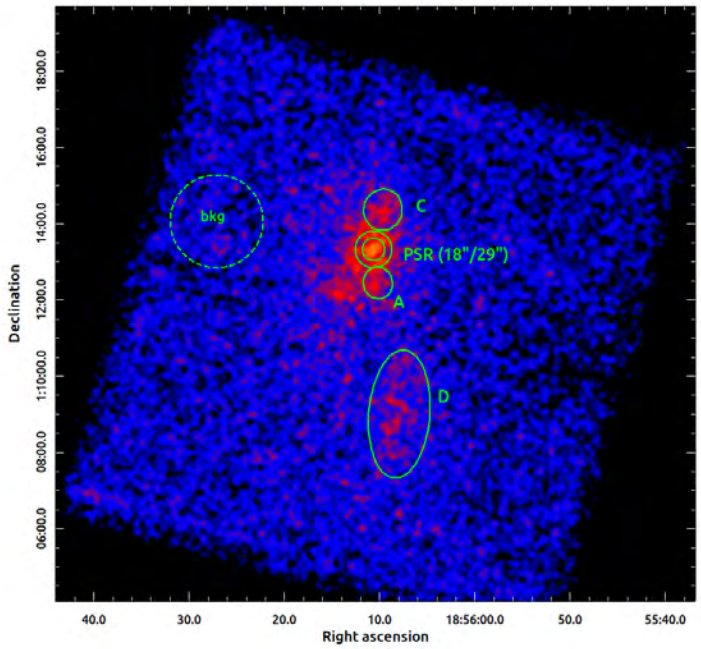

Figure 5.9: *NuSTAR* mosaic image in 3.0 to 20.0 keV with extraction regions shown. Pulsar spectra were tried to extract with circles of two different radii 18"/29". Region A is similar to the antenna region, Region C is similar to the dropped tail region and D is similar to part of the southern halo where one of the large antenna feature lies. Background region is shown in dashed green circle.

shocked supernova ejecta. The *Chandra* X-ray imaging shows that the angular separation from the pulsar position to the nearest edge of the CN in the direction of the pulsar motion is about 8", allowing us to estimate the standoff distance, d_0, to be approximately 0.16 pc (assuming a proper motion for the pulsar in the plane of the sky), considering a distance of 3 kpc to the pulsar. For the ambient mass density ρ_0, we adopt the method used by Frail et al. 1996, which includes a 10% helium composition by mass. Thus, $\rho_0 v^2_{\rm PSR} = 2.3 \times 10^{-10} n_0 v^2_{100}$ ergs cm^{-3}, with $n_0 = 0.25$cm^{-3} near the pulsar (Jones et al. 1993), and v_{100} represents the pulsar's velocity in units of 100 km s^{-1}. Our findings indicate a moderate pulsar velocity $V_{PSR} \geq 40$ km^{-1}, considerably lower than the 375 km s^{-1} estimated by Frail et al. 1996 based on radio data. This is entirely due to the fact that the standoff distance angular size in the radio images is $\lesssim 1''$. For our X-ray images, this d_0 is in fact an upper limit, as it indicates the drop of the radial profile flux along the pulsar motion, and could therefore include the contribution from the shocked ISM medium. Future, more precise measurements of the pulsar's velocity could be achieved, e.g., with advanced radio interferometry techniques.

The analysis of the *Chandra*, *XMM-Newton* and *NuSTAR* data reported in the previous Sections reveals the presence of several X-ray

structures that extend around and beyond the PWN in PSR B1853+01. These structures are likely powered by the pulsar itself, as no other high energy source is known in the region (apart from the W44 SNR itself, but previous studies indicate that it mainly contributes to thermal X-ray emission, below 4 keV). The large extension of these structures implies in turn that the X-ray radiating particles have escaped the PWN region. Extended misaligned X-ray outflows associated to BSPWNe have been reported for a number of sources in recent years (see e.g. Pavan et al. 2014; Klingler et al. 2016a; Wang 2021; de Vries and Romani 2022). Their extension, also much larger than the parent PWN, and the difficulties in associating a ballistic origin for these outflows, prompted for an alternative explanation in which these jet-like structures are the result of electrons/positrons escaping the BSPWN and emitting synchrotron radiation in the ISM magnetic field (Bandiera 2008). In most of these known cases the misaligned outflows keep remarkably collimated up to distances of a few pc (see e.g. the jet-like structures in the Guitar or the Lighthouse nebula). The jet-like features in PWN B1853+01 display also an antenna-like structure, which probably indicates the ISM magnetic field structure underneath. Considering that PSR B1853+01 is moving actually at the edge of the thermal X-ray emission region, it could well be that the pulsar is experiencing a relatively abrupt change of environment, leading to an enhancement of particle escape from the bow shock. Also, the antennae and southern halo seem to have rather hard spectra compared to that of the pulsar or the PWN tail. This further suggests that the origin of these extended structures is related to particle escape processes operating in the source.

The most striking property of the faint extended X-ray halo emission is the fact that it surrounds the source in almost all directions, while closely following the morphology of the central, compact PWN. This fact may provide valuable clues to constrain diffusion processes of escaped high energy particles in the surrounding medium, as it is done in the case of TeV halos (Linden et al. 2017; Giacinti et al. 2020; López-Coto et al. 2022). In this sense, it is worth noting that the energy of electrons radiating synchrotron emission at keV energy band could reach multi-TeV energies. Therefore, the same electrons could be responsible for the inverse-Compton radiation observed in the TeV energy band. Some of the TeV halos candidates detected in recent years by ground based very-high-energy gamma-ray facilities (Abeysekara et al. 2017; Aharonian et al. 2021; Albert et al. 2023) may then be accompanied by morphologically similar X-ray halos Linden et al. 2017. The ratio of the X-ray and TeV halo intensities would then depend on the ratio of the magnetic field to the ISRF energy densities.

We argue that the two X-ray halo structures surrounding PWN B1853+01 and the Snail Nebula can be interpreted as proper X-ray halos. The two systems share indeed great similarities as both are

located inside of their parent SNRs and both display antennae-like structures, in addition to the fainter X-ray halo structure (Temim et al. 2009, 2015). Temim et al. 2009 suggested that the prong features observed in the Snail nebula as well as the cometary tail morphology of the compact nebula are the result of the passage of the SNR reverse shock. They also modeled a SN blast wave expanding in a ISM with a non-uniform density that decreases from west to east, with the pulsar moving towards the north with a velocity of 400 km s^{-1}, to explain the offset between the X-ray PWN and the radio PWN. Additionally, the Snail nebula source is known to produce bright TeV emission spatially extended and coincident with the PWN (H. E. S. S. Collaboration et al. 2018). A scenario in which the BSPWN inside of SNR G327.1-1.1 is leaking energetic electrons could explain both the prong-like structures and the faint halo emission observed in X-rays and in the TeV band.

So far no emission at GeV or TeV energies have been detected confidently from PWN B1853+01. The 95% confidence contour for the EGRET source 3EG 1856+0114 coincides with the southeastern sector of the SNR W44 (Thompson et al. 1996). de Jager and Mastichiadis 1997 explained the observed GeV gamma-rays in terms of relativistic bremsstrahlung and IC scattering produced by a power-law distribution of relativistic electrons injected by PSR B1853+01. While this constitutes a possible explanation, a significant part of the gamma-ray flux observed may also be due to SNR shock-cloud interactions. In this regard, GeV emssion has instead been reported from two extended gamma-ray structures located at the two opposite edges of the remnant along its major axis (Peron et al. 2020). At VHEs, MAGIC conducted recently an observation campaign on the northern part of the W44 SNR. No significant emission was found, despite that detectable fluxes are expected in this energy range on theoretical grounds (Aharonian et al. 1997), suggesting a spectral cutoff between GeV and TeV energies.

6

RADIO EMISSION FROM ESCAPING ELECTRONS IN THE LIGHTHOUSE NEBULA

6.1 INTRODUCTION TO THE LIGHTHOUSE NEBULA

Originally discovered by INTEGRAL as an unidentified hard X-ray source, IGR J11014-6103 (also known as the "Lighthouse Nebula"; Pavan et al. 2014) is located $\sim$ 11 arcmins southwest of its likely progenitor supernova remnant SNR MSH 11-61A, at a distance of ~ 7 kpc from the Sun (see García et al. 2012). The Lighthouse Nebula is powered by PSR J1101-6101, displaying a period of $P = 62.8$ ms and an estimated spin-down energy of $L_{sd} = 1.36 \times 10^{36}$ erg s^{-1} (Halpern et al. 2014). Observations in the X-ray band have revealed a complex system morphology, including a trailing PWN, shaped in a narrow cone elongated toward the parent SNR, and prominent X-ray jet-like structures oriented nearly perpendicular to the PWN axis (see Pavan et al. 2016). At radio energies, extended emission has been detected with ATCA at 2 GHz from the IGR J11014-6103 tail (Pavan et al. 2014). This emission is not spatially coincident with that observed at X-rays, with the peak of the radio emission being separated further away along the tail by about 22′ ′ with respect to the X-ray maximum.

The jets observed in the Lighthouse Nebula display a rectilinear structure extending for more than 10 pc into the surrounding medium (see Fig 6.1). Their X-ray luminosity is unusually high, at the level of that retrieved from the pulsar, representing altogether a few percent of the pulsar spin-down power, $L_{sd} \sim 10^{36}$ erg s^{-1}. The jet X-ray spectrum is moderately hard, with photon indices $\Gamma_{\mathrm{X,\,jets}} \approx 1.6$, whereas the tail region displays $\Gamma_{\mathrm{X,\,tail}} \approx 1.9$. Both the jet spectral hardness and its high X-ray efficiency may be expected if these are magnetic jets carrying a hard electron distribution, and there is an amplified magnetic field along the jet structures (see e.g. Bykov et al. 2017). However, accounting for the high-speed velocity of the source, $v_{\mathrm{psr}} \gtrsim 1\,000$ km s^{-1}, the absence of any significant bending along their $\gtrsim 10$ pc extension prompts for alternative mechanisms for the production of such jet-like structures. Other BSPWNe have been interpreted in a diffusion scenario (Bandiera 2008), and rectilinear structures or “filaments” have also been recently reported from the Galactic Center region (MeerKAT Collaboration 2018), and discussed as “kinetic jets” of escaping particles diffusing into the ambient magnetic field (Barkov and Lyutikov 2019). It is therefore currently uncertain whether the jet-like structures in the Lighthouse Nebula are ballistic jets carrying an amplified mag-

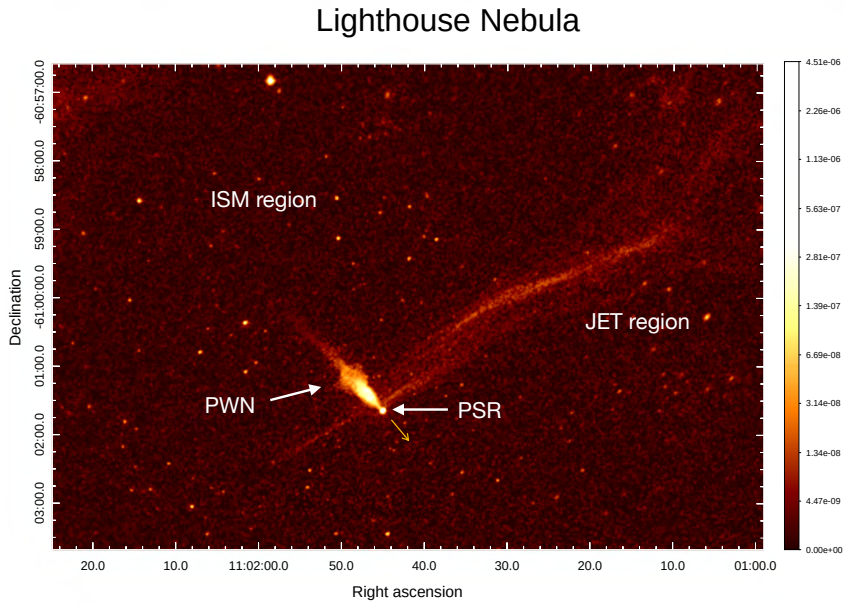

Figure 6.1: *Chandra*/ACIS exposure-corrected broadband (0.5 – 7.0 keV) flux image of IGR J11014–6103 (the "Lighthouse Nebula"). The image has been produced using all *Chandra* archival observations of the Lighthouse Nebula, for a total of $\sim$ 365 ks, merged using CIAO's `merge_obs` tool, and smoothed using a 2D Gaussian kernel with radius on a pixel size of 0.492″ and has been smoothed with a 2D-Gaussian kernel with radius = 1.7″ and $\sigma = 0.7$″.

netic field or filaments of escaping high-energy electrons from the BSPWNe into the ISM.

In this Thesis we have modeled the expected radio emission produced by high-energy electrons escaping into the ISM, where they radiate in the ISM magnetic field. After a brief description of the source, in Section 6.2 we outline the model used to describe the emitting electron population and their diffusion into the ISM. Section 6.3 provides particle and radiation distributions, as well as synthetic maps at radio wavelengths used to predict the expected signal for dedicated observations of the source by highly sensitive facilities. Section 6.4 discusses the potential of radio observations to constrain the origin of the jet-like structures observed from BSPWNe.

6.2 Modeling the radio emission in a diffusion scenario

PSR J1101-6101 in the Lighthouse Nebula displays a spin-down power of 1.36×10^{36} erg/s (Halpern et al. 2014). Observations with the *Chandra* satellite report a 2–10 keV X-ray flux from the jets at the level of 6×10^{-13} erg cm^{-2} s^{-1}, whereas spectral analysis suggests a synchrotron origin rather than a thermal emission scenario (Pavan et al. 2014). Particles accelerated at the Lighthouse Nebula that are responsible for this emission could therefore also emit in the radio band.

Under these premises, we consider the presence of a nonthermal population of relativistic electrons injected close to the BSPWNe bow shock, carrying a total kinetic luminosity $L_{\rm inj} \approx L_X \times t_{\rm sync}/t_{\rm dyn}$. Here L_X is the jet X-ray luminosity derived from *Chandra* observations (we assume a distance to the Lighthouse Nebula of $d_{\rm LN} = 7$ kpc), $t_{\rm sync}$ is the synchrotron cooling time for electrons emitting at the characteristic frequency $h\nu_c = 2$ keV in a given magnetic field B, $t_{\rm sync} \approx 460\,(B/30\mu{\rm G})^{-1/2}$ yr, and $t_{\rm dyn}$ is the dynamical timescale to travel along the jet-like feature, $t_{\rm dyn} \sim l_{\rm jet}/v_{\rm dyn}$; with $l_{\rm jet} \sim 10$ pc and $v_{\rm dyn} \sim c$, $t_{\rm dyn} \sim 32$ yr. A total power $L_{\rm inj} = 3 \times 10^{34}$ erg s^{-1} is therefore injected, which is distributed in energy following a power-law with index $\Gamma = 2$ and an exponential cutoff at both the low- and the high-energy ends of the particle spectrum at $\gamma_{\rm min}^{\rm cut}$ and $\gamma_{\rm max}^{\rm cut}$, respectively. A single power-law model has been assumed for simplicity in our model, although we note that PWNe could inject a more complex particle distribution displaying a spectral break following the presence of separate electron populations, for example those injected within the pulsar's light cylinder, and electrons accelerated at the shock between the pulsar wind and the external medium (see e.g. Atoyan and Aharonian 1996; Venter and de Jager 2007; Torres et al. 2014).

The low-energy cutoff is an assumption in our model, and it is treated as a free parameter, with two cases explored in this report:$\gamma_{\rm min}^{\rm cut} = 10^3$ and 10^5. Such a low-energy cutoff may be expected in case an energy selection mechanism is in place in IGR J11014-6103 for particles able to escape the PWN. We use $\gamma_{\rm max} = 10^8$ for the high-energy particle distribution cutoff, which should be attainable in the bow shock of a runaway pulsar such as IGR J11014-6103 (see e.g. Bykov et al. 2017). As for the spectral index, the value $\Gamma = 2$ is adopted for simplicity, but also because it predicts potentially detectable fluxes. If the electron distribution were much harder, then little emission would be produced in the radio band.

Particles injected close to the bow shock are assumed to escape the immediate BSPWNe region and diffuse into the surrounding medium, where they evolve with time due to radiation losses, both synchrotron and inverse Compton (IC) emission, the latter accounting for the surrounding cosmic microwave background (CMB) and infrared radiation fields ($U_{\rm CMB} \approx 0.25$ eV cm^{-3}, $U_{\rm IR} \approx 0.2$ eV cm^{-3}, Popescu et al. 2017). We evaluate the resulting cooled particle distribution at the present time, $t_{\rm LN} = 20$ kyr (Halpern et al. 2014). A sufficient number of particle injection events are considered, which are equally spaced along the source trajectory during this time, with Δt shorter than the typical synchrotron and IC cooling timescales for particle Lorentz factors $\gamma_e \lesssim \gamma_{\rm max}$. After injection, we consider electron diffusion in the surrounding ISM. A diffusion coefficient $D_{\rm diff}(E) = 3 \times 10^{27} \left(\frac{E/{\rm GeV}}{B/\,3\mu{\rm G}}\right)^{1/2}$ is assumed (Gabici et al. 2007). For simplicity, we assume that diffusion is isotropic from the injection point up to distances $l_{\rm diff} \sim (D_{\rm diff}\, t\,)^{1/2}$

(the medium is considered uniform, and thus adiabatic losses are not relevant).

Freshly injected particles, with injection times $t_{\rm inj} \leq 1$ kyr, are presumably responsible for the X-ray emission observed from the jet-like features in the Lighthouse Nebula. For this injection period we consider distinct conditions of the ISM, which we label as the "JET region", characterized by a magnetic field $B_{\rm JET} = 5$–30 μG that can be significantly higher than $B_{\rm ISM} \sim 5\mu$G under which electrons evolve after $t_{\rm inj} > 1$ kyr. The emission from particles injected until $t \sim 1$ kyr diffusing into this JET region, and the emission resulting from their later diffusion in the ISM region (for $t \gtrsim 1$ kyr), was computed separately. We emphasize however that the injected electron particle population is the same in the JET and ISM regions, only the value of the corresponding magnetic field for each region varies. The former are evolved until $t_{\rm inj} = 1$ kyr only, whereas the latter evolves from $t_{\rm inj} = 1$ kyr up to $t_{\rm inj} = 20$ kyr. The different conditions from the JET and ISM regions follow the assumption that the JET region corresponds to a temporary feature that relocates as the pulsar moves, and to which we assign a typical crossing timescale of ~ 1 kyr based on the JET apparent width and the pulsar velocity. The origin of the JET feature could be related to the pulsar motion pulling the threaded ISM magnetic field and, as the pulsar propagates, new ISM magnetic lines become entangled at the front of the PWN whereas the "older" ones relax and turn back into normal ISM magnetic field conditions.

Synchrotron emission is computed by employing the formulae in Pacholczyk 1970 together with the analytical approximations in Aharonian et al. (2010). The cumulative radio emission is evaluated throughout the area surrounding the source. Synthetic synchrotron emission maps are computed, which are then convolved with the beam of a radio telescope at GHz frequencies in order to obtain concrete observational predictions.

In this study we aim at predicting the radio emission produced in the surroundings of the BSPWNe, and therefore we do not attempt to model in detail the observed X-ray emission from the jet, including its morphological properties. In this regard, we only consider isotropic diffusion of particles injected in the JET and ISM regions. The effects that may result from anisotropies generated for example by the structured geometry of the underlying magnetic field, are therefore disregarded. Our estimates are based on assumed values for the injected kinetic energy, the energy distribution of the emitting particles, and on the ISM and JET regions' magnetic field values. We do not consider higher-energy radiation channels, although we note that gamma-ray halos around PWN (see e.g. Aharonian 1995) have been discussed in the recent years which could have a similar physical origin as the escaping outflows considered here. In this regard, extended TeV emission has been recently reported from the PWN in Geminga (Abeysekara et al.

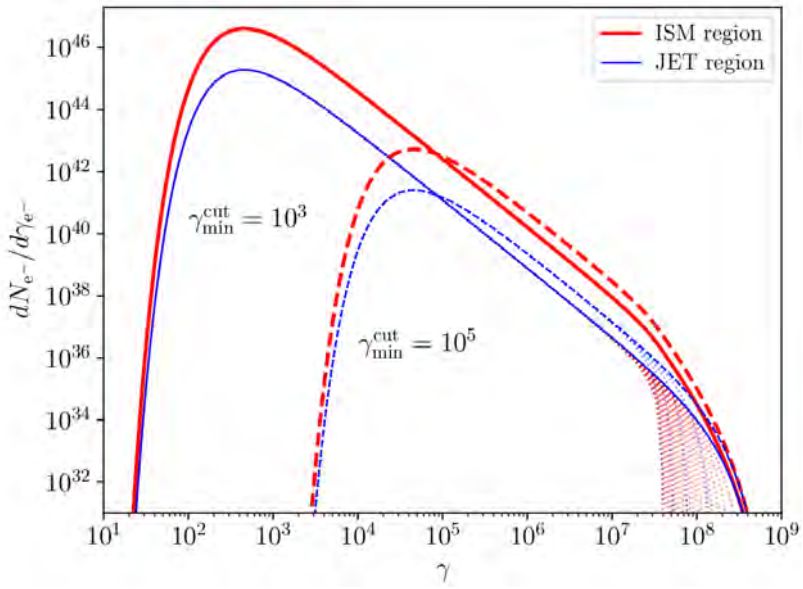

Figure 6.2: Energy distribution of non-thermal particles injected into the JET and ISM regions for different assumed values of the low-energy cutoff $\gamma_{\rm min}^{cut}$. Particle injection is discretized as occurring every $t_{\rm inj} = 1$ kyr (dotted lines). The final cumulative distribution at present time accounts for radiation cooling due to IC on the CMB and synchrotron losses. Distributions are shown for particles injected recently ($t_{\rm inj} \leq 1$ kyr) that diffuse through the JET region (blue lines), and particles injected at $t_{\rm inj} > 1$ kyr diffusing into the ISM region (in red lines). In both cases, a magnetic field of $B_{\rm ISM} = B_{\rm JET} = 5\mu$G is assumed. A low cutoff for the particle distribution at injection is considered, adopting two different values $\gamma_{\rm min}^{cut} = 10^3$ and $\gamma_{\rm min}^{cut} = 10^5$ (solid and dashed lines, respectively). A high energy cutoff $\gamma_{\rm max}^{cut} = 10^8$ is also assumed in all cases. The distribution normalization is computed accounting for the source observed X-ray luminosity (see text for details).

2017), which is consistent with free particle propagation in the ISM (see discussion in Giacinti et al. 2020). Finally, we focus in this study on the outcomes that may be expected particluarly for the case of IGR J11014-6103. A general model extendable to any other BSPWNe is not explored in this paper. We note also that the values adopted for the parameters describing the injected particle distribution can be seen as rather optimistic (e.g. Γ could be harder than the adopted value of 2 and the low-energy cutoff $\gamma_{\rm min}^{\rm cut}$ could be more restrictive than 10^3). These, however, are relatively unconstrained parameters for the case of the source under study. At the same time, the adopted values are such that they can provide estimates of the expected radio emission that can then be contrasted with dedicated observations.

6.3 PREDICTIONS FOR A RADIO-HALO IN IGR J11014-6103

6.3.1 *Injected particle distribution*

The energy distribution of particles injected along IGR J11014-6103's lifetime is shown in Fig. 6.2, which displays the two cases described in Sect. 6.2 for the value of $\gamma_{\rm min} = 10^3$ and 10^5. For the high-energy cutoff, a value of $\gamma_{\rm max}^{\rm cut} = 10^8$ is assumed in the two cases. Particles diffusing through the JET and the ISM regions are shown separately in Fig. 6.2. For the ISM region, individual single-injection events every 1 kyr (dotted lines) are considered. The particles evolve under synchrotron and IC losses while accumulating, forming the final particle distribution (solid lines). The older the injections are, the lower their contribution is at the high-energy end of the final distribution. Freshly accelerated particles are considered only for the JET region (dashed lines in Fig. 6.2).

6.3.2 *Estimated synchrotron fluxes*

The JET and the ISM regions differ in the assumed value for the magnetic field. We used $B_{\rm ISM} = 5\mu$G to compute the synchrotron emission by each injection event and their total final contribution in the ISM. For the JET region, the value of $B_{\rm JET}$ ranges between that of the ISM and the value inferred to produce the observed X-ray emission in the Lighthouse Nebula (for electrons at a maximal energy $\gamma_{\rm max} \approx 10^8$) of $B_{\rm ISM} = 30\mu$G (Pavan et al. 2014). The energy flux of the predicted synchrotron emission is displayed in Fig. 6.3 for the cases $\gamma_{\rm min}^{\rm cut} = 10^3$ and 10^5. Individual contributions and total emission in the ISM are displayed in red with dashed and solid lines, respectively. The energy flux from the JET region is in blue, for five different values of $B_{\rm JET}$: 5, 10, 15, 20 and 30μG.

The radio emission for a low-energy cutoff $\gamma_{\rm min}^{\rm cut} = 10^3$ reaches values of a few $\times 10^{29}$ erg s^{-1}, which should be at levels detectable by existing facilities sensitive in this band. Radio emission is strongly suppressed for $\gamma_{\rm min}^{\rm cut} = 10^5$, which instead provides a larger number of particles at higher energies. Current X-ray satellites can detect the JET region in X-rays even for modest magnetic fields $\sim 15\mu$G. The total radio emission from the ISM region exceeds that of the JET region by a factor 2–10, depending on the value of $B_{\rm JET}$ and the adopted value of $\gamma_{\rm min}$. The JET region is however brighter than any single injection event in the ISM when taking a similar injection time lapse ~ 1 kyr. We include in Fig. 6.3 the observation bands of the radio telescope MeerKAT and the X-ray satellite *Chandra*, noted by orange and green bands, respectively.

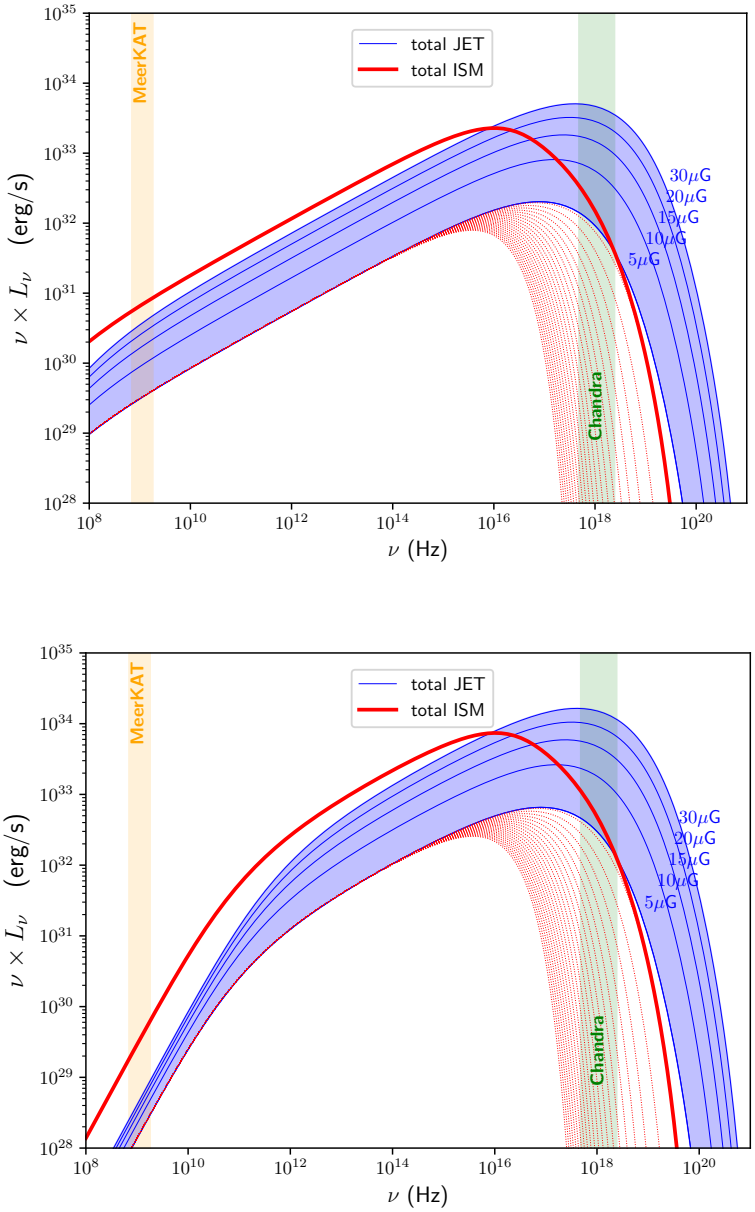

Figure 6.3: **Top**: Spectral energy distribution of the emission produced by electrons injected in the ISM (in red) and JET regions (in blue). A magnetic field $B_{\rm ISM} = 5\mu$G is assumed for the ISM, whereas a range in the value of $B_{\rm JET} = 5, 10, 15, 20$ and 30μG is probed for the JET region. Particle injection is considered up to $t_{\rm inj} = 10^3$ yr for the JET region and from $t_{\rm inj} = 10^3$ yr until $t_{\rm inj} = 20$ kyr for the ISM region (red-dotted lines). Particles are assumed to follow a power-law distribution with a low and a high energy cutoff $\gamma^{cut}_{\rm min} = 10^3$ and $\gamma^{cut}_{\rm max} = 10^8$, respectively. Green and orange vertical bands denote *Chandra* and MeerKAT frequency coverage. **Bottom**: Same as in the left panel but for a particle spectrum with a low-energy cutoff $\gamma^{cut}_{\rm min} = 10^5$.

6.3.3 *Synthetic radio maps*

The cooled particle distribution injected in each event producing the synchrotron emission described above is distributed isotropically from its injection point. The synchrotron maps displayed in Fig. 6.4 reflect this isotropy in the estimated spatial extension of the emission. The injection locations along the pulsar trajectory produce a "trail" of radio emission that is brighter along this direction, whereas the sum of the single events display an overall elliptical geometry encompassing the BSPWNe position. For the JET region, a single injection produces a radially symmetric extended source in our simplified model. In Fig. 6.4 the maps display the angular distribution of the predicted synchrotron fluxes, which has been convolved with the beam of a radio telescope of 15″ × 15″, such as that of the recently operative MeerKAT telescope (Jonas and MeerKAT Team 2016). We report only the case $\gamma_{\rm min}^{\rm cut} = 10^3$ in Fig. 6.4, for which radio emission can reach detectable levels, above ~ 50 μJy beam^{-1}. For $\gamma_{\rm min}^{\rm cut} = 10^5$ radio emission would be undetectable. The spatial distribution in our model provides evidence that the JET region is the brightest spot around IGR J11014-6103, but it is concentrated in a relatively small angular region of a few arcmins. We did not attempt to introduce further complexity with a nonisotropic particle distribution, which may produce extended structures in the radio maps, for example rectilinear jet-like features such as the ones reported in X-rays.

6.4 Discussion on the Lighthouse Nebula

The origin of the extended jet-like features observed in the Lighthouse Nebula and other BSPWNes is unclear. The high velocity of these systems and the apparent rectilinear geometry of their associated outflows, with no appreciable signature of bending as expected due to the ambient medium ram pressure, suggest alternative mechanisms responsible for such jet-like features. Bandiera 2008 proposed a scenario in which the jets could be produced by high-energy electrons escaping the parent PWN and diffusing into the ambient magnetic field. Recent 3D MHD numerical simulations seem to support such a possibility (Barkov et al. 2019a,b; Bucciantini et al. 2020). Here we provide further observational predictions to probe this hypothesis in the context of the Lighthouse Nebula by modeling the radio emission from the immediate surroundings of the source.

The results reported in Sect. 6.3 indicate that, for suitable parameters describing the injected particle energy distributions escaping the BSPWNe, substantial radio emission around IGR J11014-6103 could be produced by these particles when diffusing into the ISM. We note that the value assumed for these parameters (e.g. $\Gamma = 2$ and $\gamma_{\rm min}^{\rm cut} = 10^3$) were chosen so as to account for cases in which detectable radio

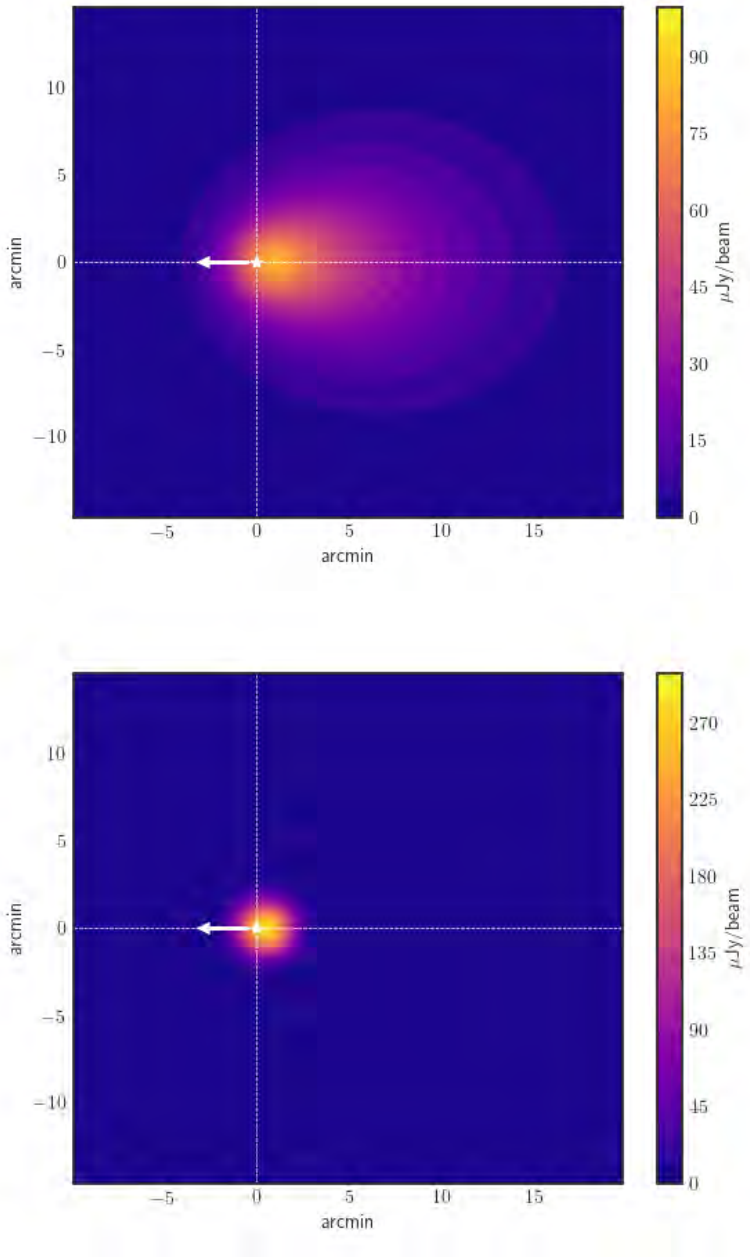

Figure 6.4: Synthetic synchrotron specific flux maps displaying the expected radio emission from IGR J11014-6103 in the 0.9–1.7 GHz band in which MeerKAT operates, convolved with an instrument beam of 15″ × 15″ (Jonas and MeerKAT Team 2016). The contribution from particles injected all along the IGR J11014-6103's lifetime, which escaped the nebula and diffused into the ISM ($B_{\rm ISM} = 5\mu$G), is displayed in the top panel, and that from the JET region ($B_{\rm ISM} = 30\mu$G) is shown in the bottom panel. A white star indicates the position of the pulsar, which is assumed to move leftwards along the horizontal dashed-line.

fluxes may be expected, whereas in others (e.g. $\gamma_{\rm min}^{\rm cut} = 10^5$) such emission would be suppressed. For the former case, the JET region provides the larger contribution, since $B_{\rm JET}$ is larger than $B_{\rm ISM}$. The fact that $B_{\rm JET} > B_{\rm ISM}$ could follow the presence of streaming instabilities generated in the flow of relativistic electrons, generating a turbulent component of the magnetic field responsible for the field amplification, and for the confinement of the radiating electrons themselves (Bykov et al. 2017). The total cumulative radio emission from the more diffuse ISM region, on the other hand, can be a factor of a few to $\sim$20 times higher than that in the JET region. According to our model, observations should therefore reveal a bright concentration toward the jet region, and a broader, dimmer diffuse radio nebular emission surrounding the source.

Compared to the radio emission from the PWN tail reported in (Pavan et al. 2014), the emission from the ISM region in our model displays somewhat softer fluxes. The nebular emission in the ISM region reported here might be intrinsically softer than that within the PWN in IGR J11014-6103. Otherwise, the presence of several populations of accelerated electrons in the PWN particle injection spectrum (see e.g. Atoyan and Aharonian 1996), could also make the radio fluxes harder. For the JET region, although we do not aim to describe the morphological and spectral properties of the extended jet-like features observed in the Lighthouse Nebula in X-rays, our model predicts fluxes compatible with the ones observed at this band, at a level $L_{2-10keV} \gtrsim 10^{33}$ erg s^{-1}, when assuming previously derived values of $B_{\rm JET}$ of a few $\times$ 10 μG (Pavan et al. 2014). At higher energies, in the gamma-ray band, it is worth noting that, given the value of U_{IR} the produced IC gamma-ray luminosity by the electrons responsible for the JET X-rays should be a factor $\sim U_{\rm IR}/(B_{\rm JET}^2/8\pi) \sim 0.3$ times that observed in X-rays, $L_{2-10keV}$.

As stated above the radio emission predicted in our model strongly depends on the assumed limits in the energy distribution of the emitting particles. As displayed in Fig. 6.3, bottom panel, a strong low-energy cutof of $\gamma_{\rm min}^{\rm cut} \gtrsim 10^5$ would render these structures too dim to be detected. On the contrary, the synchrotron radio flux maps displayed in Fig. 6.4 for $\gamma_{\rm min}^{\rm cut} \gtrsim 10^3$ indicate that extended structures should be resolvable by current radio telescopes capable of reaching sensitivities at the level of $\gtrsim 50\mu$Jy/beam. The value of $\gamma_{\rm min}^{\rm cut}$ depends on the mechanisms through which accelerated particles are able to escape the PWN region. For this to occur, the diffusion distance within the bow-shock region should be larger than the shocked wind layer thickness. Given that this is several times smaller than the bow-shock size, the escape energy is just a factor order of 10 smaller than that given by the Hillas limit, which for the Lighthouse Nebula has an associated Lorentz factor of $\gtrsim 10^8$. Nevertheless, particles with lower energies may still be able to escape the PWN along the expanding

PWN tail where the magnetic field density decreases and/or the geometry of the shock interface with the ambient ISM becomes more favorable for electrons to diffuse away. In this regard, it is worth noting that for the case of the Lighthouse Nebula, the base of the main jet-like feature seems to be shifted to a position behind the pulsar with respect to the incoming medium (see e.g. Pavan et al. 2016; see also the inset in Fig. 9 in Kargaltsev et al. 2017), where the PWN conditions could imply lower values for the particles' Lorentz factor to escape the nebula. Alternatively, particle escape can follow magnetic reconnection between the BSPWNe and the ISM magnetic fields (see e.g. Barkov et al. 2019b; Bucciantini et al. 2020), as suggested in the case of the rectilinear structures detected in J1809-1917, for which the gyroradius of the X-ray emitting electrons is by far shorter than the typical size of the nebula (Klingler et al. 2020).

7

DISCUSSION: JETS AND HALOS IN BSPWNE

In this Thesis we have focused on the study of three distinct BSPWNe that display a variety of extended structures in the X-ray band. In the case of PWN J1135-6055, in addition to the pulsar itself, our studies revealed the presence of two jet-like structures and an elongated cometary tail, all of which are presumably powered by the central pulsar. The jets are not symmetric, with the eastern jet being much longer and displaying a rectilinear structure. The western jet, instead, seems to be much more affected by the external ram pressure, given its apparent bent structure. In the next Section we argue that these might by truly pulsar ballistic jets. In the case of PWN B1853+01 the jet-like features are even more striking, as they propagate ahead of the pulsar. Furthermore, the analysis of data obtained with three different X-ray missions suggests the presence of extended X-ray emission surrounding both the PWNe as well as the two newly discovered "antennae"-like structures. As discussed below, this could be a signature of a yet unreported X-ray Halo. Finally, the Lighthouse Nebula displays the longest X-ray jet-like structures ever found in our Galaxy. They have been interpreted as "kinetic jets" produced after high-energy electrons escape the parent PWN (Barkov et al. 2019b). Considering the evolution of these energetic particles due to synchrotron and adiabatic losses, we modeled the putative extended radio emission that could be produced in the surroundings the source. We also provide precise predictions for current radio facilities like MeerKAT, which can be used to constrain the physics behind particle escape in BSPWNe. If such radio structures are detected, they would became radio halos, in analogy to the structures detected at TeV gamma-rays - and in the X-ray band.

7.1 X-RAY JETS IN BSPWNE

About half of the detected X-ray PWNe are BSPWNe (see Table 2.1), amongst which a growing number seem to display jet-like outflows. These jets, however, could be produced in at least two very different scenarios. When the torus/jet morphology was observed in the Crab Nebula (Weisskopf et al. 2000), pulsar jets were understood as the result of magnetic hoop stresses channelling shocked wind towards the rotation axis (Lyubarsky 2002; Komissarov and Lyubarsky 2004). If we take a similar pulsar but with a high proper-motion velocity, the resulting BSPWN will have the termination shock at much closer distances than in the static pulsar case. This shorter distance may

affect the amount of shocked plasma that can be channeled towards the axis, eventually making this mechanism more efficient, resulting in higher-power pulsar jets. Moderately-sized jet structures, possibly bent by the ram pressure of the surrounding medium, have been detected e.g. in Geminga (Posselt et al. 2017), PSR B1929+10(Hui and Becker 2008) and also in one of the BSPWN discussed in this Thesis, PSR J1153+6055 (see Chapter 4).

In this scenario, we argue that BSPWN could display intrinsically more powerful jets than low-velocity systems. These jets, however, are still "ballistic" jets, and therefore susceptible to be deflected by the medium at some relatively short distances, e.g. forming the arc-shaped structures observed in Geminga (Pavlov et al. 2006) or PSR J1153+6055 (see Fig. 4.1). The cometary tail trailing the pulsar motion in these systems, on the other hand, may correspond to a motion-distorted torus like those observed in slow-moving pulsars like the Crab. As for the asymmetric brightness profiles observed in the eastern/western outflows, as discussed in Sect. 4.4, this could be due different direction of propagation, relative kinetic power, or properties of the surrounding ISM. This would also be in accordance to recent numerical simulations of fast-moving PWNe (Barkov et al. 2019b).

Other large-scale X-ray outflows detected in a number of BSPWN are instead difficult to interpret as ballistic jets, like in the Guitar Nebula (Hui and Becker 2007; Wang 2021), the Lighthouse nebula (Pavan et al. 2014, 2016), PWN J2030+4415 (de Vries and Romani 2022), PWN J1509-5850 (Klingler et al. 2016a), PWN B0355+54(Klingler et al. 2016b), the Snail Nebula (Temim et al. 2009, 2015), or one of the sources discussed in this Thesis, PWN B1853+01 (see Chapter 5). These non-bent, "go-straight-ahead" jet-like features may be produced by high-energy particles that escaped the PWN through reconnected magnetic field lines, emitting synchrotron emission that traces the ISM magnetic field. As originally proposed in Bandiera 2008, the gyro-radii of these highly energetic electrons can be comparable or exceed the stand-off distance of the bow shock. Electrons emitting synchrotron radiation at 1 keV in a ~ 20 μG magnetic field have Lorentz factors $\gamma \sim 10^8 (E/1 \text{ keV})^{1/2} (B/20\ \mu\text{G})^{-1/2}$. They will be able to escape the parent PWN if the bow-shock is shorter than their gyro-radii, $r_g \sim 10^{14} (E/1 \text{ keV})^{1/2} (B/20\ \mu\text{G})^{-3/2}$ cm. This particle leakage may be powered/enhanced by the action of magnetic reconnection (see Sect 2.3). This scenario is supported by recent 3D MHD simulations (Barkov et al. 2019b; Olmi and Bucciantini 2019b), which demonstrate that the geometry of the magnetic field structures both within the PWN and in the surrounding ISM can drastically affect the formation of large-scale outflows. In addition, these simulations convincingly explain the asymmetries found in between jets and counter-jets, e.g. like those observed in the Lighthouse Nebula.

The misaligned outflows observed in these sources, on the other hand, display relatively hard spectra in the 0.5–8 keV band ($\Gamma_{B2245} = 1.14^{+0.34}_{-0.31}$, $\Gamma_{J1101} = 1.7 \pm 0.1$, $\Gamma_{J2030} = 1.18 \pm 0.20$, $\Gamma_{J1509} = 1.50 \pm 0.20$, $\Gamma_{B0355} = 1.60^{+0.32}_{-0.29}$). This could be again a fingerprint of the energy-selection process leading to the formation of such structures in a partcile-escape scenario. The spectral analysis of the antennae-like structures discussed in Sect. 5.3 reveals indeed a significantly harder emission in these outflows compared to that found in the compact nebula and tail regions. Furthermore, the *NuSTAR* results obtained in the case of PWN B1853+01 suggest that emission from these antennae can extend up to tens of keV, with no apparent signatures of spectral breaks. Similarly hard X-ray emission has been reported for the Lighthouse Nebula using dedicated *NuSTAR* observations of that source (Klingler et al. 2023).

It is worth mentioning that, apart from jets and antennae found in BSPWNe, a number of long X-ray filaments have also been detected e.g. in the Galactic Center region, as revealed by *Chandra* and *XMM-Newton* (see e.g. Johnson et al. 2009; Wang et al. 2002). Interestingly, such filamentary structures are also observed in the radio band (see e.g. the recent results reported by MeerKAT, Heywood et al. 2022). It has been suggested that these narrow filaments near the Galactic Centre could be streams of high-energy particles escaping yet unidentified PWNe, and could represent the low-frequency analogues of misaligned outflows seen in X-rays (Barkov and Lyutikov 2019).

7.2 HALOS IN BSPWNE

While the jet-like outflows in BSPWNe observed in X-rays can be explained as the signatures of particles escaping the bow shock into the surrounding medium, an increasing number of PWNe have been detected in the last years which display extended emission in the TeV energy range that goes beyond the limits of the PWN itself. This has been considered to be a new class of TeV sources, dubbed "TeV halos", which could be responsible for a significant fraction of the electronic component of Galactic cosmic-rays (Linden et al. 2017; Sudoh et al. 2019). These TeV halos are thought to be produced by relativistic electrons/positrons that have escaped from the PWN and, while diffusing through the ISM, they up-scatter the local photon-field, e.g. the cosmic microwave background or the interstellar infrared radiation field, to produce the observed TeV emission through IC processes. This diffusion process, however, cannot be very effective: fitting the averaged flux profiles of these halo structures with an isotropic diffusion model requires a diffusion coefficient significantly lower than the local cosmic ray diffusion coefficient (Abeysekara et al. 2017). This low-diffusion regime can be explained if magnetic amplification is taking place in the regions surrounding the PWN. In this regard, particle escape models

already require a relatively high magnetic field strength in the nearby ISM. Moreover, as in the presence of a net current, the magnetic field can be amplified much more efficiently than for a neutral flow (see e.g. Bell 2004).

There is also a strong debate related to the physics of PWN evolution and the formation of TeV halos. As mentioned in Chapter2 (see Sect 2.5), middle-aged PWN can be affected by the SNR reverse shock, which can partially crush and/or disrupt the PWN (see Fig. 2.12), as discussed in Giacinti et al. 2020. At this stage, high-energy particles can escape the PWN and travel through the shocked SNR plasma, and eventually reach the ambient ISM. Halo structures however are defined in this context when the central pulsar no longer dominates the dynamics of system which means the pulsar/PWN has escaped the parent SNR or the parent SNR has already dissolved. On the contrary, less-restrictive definitions of TeV halos have also been proposed. In Linden et al. 2017 and Sudoh et al. 2019, for instance, a TeV halo is formed if the diffusion is the dominant transport mechanism of electron/positron that escaped the parent PWN.

The analysis of PWN B1853+01 reported in this Thesis (Chapter 5) may actually correspond to the situation in which the reverse shock of the W44 SNR is strongly affecting the BSPWN structure. A similar scenario has also been proposed for at least another BSPWN, the Snail Nebula(Temim et al. 2009, 2015). In both cases, in addition to the antennae like structures, X-ray emission is observed to extend much beyond the PWN compact nebula and tail regions (as well as around the antennae structures themselves). We interpret this extended X-ray emission as a "proper" X-ray halo. As discussed Linden et al. 2017), the physical mechanisms behind the production of TeV halos should actually naturally lead to the formation of similar structures in the X-ray band. In this regard, using test-particle simulations in an isotropic Kolmogorov turbulent field, Giacinti et al. 2012 demonstrated that in the process in which cosmic rays diffuse away from their sources, before they have diffused over several correlation lengths of the large-scale field, the transport can be highly filamentary due to the anisotropic nature of particle diffusion in magnetised plasmas (see e.g. Isenberg and Jokipii 1979). Furthermore, Giacalone 2017 has shown that similar filaments may also develop on smaller scales close to the shock, for a given field realization. In this context, the antennae-like structures observed in PWN B1853+01 and in the Snail Nebula could represent these filamentary structures, while further diffusion of electrons into the complex SNR reverse-shocked medium would then be responsible for the extended halo-like emission surrounding the whole system.

The relative intensity of such X-ray halo with respect to the TeV halo observed at gamma-ray energies will depend on the ratio between the energy density of the local photon field and the magnetic field

density (Aharonian et al. 1997). For particles with energies beyond a few tens of TeV, the upscattering of the CMB will dominate, since IC on the IR radiation field would be highly suppressed by Klein-Nishina effects (see Sect. 2.4). Typical values for the magnetic field in the ISM is at the level of $\sim 10\mu$G, corresponding to an energy density of about 0.20 eV cm^3. This is comparable to the CMB energy density, ~ 0.26 eV/cm^3. Therefore, for electrons/positrons with multi-TeV energies the pulsar halo's fluxes at $\sim$10 TeV and at $\sim 1keV$ are supposed to be comparable. With fluxes from TeV halos observed in the VHE gamma-ray band range from $\sim 5 \times 10^{-13}$ erg cm^{-2}s^{-1} to $\sim 5 \times 10^{-12}$ erg cm^{-2}s^{-1}, the X-ray counterpart, assuming such a $\sim 10\ \mu$G, should be expected to reach $\sim 2 \times 10^{-12}$erg cm^{-2}s^{-1} in the 0.5-2 keV band. Therefore, both TeV and X-ray energy band can provide direct information about current particle acceleration and transportation mechanisms around BSPWNe. Furthermore, escaped electrons will eventually cool down due adiabatic as well as IC and synchrotron losses. These particles will then radiate at lower-energies, e.g. in the radio band. We addresses such a putative radio halo counterpart in the case of the Lighthouse Nebula (see Chapter 6). Although in this Thesis we have modelled such extended radio emission only for this system, we note that other BSPWNe may also display extended radio emission from electrons escaping their nebulae.

In the recent years, the number of TeV halo candidates has increased significantly. In particular, the exploration of the gamma-ray sky at ultra-high energies with the LHAASO observatory (Cao et al. 2019) has led to the identification of dozens of such TeV halo candidates (Cao et al. 2024). The X-ray follow-up of these newly discovered systems can be crucial to understand their nature, as X-ray instruments provide better sensitivity and angular resolution than Cherenkov arrays to constrain the flux and morphological properties of these sources. Reversely, the search for extended TeV emission from BSPWN displaying particle-escape signatures using Imaging Cherenkov telescopes did not report a positive result in the case of PSR J0357+3205, PSR J1740+1000 or PSR B0355+54 (Benbow et al. 2021). For this latter two sources, however, recent observations at TeV energies with water-Cherenkov telescopes have resulted in the detection of large-scale VHE gamma-ray emission possibly associated to a TeV halo structure (Albert et al. 2023; Cao et al. 2024). Furthermore, in the case of the Snail Nebula displaying both antennae-like structures and possibly an X-ray halo surrounding the PWN, extended TeV emission has been detected with the H.E.S.S. array (Acero 2011). For the morphologycally similar BSPWN studied in this Thesis, PWN B1853+01, the MAGIC collaboration reported recently the search for TeV gamma-ray emission from the surrounding W44(di Tria et al. 2022). No significant TeV emission could be found, although these MAGIC observations were focused on the northern regions of the SNR, from which HE gamma-rays possibly produced by the

escape of SNR-accelerated cosmic-rays has been detected (Uchiyama et al. 2012). Future observations in the VHE gamma-ray band with next-generation instruments like the Cherenkov Telescope Array will provide conclusive constraints on the putative TeV counterpart of extended emission in BSPWNe.

8

CONCLUSIONS AND FUTURE WORK

In this Thesis we have presented the results of the analysis of X-ray observations of the three BSPWN PWN J1135-6055, PWN B1853+01 and IGR J11014-6103, that display signatures of escaping particles from the PWNe. We have argued that the jet-like structures in the first one can be explained as powerful jets produced in the pulsar vicinity due to the distorted shape of the PWN owing to the large proper-motion of the system. In the case of PWN B1853+01, we discuss the antennae-like morphology in the context of particle escape from the PWN followed by emission in the magnetic field of the surrounding ISM. In addition, we interpreted the diffuse, extended emission around this source as a potential X-ray halo. We have also provided estimations for the existence of a low-energy radio counterpart in the case of IGR J11014-6103, which can be tested with current high-sensitivity instrumentation operating at these energies like MeerKAT. All together, our studies provide further evidences and observational tests to probe particle acceleration, escape and emission processes taking place in BSPWN. Additionally, we argue that the extended X-ray emission observed in these sources can have counterparts at both lower (radio) and higher (gamma-ray) energies.

The detection of extended, faint X-ray halos in other similar systems can be in general challenging for pointing X-ray instruments like XMM-*Newton*, *Chandra* or *NuSTAR*. In this regard, the sky-scanning satellite eROSITA (the extended ROentgen Survey with an Imaging Telescope Array), sensitive to X-rays in the energy range of 0.3–11 keV and featuring a wide field of view of $\sim 0.8^{\circ}$, would be an excellent instrument to search for such X-ray halos. Deep observation of PWNe with good angular resolution instruments are on the other hand crucial to study the jet-like filamentary structures detected in a growing number of BSPWNe. Next generation instruments like *Athena* could allow for more accurate spatially resolved spectral measurements of these structures, providing new insights to study particle-escape mechanisms and subsequent diffusion in and around BSPWNe. In the gamma-ray domain, water-Cherenkov telescopes like the LHAASO array hold the promise to detect tens of new TeV halos in our Galaxy in the next few years. Future imaging Cherenkov facilities like the Cherenkov Telescope Array Observatory CTAO have the potential to further constraint the spectral and morphological properties of this new class of VHE emitters thanks to the improvement in both sensitivity and angular resolution with respect to current instruments.

BIBLIOGRAPHY

Abeysekara, A. U. et al. (2017). "Extended gamma-ray sources around pulsars constrain the origin of the positron flux at Earth." In: *Science* 358.6365, pp. 911–914.

Acero, F. (2011). "Detection of TeV emission from the intriguing composite SNR G327.1-1.1." In: *International Cosmic Ray Conference*. Vol. 7. International Cosmic Ray Conference, p. 185.

Achterberg, A. et al. (2001). "Particle acceleration by ultrarelativistic shocks: theory and simulations." In: *MNRAS* 328.2, pp. 393–408.

Aharonian, F. A. (1995). "Very high energy gamma-ray astronomy and the origin of cosmic rays." In: *Nuclear Physics B Proceedings Supplements* 39.1, pp. 193–206.

Aharonian, F. A., A. M. Atoyan, and T. Kifune (1997). "Inverse Compton gamma radiation of faint synchrotron X-ray nebulae around pulsars." In: *MNRAS* 291.1, pp. 162–176.

Aharonian, F. A., S. R. Kelner, and A. Y. Prosekin (2010). "Angular, spectral, and time distributions of highest energy protons and associated secondary gamma rays and neutrinos propagating through extragalactic magnetic and radiation fields." In: *Phys. Rev. D* 82.4, 043002, p. 043002.

Aharonian, F. et al. (2006). "Observations of the Crab nebula with HESS." In: *A&A* 457.3, pp. 899–915.

Aharonian, F. et al. (2021). "Extended Very-High-Energy Gamma-Ray Emission Surrounding PSR J 0622 +3749 Observed by LHAASO-KM2A." In: *Phys. Rev. Lett.* 126.24, 241103, p. 241103.

Albert, A. et al. (2023). "HAWC Detection of a TeV Halo Candidate Surrounding a Radio-quiet Pulsar." In: *ApJ* 944.2, L29, p. L29.

Amato, E. (2024). "Particle acceleration in pulsars and pulsar wind nebulae." In: *arXiv e-prints*, arXiv:2402.10912, arXiv:2402.10912.

Arnaud, K. A. (1996). "XSPEC: The First Ten Years." In: *Astronomical Data Analysis Software and Systems V*. Ed. by G. H. Jacoby and J. Barnes. Vol. 101. Astronomical Society of the Pacific Conference Series, p. 17.

Arons, J. and E. T. Scharlemann (1979). "Pair formation above pulsar polar caps: structure of the low altitude acceleration zone." In: *ApJ* 231, pp. 854–879.

Atoyan, A. M. and F. A. Aharonian (1996). "On the mechanisms of gamma radiation in the Crab Nebula." In: *MNRAS* 278.2, pp. 525–541.

Axford, W. I., E. Leer, and G. Skadron (1977). "The Acceleration of Cosmic Rays by Shock Waves." In: *International Cosmic Ray Conference*. Vol. 11. International Cosmic Ray Conference, p. 132.

Baade, W. and F. Zwicky (1934). "Remarks on Super-Novae and Cosmic Rays." In: *Physical Review* 46.1, pp. 76–77.

Bamba, A. and B. J. Williams (2022). "Supernova Remnants: Types and Evolution." In: *Handbook of X-ray and Gamma-ray Astrophysics*, 77, p. 77.

Bandiera, R. (2008). "On the X-ray feature associated with the Guitar nebula." In: *A&A* 490.1, pp. L3–L6.

Barkov, M. V. and M. Lyutikov (2019). "On the nature of radio filaments near the Galactic Centre." In: *MNRAS* 489.1, pp. L28–L31.

Barkov, M. V., M. Lyutikov, and D. Khangulyan (2019a). "3D dynamics and morphology of bow-shock pulsar wind nebulae." In: *MNRAS* 484.4, pp. 4760–4784.

Barkov, M. V. et al. (2019b). "Kinetic 'jets' from fast-moving pulsars." In: *MNRAS* 485.2, pp. 2041–2053.

Bell, A. R. (1978). "The acceleration of cosmic rays in shock fronts - I." In: *MNRAS* 182, pp. 147–156.

Bell, A. R. (2004). "Turbulent amplification of magnetic field and diffusive shock acceleration of cosmic rays." In: *MNRAS* 353.2, pp. 550–558.

Benbow, W. et al. (2021). "A Search for TeV Gamma-Ray Emission from Pulsar Tails by VERITAS." In: *ApJ* 916.2, 117, p. 117.

Blandford, R. D. and J. P. Ostriker (1978). "Particle acceleration by astrophysical shocks." In: *ApJ* 221, pp. L29–L32.

Bogovalov, S. V. (1999). "On the physics of cold MHD winds from oblique rotators." In: *A&A* 349, pp. 1017–1026.

Bordas, P. et al. (2021). "Signatures of extended radio emission from escaping electrons in the Lighthouse Nebula." In: *A&A* 654, A4, A4.

Bosch-Ramon, V. (2008). "The physics of non-thermal radiation in microquasars." In: *arXiv e-prints*, arXiv:0805.1707, arXiv:0805.1707.

Brisbois, C. et al. (2018). "HAWC detection of TeV source HAWC J0635+070." In: *The Astronomer's Telegram* 12013, p. 1.

Bucciantini, N. (2002). "Pulsar bow-shock nebulae. II. Hydrodynamical simulation." In: *A&A* 387, pp. 1066–1073.

Bucciantini, N. (2018). "Escape of high-energy particles from bow-shock pulsar wind nebulae." In: *MNRAS* 480.4, pp. 5419–5426.

Bucciantini, N. and R. Bandiera (2001). "Pulsar bow-shock nebulae. I. Physical regimes and detectability conditions." In: *A&A* 375, pp. 1032–1039.

Bucciantini, N., B. Olmi, and L. Del Zanna (2020). "3D Relativistic MHD Simulations of Pulsar Bow Shock Nebulae." In: *Journal of Physics Conference Series*. Vol. 1623. Journal of Physics Conference Series. IOP, 012002, p. 012002.

Burrows, D. N. (2021). *The WSPC Handbook of Astronomical Instrumentation, Volume 4: X-Ray Astronomical Instrumentation*.

Bykov, A. M. et al. (2017). "Pulsar Wind Nebulae with Bow Shocks: Non-thermal Radiation and Cosmic Ray Leptons." In: *Space Sci. Rev.* 207.1-4, pp. 235–290.

Cao, Z. et al. (2019). "The Large High Altitude Air Shower Observatory (LHAASO) Science Book (2021 Edition)." In: *arXiv e-prints*, arXiv:1905.02773, arXiv:1905.02773.

Cao, Z. et al. (2024). "The First LHAASO Catalog of Gamma-Ray Sources." In: *ApJS* 271.1, 25, p. 25.

Caprioli, D. and A. Spitkovsky (2014). "Simulations of Ion Acceleration at Non-relativistic Shocks. III. Particle Diffusion." In: *ApJ* 794.1, 47, p. 47.

Caswell, J. L. et al. (1975). "Neutral hydrogen absorption measurements yielding kinematic distances for 42 continuum sources in the galactic plane." In: *A&A* 45, pp. 239–258.

Cerutti, B. et al. (2013). "Simulations of Particle Acceleration beyond the Classical Synchrotron Burnoff Limit in Magnetic Reconnection: An Explanation of the Crab Flares." In: *ApJ* 770.2, 147, p. 147.

Chevalier, R. A. (1977). "Was SN 1054 A Type II Supernova?" In: *Supernovae*. Ed. by D. N. Schramm. Vol. 66. Astrophysics and Space Science Library, p. 53.

Chevalier, R. A. (1998). "Pulsar nebulae in supernovae." In: *Mem. Soc. Astron. Italiana* 69, pp. 977–987.

Clark, D. H., A. J. Green, and J. L. Caswell (1975). "Improved 408 MHz Observations of Some Galactic Supernova Remnants." In: *Australian Journal of Physics Astrophysical Supplement* 37, pp. 75–86.

Claussen, M. J. et al. (1997). "Polarization Observations of 1720 MHz OH Masers toward the Three Supernova Remnants W28, W44, and IC 443." In: *ApJ* 489.1, pp. 143–159.

Condon, J. J. and S. M. Ransom (2016). *Essential Radio Astronomy*.

Coroniti, F. V. (1990). "Magnetically Striped Relativistic Magnetohydrodynamic Winds: The Crab Nebula Revisited." In: *ApJ* 349, p. 538.

Cox, D. P. (1972). "Cooling and Evolution of a Supernova Remnant." In: *ApJ* 178, pp. 159–168.

Del Zanna, L., E. Amato, and N. Bucciantini (2004). "Axially symmetric relativistic MHD simulations of Pulsar Wind Nebulae in Supernova Remnants. On the origin of torus and jet-like features." In: *A&A* 421, pp. 1063–1073.

Ebeling, H. and G. Wiedenmann (1993). "Detecting structure in two dimensions combining Voronoi tessellation and percolation." In: *PRE* 47.1, pp. 704–710.

Fermi, E. (1949). "On the Origin of the Cosmic Radiation." In: *Physical Review* 75.8, pp. 1169–1174.

Ferrand, G. and S. Safi-Harb (2012). "A census of high-energy observations of Galactic supernova remnants." In: *Advances in Space Research* 49.9, pp. 1313–1319.

Frail, D. A., N. E. Kassim, and K. W. Weiler (1994). "Radio Imaging of two Supernova Remnants Containing Pulsars." In: *AJ* 107, p. 1120.

Frail, D. A. et al. (1996). "The Pulsar Wind Nebula around PSR B1853+01 in the Supernova Remnant W44." In: *ApJ* 464, p. L165.

Fruscione, A. et al. (2006). "CIAO: Chandra's data analysis system." In: *Observatory Operations: Strategies, Processes, and Systems*. Ed. by D. R. Silva and R. E. Doxsey. Vol. 6270. Society of Photo-Optical Instrumentation Engineers (SPIE) Conference Series, 62701V, p. 62701V.

Gabici, S., F. A. Aharonian, and P. Blasi (2007). "Gamma rays from molecular clouds." In: *Ap&SS* 309.1-4, pp. 365–371.

Gaensler, B. M. et al. (2004). "The Mouse that Soared: High-Resolution X-Ray Imaging of the Pulsar-powered Bow Shock G359.23-0.82." In: *ApJ* 616.1, pp. 383–402.

Gaensler, B. M. and P. O. Slane (2006). "The Evolution and Structure of Pulsar Wind Nebulae." In: *ARA&A* 44.1, pp. 17–47.

García, F. et al. (2012). "On the origin of the jet-like radio/X-ray morphology of G290.1-0.8." In: *A&A* 546, A91, A91.

Giacalone, J. (2017). "The Acceleration of Charged Particles at a Spherical Shock Moving through an Irregular Magnetic Field." In: *ApJ* 848.2, 123, p. 123.

Giacinti, G., M. Kachelrieß, and D. V. Semikoz (2012). "Filamentary Diffusion of Cosmic Rays on Small Scales." In: *Phys. Rev. Lett.* 108.26, 261101, p. 261101.

Giacinti, G. et al. (2020). "Halo fraction in TeV-bright pulsar wind nebulae." In: *A&A* 636, A113, A113.

Ginzburg, V. L. and S. I. Syrovatskii (1964). *The Origin of Cosmic Rays*.

Gold, T. (1968). "Rotating Neutron Stars as the Origin of the Pulsating Radio Sources." In: *Nature* 218.5143, pp. 731–732.

Gold, T. (1969). "Rotating Neutron Stars and the Nature of Pulsars." In: *Nature* 221.5175, pp. 25–27.

Goldreich, P. and W. H. Julian (1969). "Pulsar Electrodynamics." In: *ApJ* 157, p. 869.

H. E. S. S. Collaboration et al. (2018). "The H.E.S.S. Galactic plane survey." In: *A&A* 612, A1, A1.

Halpern, J. P. et al. (2014). "Discovery of X-Ray Pulsations from the INTEGRAL Source IGR J11014-6103." In: *ApJ* 795.2, L27, p. L27.

Harrison, F. A. et al. (2013). "The Nuclear Spectroscopic Telescope Array (NuSTAR) High-energy X-Ray Mission." In: *ApJ* 770.2, 103, p. 103.

Harrus, I. et al. (2006). "XMM-Newton Analysis of the Supernova Remnant W44." In: *The X-ray Universe 2005*. Ed. by A. Wilson. Vol. 604. ESA Special Publication, p. 369.

Harrus, I. M., J. P. Hughes, and D. J. Helfand (1996). "Discovery of an X-Ray Synchrotron Nebula Associated with the Radio Pulsar PSR B1853+01 in the Supernova Remnant W44." In: *ApJ* 464, p. L161.

Hester, J. J. (2008). "The Crab Nebula : an astrophysical chimera." In: *ARA&A* 46, pp. 127–155.

Hewish, A. et al. (1968). "Observation of a Rapidly Pulsating Radio Source." In: *Nature* 217.5130, pp. 709–713.

Heywood, I. et al. (2022). "The 1.28 GHz MeerKAT Galactic Center Mosaic." In: *ApJ* 925.2, 165, p. 165.

Hobbs, G. et al. (2005). "A statistical study of 233 pulsar proper motions." In: *MNRAS* 360.3, pp. 974–992.

Hui, C. Y. and W. Becker (2007). "X-ray emission properties of the old pulsar PSR B2224+65." In: *A&A* 467.3, pp. 1209–1214.

Hui, C. Y. and W. Becker (2008). "Resolving the bow-shock nebula around the old pulsar PSR B1929+10 with multi-epoch Chandra observations." In: *A&A* 486.2, pp. 485–491.

Hui, C. Y. et al. (2012). "XMM-Newton Observation of PSR B2224+65 and Its Jet." In: *ApJ* 747.1, 74, p. 74.

Isenberg, P. A. and J. R. Jokipii (1979). "Gradient and curvature drifts in magnetic fields with arbitrary spatial variation." In: *ApJ* 234, pp. 746–752.

Johnson, S. P., H. Dong, and Q. D. Wang (2009). "A large-scale survey of X-ray filaments in the Galactic Centre." In: *MNRAS* 399.3, pp. 1429–1440.

Jonas, J. and MeerKAT Team (2016). "The MeerKAT Radio Telescope." In: *MeerKAT Science: On the Pathway to the SKA*, 1, p. 1.

Jones, L. R., A. Smith, and L. Angelini (1993). "A detailed X-ray and radio study of the supernova remnant W 44." In: *MNRAS* 265, pp. 631–640.

Kargaltsev, O. and G. G. Pavlov (2008). "Pulsar Wind Nebulae in the Chandra Era." In: *40 Years of Pulsars: Millisecond Pulsars, Magnetars and More*. Ed. by C. Bassa et al. Vol. 983. American Institute of Physics Conference Series, pp. 171–185.

Kargaltsev, O. et al. (2017). "Pulsar wind nebulae created by fast-moving pulsars." In: *Journal of Plasma Physics* 83.5, 635830501, p. 635830501.

Kaspi, V. M. et al. (2001). "X-Ray Detection of Pulsar PSR B1757-24 and Its Nebular Tail." In: *ApJ* 562.2, pp. L163–L166.

Kaspi, V. M., M. S. E. Roberts, and A. K. Harding (2006). "Isolated neutron stars." In: *Compact stellar X-ray sources*. Vol. 39, pp. 279–339.

Kennel, C. F. and F. V. Coroniti (1984a). "Confinement of the Crab pulsar's wind by its supernova remnant." In: *ApJ* 283, pp. 694–709.

Kennel, C. F. and F. V. Coroniti (1984b). "Magnetohydrodynamic model of Crab nebula radiation." In: *ApJ* 283, pp. 710–730.

Kennel, C. F., F. S. Fujimura, and R. Pellat (1979). "Pulsar Magnetospheres." In: *Space Sci. Rev.* 24.4, pp. 407–436.

Kirk, J. G. and D. Y. Lyubarsky (2001). "Reconnection in Pulsar Winds." In: *PASA* 18.4, pp. 415–420.

Kirk, J. G. et al. (2000). "Particle Acceleration at Ultrarelativistic Shocks: An Eigenfunction Method." In: *ApJ* 542.1, pp. 235–242.

Kirk, J. G., Y. Lyubarsky, and J. Petri (2009). "The Theory of Pulsar Winds and Nebulae." In: *Astrophysics and Space Science Library*. Ed. by W. Becker. Vol. 357. Astrophysics and Space Science Library, p. 421.

Klingler, N. et al. (2016a). "Chandra Observations of Outflows from PSR J1509-5850." In: *ApJ* 828.2, 70, p. 70.

Klingler, N. et al. (2016b). "Deep Chandra Observations of the Pulsar Wind Nebula Created by PSR B0355+54." In: *ApJ* 833.2, 253, p. 253.

Klingler, N. et al. (2020). "Chandra Monitoring of the J1809-1917 Pulsar Wind Nebula and Its Field." In: *ApJ* 901.2, 157, p. 157.

Klingler, N. et al. (2023). "A NuSTAR and Chandra Investigation of the Misaligned Outflow of PSR J1101–6101 and the Lighthouse Pulsar Wind Nebula." In: *The Astrophysical Journal* 950.2, p. 177.

Komissarov, S. S. and Y. E. Lyubarsky (2004). "Synchrotron nebulae created by anisotropic magnetized pulsar winds." In: *MNRAS* 349.3, pp. 779–792.

LHAASO Collaboration et al. (2021). "Peta-electron volt gamma-ray emission from the Crab Nebula." In: *Science* 373, pp. 425–430.

Landau, L. D. and E. M. Lifshitz (1975). *The classical theory of fields*.

Linden, T. et al. (2017). "Using HAWC to discover invisible pulsars." In: *Phys. Rev. D* 96.10, 103016, p. 103016.

Longair, M. S. (2011). *High Energy Astrophysics*.

López-Coto, R. et al. (2022). "Gamma-ray haloes around pulsars as the key to understanding cosmic-ray transport in the Galaxy." In: *Nature Astronomy* 6, pp. 199–206.

Lovelace, R. V. E., J. M. Sutton, and H. D. Craft (1968). "Pulsar NP 0532 Near Crab Nebula." In: *IAU Circ.* 2113, p. 1.

Lyubarsky, Y. E. (2002). "On the structure of the inner Crab Nebula." In: *MNRAS* 329.2, pp. L34–L36.

Lyubarsky, Y. E. (2003). "The termination shock in a striped pulsar wind." In: *MNRAS* 345.1, pp. 153–160.

Lyubarsky, Y. and J. G. Kirk (2001). "Reconnection in a Striped Pulsar Wind." In: *ApJ* 547.1, pp. 437–448.

Manchester, R. N. (2004). "Observational Properties of Pulsars." In: *Science* 304.5670, pp. 542–547.

Manchester, R. N. et al. (1991). "PSR 1758-24 and G 5.4-1.2, a remarkable pulsar-supernova remnant association." In: *MNRAS* 253, 7P.

Marelli, M. (2012). "The X-ray behaviour of Fermi/LAT pulsars." In: *arXiv e-prints*, arXiv:1205.1748, arXiv:1205.1748.

Matheson, H. and S. Safi-Harb (2010). "The Plerionic Supernova Remnant G21.5-0.9 Powered by PSR J1833-1034: New Spectroscopic and Imaging Results Revealed with the Chandra X-ray Observatory." In: *ApJ* 724.1, pp. 572–587.

Mayall, N. U. (1939). "The Crab Nebula, a Probable Supernova." In: *Leaflet of the Astronomical Society of the Pacific* 3.119, p. 145.

Mayall, N. U. and J. H. Oort (1942). "Further Data Bearing on the Identification of the Crab Nebula with the Supernova of 1054 A.D. Part II. The Astronomical Aspects." In: *PASP* 54.318, pp. 95–104.

MeerKAT Collaboration (2018). "News Note: MeerKAT Radio Telescope Inaugurated/ Clearest image of the Centre of the Milky Way." In: *Monthly Notes of the Astronomical Society of South Africa* 77.8, pp. 102–103.

Michel, F. C. (1971). "Coherent Neutral Sheet Radiation from Pulsars." In: *Comments on Astrophysics and Space Physics* 3, p. 80.

Michel, F. C. (1994). "Magnetic Structure of Pulsar Winds." In: *ApJ* 431, p. 397.

Nobukawa, K. K. et al. (2018). "Evidence for a Neutral Iron Line Generated by MeV Protons from Supernova Remnants Interacting with Molecular Clouds." In: *ApJ* 854.2, 87, p. 87.

Okon, H. et al. (2020). "Deep XMM-Newton Observations Reveal the Origin of Recombining Plasma in the Supernova Remnant W44." In: *ApJ* 890.1, 62, p. 62.

Olmi, B. and N. Bucciantini (2019a). "Full-3D relativistic MHD simulations of bow shock pulsar wind nebulae: emission and polarization." In: *MNRAS* 488.4, pp. 5690–5701.

Olmi, B. and N. Bucciantini (2019b). "On the origin of jet-like features in bow shock pulsar wind nebulae." In: *MNRAS* 490.3, pp. 3608–3615.

Olmi, B. and N. Bucciantini (2023). "The Dawes Review 11: From young to old: The evolutionary path of Pulsar Wind Nebulae." In: *PASA* 40, e007, e007.

Pacholczyk, A. G. (1970). *Radio astrophysics. Nonthermal processes in galactic and extragalactic sources*.

Pacini, F. (1967). "Energy Emission from a Neutron Star." In: *Nature* 216.5115, pp. 567–568.

Padmanabhan, T. (2000). *Theoretical Astrophysics: Volume 2, Stars and Stellar Systems*. Theoretical Astrophysics. Cambridge University Press.

Pavan, L. et al. (2014). "The long helical jet of the Lighthouse nebula, IGR J11014-6103." In: *A&A* 562, A122, A122.

Pavan, L. et al. (2016). "Closer view of the IGR J11014-6103 outflows." In: *A&A* 591, A91, A91.

Pavlov, G. G., D. Sanwal, and V. E. Zavlin (2006). "The Pulsar Wind Nebula of the Geminga Pulsar." In: *ApJ* 643.2, pp. 1146–1150.

Peron, G. et al. (2020). "On the Gamma-Ray Emission of W44 and Its Surroundings." In: *ApJ* 896.2, L23, p. L23.

Petre, R., K. D. Kuntz, and R. L. Shelton (2002). "The X-Ray Structure and Spectrum of the Pulsar Wind Nebula Surrounding PSR B1853+01 in W44." In: *ApJ* 579.1, pp. 404–410.

Petre, R. and P. J. Serlemitsos (1985). "Conical imaging mirrors for high-speed x-ray telescopes." In: *Appl. Opt.* 24.12, pp. 1833–1837.

Pétri, J. and Y. Lyubarsky (2007). "Magnetic reconnection at the termination shock in a striped pulsar wind." In: *A&A* 473.3, pp. 683–700.

Philippov, A. and M. Kramer (2022). "Pulsar Magnetospheres and Their Radiation." In: *ARA&A* 60, pp. 495–558.

Popescu, C. C. et al. (2017). "A radiation transfer model for the Milky Way: I. Radiation fields and application to high-energy astrophysics." In: *MNRAS* 470.3, pp. 2539–2558.

Posselt, B. et al. (2017). "Geminga's Puzzling Pulsar Wind Nebula." In: *ApJ* 835.1, 66, p. 66.

Protheroe, R. J. and R. W. Clay (2004). "Ultra High Energy Cosmic Rays." In: *PASA* 21.1, pp. 1–22.

Ranasinghe, S. and D. A. Leahy (2018). "Revised Distances to 21 Supernova Remnants." In: *AJ* 155.5, 204, p. 204.

Rees, M. J. and J. E. Gunn (1974). "The origin of the magnetic field and relativistic particles in the Crab Nebula." In: *MNRAS* 167, pp. 1–12.

Reynolds, S. P. (2008). "Supernova remnants at high energy." In: *ARA&A* 46, pp. 89–126.

Reynolds, S. P. and R. A. Chevalier (1984). "Evolution of pulsar-driven supernova remnants." In: *ApJ* 278, pp. 630–648.

Rho, J. et al. (1994). "An X-Ray and Optical Study of the Supernova Remnant W44." In: *ApJ* 430, p. 757.

Riviere, C., H. Fleischhack, and A. Sandoval (2017). "HAWC detection of TeV emission near PSR B0540+23." In: *The Astronomer's Telegram* 10941, p. 1.

Ruderman, M. A. and P. G. Sutherland (1975). "Theory of pulsars: polar gaps, sparks, and coherent microwave radiation." In: *ApJ* 196, pp. 51–72.

Rybicki, G. B. and A. P. Lightman (1986). *Radiative Processes in Astrophysics*.

Sedov, L. I. (1959). *Similarity and Dimensional Methods in Mechanics*.

Seta, M. et al. (2004). "Detection of Shocked Molecular Gas by Full-Extent Mapping of the Supernova Remnant W44." In: *AJ* 127.2, pp. 1098–1116.

Shelton, R. L., K. D. Kuntz, and R. Petre (2004). "Chandra Observations and Models of the Mixed-Morphology Supernova Remnant W44: Global Trends." In: *ApJ* 611.2, pp. 906–918.

Sironi, L. and B. Cerutti (2017). "Particle Acceleration in Pulsar Wind Nebulae: PIC Modelling." In: *Modelling Pulsar Wind Nebulae*. Ed. by D. F. Torres. Vol. 446. Astrophysics and Space Science Library, p. 247.

Sironi, L. and A. Spitkovsky (2011). "Acceleration of Particles at the Termination Shock of a Relativistic Striped Wind." In: *ApJ* 741.1, 39, p. 39.

Sironi, L. and A. Spitkovsky (2014). "Relativistic Reconnection: An Efficient Source of Non-thermal Particles." In: *ApJ* 783.1, L21, p. L21.

Sironi, L., A. Spitkovsky, and J. Arons (2013). "The Maximum Energy of Accelerated Particles in Relativistic Collisionless Shocks." In: *ApJ* 771.1, 54, p. 54.

Smith, A. et al. (1985). "X-ray observations of the supernova remnant W 44." In: *MNRAS* 217, pp. 99–104.

Spitkovsky, A. (2008). "Particle Acceleration in Relativistic Collisionless Shocks: Fermi Process at Last?" In: *ApJ* 682.1, p. L5.

Strüder, L. et al. (2001). "The European Photon Imaging Camera on XMM-Newton: The pn-CCD camera." In: *A&A* 365, pp. L18–L26.

Sturrock, P. A. (1971). "A Model of Pulsars." In: *ApJ* 164, p. 529.

Sudoh, T., T. Linden, and J. F. Beacom (2019). "TeV halos are everywhere: Prospects for new discoveries." In: *Phys. Rev. D* 100.4, 043016, p. 043016.

Takahashi, T. et al. (2007). "Hard X-Ray Detector (HXD) on Board Suzaku." In: *PASJ* 59, pp. 35–51.

Temim, T. et al. (2009). "Chandra and XMM Observations of the Composite Supernova Remnant G327.1-1.1." In: *ApJ* 691.2, pp. 895–906.

Temim, T. et al. (2015). "Late-Time Evolution of Composite Supernova Remnants: Deep Chandra Observations and Hydrodynamical Modeling of a Crushed Pulsar Wind Nebula in SNR G327.1-1.1." In: *ApJ* 808.1, 100, p. 100.

Thompson, D. J. et al. (1996). "Supplement to the Second EGRET Catalog of High-Energy Gamma-Ray Sources." In: *ApJS* 107, p. 227.

Timokhin, A. N. and A. K. Harding (2019). "On the Maximum Pair Multiplicity of Pulsar Cascades." In: *ApJ* 871.1, 12, p. 12.

Torres, D. F. et al. (2014). "Time-dependent modeling of TeV-detected, young pulsar wind nebulae." In: *Journal of High Energy Astrophysics* 1, pp. 31–62.

Turner, M. J. L. et al. (2001). "The European Photon Imaging Camera on XMM-Newton: The MOS cameras." In: *A&A* 365, pp. L27–L35.

Uchida, H. et al. (2012). "Recombining Plasma and Hard X-Ray Filament in the Mixed-Morphology Supernova Remnant W 44." In: *PASJ* 64, 141, p. 141.

Uchiyama, Y. et al. (2012). "Fermi Large Area Telescope Discovery of GeV Gamma-Ray Emission from the Vicinity of SNR W44." In: *ApJ* 749.2, L35, p. L35.

Van Der Swaluw, E., A. Achterberg, and Y. A. Gallant (1998). "Hydrodynamical simulations of pulsar wind nebulae in supernova remnants." In: *Mem. Soc. Astron. Italiana* 69, p. 1017.

Venter, C. and O. C. de Jager (2007). "Constraints on the Parameters of the Unseen Pulsar in the PWN G0.9+0.1 from Radio, X-Ray, and VHE Gamma-Ray Observations." In: *WE-Heraeus Seminar on Neutron Stars and Pulsars 40 years after the Discovery*. Ed. by W. Becker and H. H. Huang, p. 40.

Vink, J. (2020). *Physics and Evolution of Supernova Remnants*.

Wang, Q. D. (2021). "X-Ray Jet, Counter-jet, and Trail of the Fast-moving Pulsar PSR B2224+65." In: *Research Notes of the American Astronomical Society* 5.1, 5, p. 5.

Wang, Q. D., F. Lu, and C. C. Lang (2002). "X-Ray Thread G0.13-0.11: A Pulsar Wind Nebula?" In: *ApJ* 581.2, pp. 1148–1153.

Watson, M. G. et al. (1983). "Einstein observations of the SNRs IC443, W44 and W49B." In: *Supernova Remnants and their X-ray Emission*. Ed. by J. Danziger and P. Gorenstein. Vol. 101, pp. 273–280.

Weibel, E. S. (1959). "Spontaneously Growing Transverse Waves in a Plasma Due to an Anisotropic Velocity Distribution." In: *Phys. Rev. Lett.* 2.3, pp. 83–84.

Weisskopf, M. C. et al. (2000). "Discovery of Spatial and Spectral Structure in the X-Ray Emission from the Crab Nebula." In: *ApJ* 536.2, pp. L81–L84.

Wilkin, F. P. (1996). "Exact Analytic Solutions for Stellar Wind Bow Shocks." In: *ApJ* 459, p. L31.

Wilms, J., A. Allen, and R. McCray (2000). "On the Absorption of X-Rays in the Interstellar Medium." In: *ApJ* 542.2, pp. 914–924.

Winkler, C. et al. (2003). "The INTEGRAL mission." In: *A&A* 411, pp. L1–L6.

Wolszczan, A., J. M. Cordes, and R. J. Dewey (1991). "Discovery of a Young, 267 Millisecond Pulsar in the Supernova Remnant W44." In: *ApJ* 372, p. L99.

Wolter, H. (1952). "Spiegelsysteme streifenden Einfalls als abbildende Optiken für Röntgenstrahlen." In: *Annalen der Physik* 445.1, pp. 94–114.

Wootten, H. A. (1977). "The molecular cloud associated with the supernova remnant W44." In: *ApJ* 216, pp. 440–445.

Yuan, W. et al. (2015). "Einstein Probe - a small mission to monitor and explore the dynamic X-ray Universe." In: *arXiv e-prints*, arXiv:1506.07735, arXiv:1506.07735.

de Jager, O. C. and A. Mastichiadis (1997). "A Relativistic Bremsstrahlung/Inverse Compton Origin for 2EG J1857+0118 Associated with Supernova Remnant W44." In: *ApJ* 482.2, pp. 874–880.

de Luca, A., M. Marelli, and P. A. Caraveo (2011). "X-Ray observations of "gamma-ray only" PSRs." In: *The 2011 Fermi Symposium*. The 2011 Fermi Symposium.

de Vries, M. and R. W. Romani (2022). "The Long Filament of PSR J2030+4415." In: *ApJ* 928.1, 39, p. 39.

di Tria, R. et al. (2022). "Analysis of the W 44 Supernova Remnant and its surroundings with Fermi-LAT and MAGIC." In: *37th International Cosmic Ray Conference*, 642, p. 642.

van der Swaluw, E. et al. (2003). "Interaction of high-velocity pulsars with supernova remnant shells." In: *A&A* 397, pp. 913–920.

COLOPHON

This document was typeset using the typographical look-and-feel `classicthesis` developed by André Miede and Ivo Pletikosić. The style was inspired by Robert Bringhurst's seminal book on typography *The Elements of Typographic Style*. The `classicthesis` template is available for both LaTeX and LyX at https://bitbucket.org/amiede/classicthesis/.

Final Version as of May 9, 2024 (classicthesis v4.6).

ACKNOWLEDGEMENT OF FUNDING

The author acknowledges funding by l'Agència de Gestió d'Ajuts Universitaris i de Recerca (AGAUR) official doctoral program for the development of a R+D+i project under the FI-SDUR grant (2021 FISDU 00369), and by Ministerio de Ciencia, Innovación y Universidades (MCIUN) through Proyectos I+D Generación de Conocimiento: FUENTES DE ALTA ENERGIA CON FLUJOS A DIFERENTES ESCALAS: TEORIA Y OBSERVACIONES (PID2019-105510GB-C31).